Motion Induced Noise in Marine Electromagnetic Data

Von der Fakultät für Elektrotechnik, Informationstechnik, Physik
der Technischen Universität Carolo-Wilhelmina
zu Braunschweig
zur Erlangung des Grades eines
Doktors der Naturwissenschaften
(Dr.rer.nat.)
genehmigte
Dissertation

von Kaushalendra Mangal Bhatt
aus Varanasi, India

Referentin oder Referent:

1. Prof. Dr. Andreas Hördt
2. Prof. Dr. Bülent Tezkan
3. Prof. Dr. Karl-Heinz Glaßmeier
4. Prof. Dr. Antje Schwalb

Dedicated to ...

Late Prof. Peter Weidelt
an unforgettable teacher

Contents

Summary

The marine **C**ontrolled **S**ource **E**lectromagnetic (mCSEM) method is an offshore geo-physical technique, employing a transmitter (dipole source) to transmit the electromagnetic field which couples with the sub-floor ground. The recorded signals are analyzed to reveal the geological information of interest (particularly hydrocarbon reservoirs). The mCSEM signals are often reported to be perturbed by electromagnetic noise in the ocean. The aim of the study was therefore to determine whether we can identify the noise sources which occur always and find possibilities to take measures against.

It is established that the motion of oceanic water in the Geomagnetic field creates electromagnetic signals. These motionally contributed signals at the sea-floor are generally considered small, but since the characteristic reservoir signal in mCSEM data is also small, the inclusion of the motional contribution in the modeling estimate will enhance the probability of reservoir detection. In this thesis, therefore we start with the theory of motional contribution of the electromagnetic field in the ocean. Commonly, the distortions in the mCSEM data set are reported to vary from one place and time of acquisition to the other. The oceanic background electromagnetic field is therefore studied by analyzing two data sets, which are described in chapters 3 and 5. Moreover, we have developed an approach to find the field line direction of frequencies in time to characterize the oceanic features, described in chapter 4.

The theory is developed with initial assumption that ocean consists of moving charge particles which experience a Lorentz force in the geomagnetic field. The action of Lorentz force generates a secondary electric field via galvanic and inductive processes. We used the Lorentz electric field as a source in the corresponding set of Maxwell's equations for the mathematical formulation. The equations are solved by disintegrating them into **T**angential **M**agnetic (TM) and **T**angential **E**lectric (TE) mode. The horizontal and vertical-horizontal component of the wave velocity excites the TM and TE mode, respectively. For the solution we first start with a simple two-halfspace model. Later, a layered model is considered by adding the transmissions and reflections by the interfaces. The solutions for these models are obtained by means of the Green's function. Further, we developed a theory for a special case which allows usage of a layered velocity model for the ocean. Provided the vertical velocity structure of the ocean is known, the development is significant as it could enable a realistic simulation.

The developed theory helps to demonstrate the physics of the motionally contributed signals and also informs the influence of the parameters in defining the field strength.

The theoretically gained knowledge helps in the analysis of measured mCSEM data. The mCSEM data sets are recored at the ocean floor. The time-segments of the data when the transmitter was inactive is equivalent to the data of a background field near the floor. Since the aim is to understand an ambient background electromagnetic noise therefore, we have chosen a time segment of the data where transmitter current is absent.

The power spectral density (PSD) is analyzed with respect to the prominent peaks. Four spectral peaks are evident corresponding to frequencies 0.4 Hz, 0.3 Hz, 0.2 Hz, and 1 Hz. The identification of the sources corresponding to these spectral peaks from the PSD plot alone is difficult and therefore spectrograms are analyzed. Unlike PSD, the time involvement in a spectrogram helps to evaluate the time related source characteristics of the significant peaks. The 0.3 Hz peak is a time ambient feature in the spectrogram, which suggests a time ambient source. The remaining peaks are observed momentarily and therefore are contributions by temporary sources. The spectrogram shows a broad spectral range of 0.1 to 1 Hz corresponding to the spectral peaks of 0.2 Hz and 0.4 Hz observed in the PSD. The likely candidates for 0.3 Hz, 1 Hz and a broad band 0.1 to 1 Hz could be respectively gravity waves, microseisms and mud-volcano. The detailed analysis suggests that the 0.3 Hz is most likely caused by the non-linear interaction of two wave trains. We reject 0.3 Hz as a contribution by the surface gravity waves since modeling study discards an arrival of a 3.3 seconds period wave at 500 m depth. For a profound understanding of the source contributions, the field line direction of each frequency is observed in time by plotting spectral-directionalograms. The result suggests that features at 1 Hz and 0.1 to 1 Hz might be a contribution by the transmitter.

The spectral-directionalogram is a new technique developed during this work. The technique provides the direction of the field lines for every registered frequency in varying time. Generally, a spectral peak in PSD corresponds to a source. The directional information corresponding to the spectral peak may help in identifying the source and eventually may lead to a robust interpretation. An application with the mCSEM data shows the essence of the methodology. As mentioned above, we observed that the source for the peaks at 1 Hz and 0.1 to 1 Hz is probably by the transmitter, which might be running in certain times when it should be absent.

A marine magnetotelluric (mMT) data set is analyzed to further aid the understanding. Two important factors motivate the study: First, the data set guarantees the absence of the transmitter current and second, the interesting topography in vicinity of the stations and thus suitable to observe the distortions by the topography. Six stations are studied, three from shallow depth and the remaining three from greater depth. Modeling of the electric and the magnetic spectra from different depth stations show a correspondence in the lower spectral range, which indicates an association with the natural field decay. The ionospheric and magnetospheric current system induces a natural fields in the earth. The change in the spectral pattern from one station to the other suggests a significant influence by the local topography. The observation shows that the topography distorts the magnetic field much more than the electric field. We present an explanation for the noted spectral pattern resemblance in the field components E_y, B_x and B_y. Like the observed 0.3 Hz in

the mCSEM data, we here too note a time ambient spectral feature at 0.25 Hz in deeper stations spectrograms. We have surmised similar source processes, as mentioned above, to explain the peak. Moreover, a correlation study is done between pressure, electric and magnetic fields to find the source resemblance. We have observed a correlation among the electric and the pressure field, which is of complicated nature, however.

The study concludes that there are oceanic sources which motionally contribute a significant field to distort the mCSEM signal. Inclusion of these fields in the modeling estimate is important for a proper detection of the reservoir. For example, we show powerful microseisms during the time of recording when transmitter was active. In this case, the modeling of the signal without accounting the microseisms may lead to a poor estimate. Particularly, the field generated by a non-linear interaction of the waves at the sea-surface (leading to a pressure gradient at the floor and generating a significant velocity field creating the electric field) is significant as it contributes a time-ambient field. We have observed these contributions in both the data sets (i.e. mCSEM and mMT). The strength of the feature suggests that it is insignificant in stations with smaller transmitter-receiver (T-R) separation but is significant in the stations with a large T-R separation.

1 Introduction

The marine magnetotelluric (mMT) (Constable *et al.* 1998) and the marine controlled source electromagnetic (mCSEM) (Chave *et al.* 1991) methods are geophysical techniques help to provide the lithospheric information. The horizontal components of the electric and the magnetic fields are measured (Constable *et al.* 1998) in both the methods. They use different energizing sources. The mMT method uses natural source field induced by the ionospheric and magnetospheric current systems (Chave & Filloux 1984). The method is sensitive to the conductive structures. On the other hand, the mCSEM method utilises an electrical transmitter for the source field. The mCSEM method is found sensitive to resistive structures (Weidelt 2007), which has turned it as a promising tool to detect and map the offshore hydrocarbon reservoirs (Constable & Srnka 2007). Moreover, the cost of drilling wells in the ocean are expensive and therefore, along with seismic data, mCSEM data set is useful as it further add the information to reduce the exploration risk (Ellingsrud *et al.* 2002) and helps to provide a better insight of the geology.

Electromagnetic fields are created in the ocean by the movement of oceanic water in the Geomagnetic field. These natural fields are signal for the oceanographic (Toh *et al.* 2011) and seismological applications (Manoj *et al.* 2010) but noise for mMT (Bahr 1988, Koefoed *et al.* 1980) and mCSEM (Hesthammer & Boulaenko 2005, Sinha *et al.* 1990) signals. Oceanographers use the fields to extract information on the detailed velocity structure and Seismologists use them to study the seismic background noise (Larsen 1997). The induced fields contaminate the mMT and mCSEM signals used for lithospheric and hydrocarbon exploration studies (MacGregor & Tompkins 2005, MacGregor & Sinha 2000). The signal of hydrocarbon reservoirs in mCSEM data is small and therefore small noise sources may be important. So far, the literature on the sources of noise is sparse. For example, some papers (Chave & Cox 1982, Chave 1983, Chave & Luther 1990) describe the mCSEM theory whereas studies reporting the background electromagnetic fields near the the ocean floor (Webb & Cox 1984) are rare. Our prime interest is therefore on an integrated motional contribution study for mCSEM problems. The results of the theory are also appropriate for other scientific applications.

The electromagnetic induction investigation has a long history. Faraday (1832) first reported deflection in the galvanometer by stream waves and concluded that a flow of water will induce electric currents, which were afterwards measured experimentally by Young *et al.* (1920). The motional induction study was almost neglected thereafter and got re-attention after World War II. Longuet-Higgins *et al.* (1954) carried out the study of

electric field induction by surface waves. The initial study of the magnetic filed creation by the oceanic movements was done by the authors Crews & Futterman (1962), Beal & Weaver (1970), and Fraser (1966). Considering the three-dimensional water flows, Sanford (1971) extended the theory of motional induction. A comprehensive study of the theory has been made by some authors like Larsen (1973), Podney (1975), Chave (1983). The motional induction problem was re-examined theoretically by Chave & Luther (1990). Despite of these existing formulations, we re-developed the theory due to the complexities involved even in the understanding of the source mechanisms, which governs the electromagnetic (EM) field creation in the ocean. Our aim is to provide a simple and illustrative physics of the source mechanism processes. Although we used a different approach to obtain the solutions, the results are consistent with the previously reported results. We adopted a much simpler methodology for the theoretical formulations, which gives an effective visualization of the associated physics. Unlike previous formulations (Podney 1975, Chave 1983), which use a source current decomposition into the two modal forms of the fields, we have utilized two different velocity structures to find the two modes of the EM fields i.e. TE (tangential electric) mode and TM (tangential magnetic) mode. The modal form is more illuminating as it links the physics of motional contribution with the oceanic velocity structure. Rather than using a vector potentials, which expresses the EM field in to two scalar potential where the choice of scalars is made to represent two uncoupled modes of toroidal and poloidal currents, the direct use of the modal form to obtain the field equations adds further simplicity to the theoretical formulations, which we describe in the chapter 2.

Chapter 2 starts with a simple case of a one dimensional model, where we assume one dimensional velocity and conductivity structure. The problem is mathematically formulated by assuming Lorentz electric field as a source in the corresponding set of Maxwell's equations. The equations are simplified and solved for different models by obtaining corresponding Green's functions. Later, we extended the model for two dimensional velocity structure. The toroidal velocity field is found to create the TM mode only while the TE mode is excited by a poloidal velocity field. We obtain a set of exact integral equations describing the induction process in an ocean as a function of vertically varying conductivity. We have solved the equations starting from simple geological models comprising of ocean and earth to more complicated suitable layered earth models. Moreover, we have also obtained the field expressions to incorporate the layered velocity structure of an ocean. The simple illuminative theoretical observations in this chapter will ably help in clarifying many complicated physical problems. For example, the role of electrical charges, implication of a particle trajectory path during surface wave movements in the creation of the electromagnetic fields, the role of the damping parameters in governing the field propagation etc.

As mentioned above, unfortunately there are only few practical studies (Webb & Cox 1986, Chave & Filloux 1984, Webb & Cox 1984, Peterson 1993) expressing the noise environment close to the sea-floor. There are some studies (Longuet-Higgins & Ursell 1948, Ponomaryov 1998, Longuet-Higgins 1950, Bromirski 2005, Tanimoto *et al.* 2006)

to characterize the source mechanism of a microseism (which is one of significant noise source for mCSEM data) but less (Chave & Filloux 1984) has been reported in context of the mCSEM interests. The reported studies commonly use only the power spectral density (PSD) plots and therefore provide poor characterization of the sources. For example, microseisms have been repeatedly studied but their characteristics are still poorly known, like their time related characterization, spectral content based on different governing parameters etc. The discussion in the Chapter 3 is limited in the context to mCSEM interests to recognize and characterize the possible oceanic features contributing a significant electric field at the ocean floor. We have utilised a mCSEM electric field time-series data set for the purpose, provided by KMS Technologies-KJT Enterprises Inc. We studied only those time-segments, where the transmitter was inactive as the aim was the study of the background EM field. First, we hypothesize the different sources for the observed spectral peaks of the PSD. Further, to recognize and characterize the sources, spectrograms are plotted, which are helpful in providing the time based characteristics of the peaks. The consideration of the directionality of features, together with spectrograms makes this study different from the previous studies. We have used various discussions to describe the suitability of the sources corresponding to a spectral peak. The theory developed in chapter 2 is used to model a spectral peak and to understand the field characteristics. This chapter serves to exemplify the possible oceanic sources significant for the mCSEM data. From my knowledge, this study is the first to show the various oceanic features capable of producing significant distortions in the mCSEM data.

The natural electric field creation in the ocean is a function of a velocity (vector field). Various oceanic features (Sundermann 1994, Pinet 2006) create different velocity fields. The directional knowledge of these features (sources) could prove therefore a useful asset to characterize them. Mostly, oceanic features are time-dependent and therefore they demand a technique which can bring directional information of the sources together with the changing time. Using Windowed Fourier Transform (Griffin 1984) as an integral part of the technique, we developed a new approach 'Spectral-Directionalograms', which is described in Chapter 4. This technique measures the field lines directions of every registered frequencies of a vector field in time. As discussed above, the purpose of technique is the profound understanding of the sources for their distinct characterization.

There are studies to characterize a relationship between the microseism (Longuet-Higgins 1950, Kedar *et al.* 2008) and the swell (Haubrich *et al.* 1963). The pressure and electric field near the deep sea floor are studied by Webb & Cox (1986) to examine the relationship between two fields. In our final chapter, we have analyzed a mMT data set, which contains magnetic and pressure data together with the electric field data. The creation of the electric and magnetic field is a function of the velocity in the ocean. The Bernoulli's law indicates that the pressure is as well a function of the velocity and therefore a correlation between the electric and pressure fields are expected. Might be due to the same reasons, Webb & Cox (1984) searched for coherency, but were unsuccessful to report any. Despite of the suggested relationships, the absence of correlation is surprising and therefore motivated the study discussed in this chapter. Particularly, the data set is

interesting because of the undulating topography near the acquisition area. An attempt to outline a role of topography together with the various observed spectral features are an interesting aspect in the chapter.

We will show that a microseism can significantly distort mCSEM data. Prior to modeling or inversion, it is therefore essential to analyze and compensate the data set against such powerful features. The oceanic features like the wave-wave interaction and tidally induced motions are among sources which can distort mCSEM recording at larger transmitter-receiver separations. The influence of topography is found significant in the data.

2 Theory

2.1 The Motional Contribution

In presence of both the electric $\vec{E_0}$ and the magnetic $\vec{B_0}$ fields, an electric charge q moving with a velocity $\vec{V}$ experiences a Lorentz force $\vec{F_L}$ (Jackson 1975) given by

$$\vec{F_L} = q(\vec{E_0} + \vec{V} \times \vec{B_0}) \tag{2.1}$$

In presence of only the magnetic field $\vec{B_0}$, the expression (Eq. 2.1) becomes

$$\vec{F_L} = q(\vec{V} \times \vec{B_0}) \tag{2.2}$$

This implies

$$\vec{E_L} = \vec{V} \times \vec{B_0} \tag{2.3}$$

An ocean consisting of the charged particles is our assumption. This suggests that a dynamic ocean in the geomagnetic field will generate a Lorentz electric field $\vec{E_L}$ (Eq. 2.3), which in turn will create a secondary electric field $\vec{E}$ by the two ways: a) Galvanic way and b) Inductive way.

2.1.1 Galvanic Way

The oceanic regions where $\vec{E_L}$ has a component parallel to the conductivity gradient ($\nabla\sigma$), space or surface charges are accumulated. These accumulated electric charges galvanically create a secondary electric field $\vec{E}$ (Weidelt (2009, pers.comm)), even if the velocity does not change with time.

In the case of DC field, $\vec{E}$ can be related with a scalar potential function U, which is continuous across the boundary such that

$$\vec{E} = -\nabla U \tag{2.4}$$

Ohm's law (with $\vec{J}$ as current density) for the case is

$$\vec{J} = \sigma(\vec{E} + \vec{V} \times \vec{B_0}) \tag{2.5}$$

17

According to Gauss theorem,

$$\nabla \cdot \vec{J} = 0 \tag{2.6}$$

It follows from Eq. 2.5 using Eq. 2.4

$$\nabla \cdot (\sigma \nabla U) = \nabla \cdot [\sigma(\vec{V} \times \vec{B_0})] \tag{2.7}$$

Further detail on accumulation of charges will be discussed in the Section 2.5.

2.1.2   Inductive Way

A current density is created i.e.

$$\vec{J} = \sigma(\vec{V} \times \vec{B_0}) \tag{2.8}$$

This creates a magnetic field $\vec{H}$ if $\vec{V}$ changes with time (from Ampere's Law) i.e.

$$\nabla \times \vec{H} = \vec{J} \tag{2.9}$$

In turn, the field $\vec{H}$ induces a secondary electric field $\vec{E}$ via the law of induction (Faraday's Law) i.e.

$$\nabla \times \vec{E} = -\mu_0 \partial_t \vec{H} \tag{2.10}$$

2.2   Governing Equations

The electromagnetic field creation in the ocean using the quasi-static approximation formulates the set of Maxwell's equation to be solved for the motional induction problem. The useful frequencies for oceanic induction problems are less than one cycles per minute (Larsen 1973) and therefore the quasi-static approximation is appropriate (Sanford 1971). Thus, the governing equations are

$$\nabla \times \vec{H} = \sigma(\vec{E} + \vec{V} \times \vec{B_0}) \tag{2.11}$$

$$\nabla \times \vec{E} = -\mu_0 \partial_t \vec{H} \tag{2.12}$$

In an exact formulation, the ambient magnetic field is the sum of the earth's magnetic field $\vec{B_0}$, the ionospheric current system generated external magnetic field $\vec{B_{ext}}$, the field generated by local anomalies $\vec{B_{ano}}$ and the motionally contributed field $\vec{B_{mi}}$ i.e.

$$\vec{B} = \vec{B_0} + \vec{B_{ext}} + \vec{B_{ano}} + \vec{B_{mi}} \tag{2.13}$$

In general, the time varying induced magnetic fields (last three terms) are order of magnitude smaller than the steady geomagnetic field $\vec{B_0}$. Therefore, the local value of the earth's magnetic field is a good choice and we will use throughout the manuscript. In the

geo-electromagnetism, motional contribution is known as motional induction. But this is an incomplete name as Eq. 2.11 asserts that an electric field can be produced not only by the induction process ($\vec{V} \times \vec{B_0}$) but also by the galvanic ways $\vec{E}$. Therefore, rather than 'motional induction' we will stick to the name 'motional contribution'.

2.3   One Dimensional Case

To gain the basic insight into the problems of the motional contribution, we here begin with a simple one dimensional (1D) case in which the electromagnetic field is assumed to depend only on the z coordinate of the rectangular coordinate system (x,y,z). Throughout the manuscript we have retained vertical axis z positive in the downward direction.
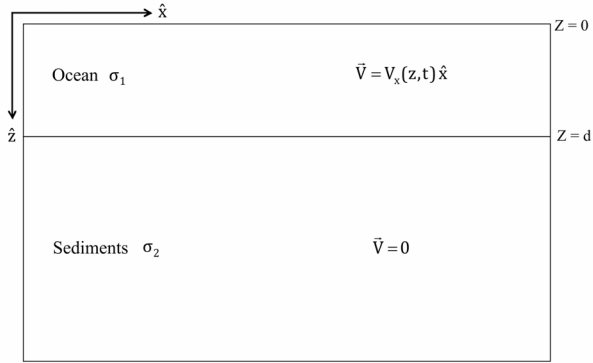
Figure 2.1: Schematic representation of a 1D model used for the problem formulation.

2.3.1   The 1D Model

For the formulation of the problem, let us imagine an ocean moving in a geomagnetic field (Fig. 2.1). Let $\vec{V}$ be the velocity of the oceanic movement in the x-direction. For simplicity, assume velocity as a function of depth (z) and time (t) (i.e $\vec{V} = V_x(z,t)\hat{x}$). Let the ocean-bottom be flat with $z = 0$ and $z = d$ as its surface and floor, respectively. Below the ocean, a static sedimentary layers is assumed. Let the vertical geomagnetic field be $\vec{B_0} = B_0\hat{z}$. As the wave movement direction is x and magnetic field direction is z, it will create an electric and a magnetic field in y and x direction, respectively. Therefore,

$$\vec{E} = E_y(z,t)\hat{y} \tag{2.14}$$

$$\vec{H} = H_x(z,t)\hat{x} \tag{2.15}$$

19

The above considerations simplify the Eq. 2.11 and Eq. 2.12 as

$$H_x^{'} = \sigma(E_y - V_x B_0) \tag{2.16}$$

$$E_y^{'} = \mu_0 \dot{H}_x \tag{2.17}$$

Here, prime and dot respectively represent the partial differentiation w.r.t. z and t. Differentiating partially Eq. 2.16 and Eq. 2.17 with respect to t and z, respectively and substitution gives,

$$E_y^{''} = \mu_0 \sigma(\dot{E}_y - \dot{V}_x B_0) \tag{2.18}$$

Let us assume harmonic time dependence $V_x(z,t) = \tilde{V}_x(z)e^{i\omega t}$. This implies that the same behavior like the velocity will be followed by both the fields (electric and magnetic)

$$E_y(z,t) = \tilde{E}_y(z)e^{i\omega t} \tag{2.19}$$

$$H_x(z,t) = \tilde{H}_x(z)e^{i\omega t} \tag{2.20}$$

Use of Eq. 2.19 and Eq. 2.20 simplifies Eq. 2.18 and we obtain

$$\tilde{E}_y^{''}(z) = i\omega\mu_0\sigma(z)[\tilde{E}_y(z) - \tilde{V}_x(z)B_0] \tag{2.21}$$

$$= k^2(z)[\tilde{E}_y(z) - \tilde{V}_x(z)B_0] \tag{2.22}$$

$$\text{with,} \quad k^2 = i\omega\mu_0\sigma(z) \tag{2.23}$$

The term k^2 in Eq. 2.23 is the vertical wavenumber and represents the electromagnetic damping. It is complex such that amplitude decay is associated with a phase shift with respect to the field at the surface. The Eq. 2.22 describes the electric field signal generated by moving water in the geomagnetic field. The equation involves $k^2\tilde{V}_x(z)B_0$, which is the source term for the motional contribution problem. Now our problem is formulated and solution for the Eq. 2.22 is our aim. Rearrangement gives

$$\tilde{E}_y^{''}(z) - k^2(z)\tilde{E}_y(z) = -k^2(z)\tilde{V}_x(z)B_0 \tag{2.24}$$

The right-hand side of Eq. 2.24 contains the source term, which is known. Therefore, the equation can be solved using the Green's function, which is the response of a unit point source at the origin (Nabighian 1987). The Green's function corresponding to Eq. 2.24 is defined by

$$G^{''}(z/z_0) - k^2(z)G(z/z_0) = -\delta(z - z_0) \tag{2.25}$$

The solution for $\tilde{E}_y$ is obtained by the condition's that both $\tilde{E}_y^{'}$ and $G^{'}$ will vanish at limits $-\infty$ and $+\infty$,

$$\tilde{E}_y(z_0) = \int_{-\infty}^{+\infty} k^2(z)\tilde{V}_x(z)B_0G(z/z_0)\,dz \tag{2.26}$$

The integration range reduces to 0 to d because that is the range where source is nonzero.

$$\tilde{E}_y(z_0) = \int_0^d k^2(z)\tilde{V}_x(z)B_0 G(z/z_0)\,dz, \qquad -\infty < z_0 < +\infty \qquad (2.27)$$

$$= B_0 \int_0^d k^2(z)\tilde{V}_x(z)G(z/z_0)\,dz \qquad (2.28)$$

The Eq. 2.28 is a general expression for the electric field signal. The equation demands the knowledge of the Green's function.

2.3.2   Green's function

The Green's function is commonly used to solve inhomogeneous boundary value problems. The solution by means of the Green's function gives a special advantage because of its reciprocity property, which means relationship between a source and the resulting field at some point of observation is unchanged even if the observation and source points are interchanged. Calculation of the Green's function demands boundary conditions. From Eq. 2.25 follows

$$G'(z_0 + \epsilon/z_0) - G'(z_0 - \epsilon/z_0) = -1 \qquad (2.29)$$

and

$$G(z_0 + \epsilon/z_0) - G(z_0 - \epsilon/z_0) = 0 \qquad (2.30)$$

i.e. $G(z/z_0)$ is continuous at $z = z_0$. Here, ϵ is a small positive number. With the known boundary conditions, let us first solve the Green's function for a simplest case.

2.3.2.1   Uniform Full-space Model

A uniform full-space is defined as $\sigma(z) = \sigma$ and therefore $k(z) = k$. We consider

$$G(z/z_0) = \begin{cases} Ae^{+kz} & \text{for } z < z_0 \\ Be^{-kz} & \text{for } z > z_0 \end{cases} \qquad (2.31)$$

Putting Eq. 2.31 in Eq. 2.29 and Eq. 2.30 gives

$$-Bke^{-kz_0} - Ake^{-kz_0} = -1 \qquad (2.32)$$

$$Be^{-kz_0} - Ae^{-kz_0} = 0 \qquad (2.33)$$

Solving above equation gives the value of A and B as

$$A = \frac{1}{2k}e^{-kz_0} \qquad (2.34)$$

$$B = \frac{1}{2k}e^{+kz_0} \qquad (2.35)$$

Inserting the value of *A* and *B* in Eq. 2.31 yields,

$$G(z/z_0) = \frac{1}{2k}e^{-k|z-z_0|} \tag{2.36}$$

The Eq. 2.36 is a expression for the Green's function corresponding to a full-space.

2.3.2.2   Two Uniform Half-spaces Model

The absence of the conductivity contrast in the full-space model makes it a very crude and an ideal model. Let us consider a two uniform half-space model with $k(z) = k_0$ in the air (i.e. $z < 0$) and $k(z) = k$ in the earth (i.e. $z > 0$)(Fig. 2.2). Although this model is still very simple but it accounts for the electromagnetic effects at a major conductivity discontinuity of earth-air boundary. In the earth half-space $z \geq 0$, together with the downward progressing motionally contributed signal, there also exists a signal reflected from the air-earth interface. The transmitted part of the signal will contribute to the air half-space. Therefore, for $z_0 > 0$ let us assume
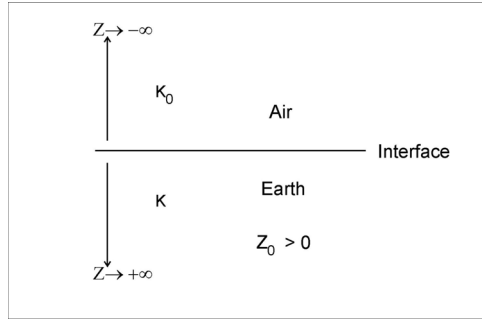
Figure 2.2: Idealistic diagram of a two half-spaces model. The parameter k_0 and k represents the electromagnetic damping in the air half-space ($z < 0$) and the earth half-space ($z < 0$), respectively.

$$G(z/z_0) = \begin{cases} \frac{1}{2k}e^{-k|z-z_0|} + Re^{-kz} & \text{for } z \geq 0 \\ \\ Te^{k_0 z} & \text{for } z \leq 0 \end{cases} \tag{2.37}$$

where T and R are respectively transmission and reflection coefficients. The continuity of $G(z/z_0)$ and $G'(z/z_0)$ at $z = 0$ yields

$$R = \frac{1}{2k}\left(\frac{k-k_0}{k+k_0}\right)e^{-kz_0} \tag{2.38}$$

$$T = \left(\frac{1}{k+k_0}\right)e^{-kz_0} \tag{2.39}$$

Substituting Eq. 2.38 and Eq. 2.39 in Eq. 2.37 yields

$$G(z/z_0) = \begin{cases} \frac{1}{2k} \left[e^{-k|z-z_0|} + \left(\frac{k-k_0}{k+k_0} \right) e^{-k(z+z_0)} \right] & \text{for } z \geq 0, z_0 \geq 0 \\ \frac{1}{k+k_0} e^{k_0 z - k z_0} & \text{for } z \leq 0, z_0 \geq 0 \end{cases} \tag{2.40}$$

In particular, for a insulating air half-space $k_0 = 0$, as $\sigma = 0$, the two half-space Green's function takes the form

$$G(z/z_0) = \begin{cases} \frac{1}{2k} \left[e^{-k|z-z_0|} + e^{-k(z+z_0)} \right] & \text{for } z \geq 0, z_0 \geq 0 \\ \frac{1}{k} e^{-k z_0} & \text{for } z \leq 0, z_0 \geq 0 \end{cases} \tag{2.41}$$

2.3.2.3 Layered Model

Actual earth is neither half-space nor two half-space. It is much more complicated than any mathematical model. Despite the fact, a layered model is good mathematical approximation as it replicates much close real situation than used previous two models (i.e. half-space and two half-space). The possibility to allocate multi-layers of a desired conductivity and thickness provides flexibility to the model to make it practically reasonable.
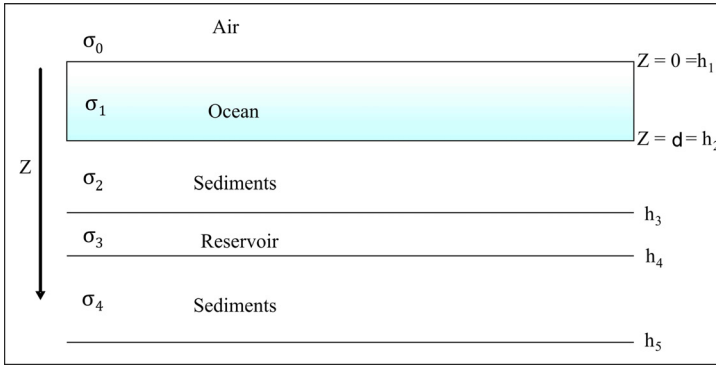
Figure 2.3: Idealistic diagram of a layered model used for the calculation of a layered Green's function. Here, σ_n and h_n respectively represent the conductivity and the thickness of the different layers.

Let us consider a canonical model (Constable & Key 2006), which is a layered model and is commonly used for the studies in marine controlled source electromagnetic (mC-SEM) methods. The model is shown in Fig. 2.3 which includes an ocean, two sedimentary layers and a reservoir. Reservoirs are also a sedimentary rock formation but they are much resistive than the normal sedimentary formations because of the hydrocarbon saturation.

The differences in conductivity are therefore an obvious cause for various interfaces in the model, which will create reflection and transmission of the signals. The Green's function for such a layered model will therefore contain a reflection and transmission term. Consequently, let us assume

$$G(z/z_0) = \frac{1}{2k_1} \left[e^{-k_1|z-z_0|} + R_d e^{-k_1 z} + R_u e^{+k_1 z} \right] \quad 0 \le z \le d, \quad 0 \le z_0 \le d \qquad (2.42)$$

where $k_1 = \sqrt{i\omega\mu_0\sigma_1}$ is the propagation constant and it represents the electromagnetic damping in the ocean. The constant R_d describes the field propagating downward due to the reflection from the air-earth interface (i.e. $z = 0$) and R_u describes the field propagating upward by the reflection from the ocean floor (i.e. $z = d$). Since $G(z/z_0)$ is constant in the air half-space suggesting

$$G'(z/z_0) = 0 \qquad (2.43)$$

at the surface. A continuous transfer function (Weidelt 2007) derived from $G(z/z_0)$ is given by

$$G'(d/z_0) = -\mu_0 b_e(d) G(d/z_0) \qquad (2.44)$$

where $b_e(d)$ is determined using Appendix A. These two boundary (Eq. 2.43 and Eq. 2.44) conditions are significant for the determination of the constants R_d and R_u. They yield,

$$R_d = \frac{1 - R_c e^{-2k_1(d_1-z_0)}}{1 + R_c e^{-2k_1 d_1}} \; e^{-k_1 z_0} \qquad (2.45)$$

$$R_u = -\frac{R_c(1 + e^{-2k_1 z_0})}{1 + R_c e^{-2k_1 d_1}} \; e^{-k_1(2d_1-z_0)} \qquad (2.46)$$

with

$$R_c = \frac{\mu_0 b_2 - k_1}{\mu_0 b_2 + k_1} \qquad (2.47)$$

2.3.3   Solution For Two Half-spaces Model

In Section 2.3.1, we derived an expression for the electric field (Eq. 2.28) in term of the Green's function. We have now the expressions for the Greens's function, which we can use to calculate the field for a two half-space model. In the air halfspace i.e. $z < 0$ we assume $\sigma(z) = 0$. The space $z > 0$ is the earth halfspace, which contains a dynamic ocean and static sediments. For the simplicity, we assume that the conductivity of both the formations (i.e. ocean and the sediments) are constant and is $\sigma(z) = \sigma$. We can further simplify the expression by assuming a constant velocity $V(z) = V$ in the ocean. Finally, we obtain,

$$\tilde{E}_y(z_0) = k^2 V B_0 \int_0^d G(z/z_0) \, dz, \quad -\infty < z_0 < +\infty \qquad (2.48)$$

The Green's function in the air half-space is $G(z/z_0) = \frac{1}{k} e^{-kz_0}$ (Eq. 2.41). The inclusion in the expression gives

$$
\begin{aligned}
\tilde{E}_y(z_0) &= k^2 V B_0 \int_0^d (\frac{1}{k} e^{-kz}) \, dz, \\
&= V B_0 \, (1 - e^{-kd}), \quad z_0 \leq 0
\end{aligned}
\tag{2.49}
$$

This is an expression for the horizontal electric field $\tilde{E}_y(z_0)$ in the air half-space. It is evident that the field is constant in the air.

The Green's function in the earth half-space is $G(z/z_0) = \frac{1}{2k} \left[e^{-k|z-z_0|} + e^{-k(z+z_0)} \right]$. The inclusion in Eq. 2.48 yields

$$
\begin{aligned}
\tilde{E}_y(z_0) &= \frac{kVB_0}{2} \left[\int_0^d e^{-k|z-z_0|} \, dz + \int_0^d e^{-k(z+z_0)} \right] dz, \\
&= \frac{VB_0}{2} \left[e^{+kz_0} \, (1 - e^{-kd}) \, + \, e^{-kz_0} \, (1 - e^{-kd}) \right], \\
&= V B_0 \, (1 - e^{-kd} \, \cosh kz_0), \quad 0 \leq z_0 \leq d
\end{aligned}
\tag{2.50}
$$

$$
\begin{aligned}
\tilde{E}_y(z_0) &= \frac{kVB_0}{2} e^{-kz_0} \int_0^d (e^{kz} + e^{-kz}) \, dz, \\
&= V B_0 \, e^{-kz_0} \, \sinh kd, \quad z_0 \geq d
\end{aligned}
\tag{2.51}
$$

For $z_0 = 0$, it is evident from the Eq. 2.50 that the strength of the horizontal electric field of a homogeneous ocean depends chiefly on the four factors (oceanic conductivity is assumed constant):

1. Wave velocity
2. Strength of the geomagnetic field
3. Thickness of the ocean
4. Frequency

The field strength would be strong for a thick ocean if other three factors are assumed constant. This suggests that a shallow ocean contributes a weak electric field at the surface.

We have now the expression for the electric field, which we can use to find the expression for the magnetic field using the Eq. 2.17

$$
\tilde{B}_x(z_0) = \frac{1}{i\omega} \tilde{E}_y{}'(z_0)
\tag{2.52}
$$

In the air half-space, the horizontal magnetic field will be zero i.e.

$$
\tilde{B}_x(z_0) = 0 \quad \text{for } z_0 \leq 0
\tag{2.53}
$$

25

while in the earth half-space, the expression is

$$\tilde{B}_x(z_0) = \frac{-kVB_0}{i\omega}e^{-kd}\sinh(kz_0) \qquad \text{for } 0 \leq z_0 \leq d \qquad (2.54)$$

$$\tilde{B}_x(z_0) = \frac{-kVB_0}{i\omega}e^{-kz_0}\sinh(kd) \qquad \text{for } z_0 \geq d \qquad (2.55)$$

2.3.4 Results

We have assumed a halfspace of conductivity 3.33 S/m as the standard conductivity for the ocean is 3.33 S/m (Cox 1981). The oceans and the sedimentary formation are assumed respectively in dynamic and static state. A homogeneous velocity of 0.1 m/s is assumed in the ocean. The difference in the velocity state marks the interface of the formations. The strength of the vertical geomagnetic field is assumed 5×10^{-5} T. The magnetic permeability is assumed constant and is equal to the free space permeability value i.e. $\mu_0 = 4\pi \times 10^{-7}$ Vs/Am. The depth wise variation of the horizontal electric and magnetic field for three frequencies 0.01, 0.1 and 1 Hz are shown in Fig. 2.4. Evidently, in general, the strength of the field E_y is finite at the surface and it gradually reduces with the depth. On the other hand, the field B_x is zero at the surface and it progressively gets stronger within the ocean. Strongest strength is recorded at the ocean floor. The zero amplitude of the B_x field is surprising but can be understood from the Eq. 2.49. Here, the E_y field is constant in the air and surface. The B_x field is as a vertical derivative (Eq. 2.52) of E_y and therefore this will be zero in the air and surface too.

The Eq. (2.50, Eq. 2.51, Eq. 2.54 and Eq. 2.55) imply that the increase/decrease in V and B_0 will cause a increase/decrease in the E_y and B_x field. Thus, both the fields are sensitive to the velocity and geomagnetic field. In this respect, we observe a significant observation at the ocean floor, which is a velocity interface. The response pattern of the E_y field shows a smooth transition here while the B_x field indicates a sharp change. The conductivity of both the formations are same. They only differ in their velocity state. The observation therefore suggests that the field B_x effectively reads the velocity changes of the formations. For the practical considerations, therefore, the B_x field will be more informative and effective in providing the velocity changes than the E_y field.

2.3.5 Layered Model Expressions

The impedance contrast present at the layered boundaries of a layered model offer reflections and therefore, unlike uniform half-space model which includes only downward propagating waves, a layered model includes both downward and upward propagating waves. This advantage together with the flexibility to choose thickness and conductivity of layers makes a layered model much superior than the uniform half-space model. We have already derived an expression for the layered Green's function (Eq. 2.42 - 2.47) and we can therefore easily calculate the field expressions for a layered model. The expression
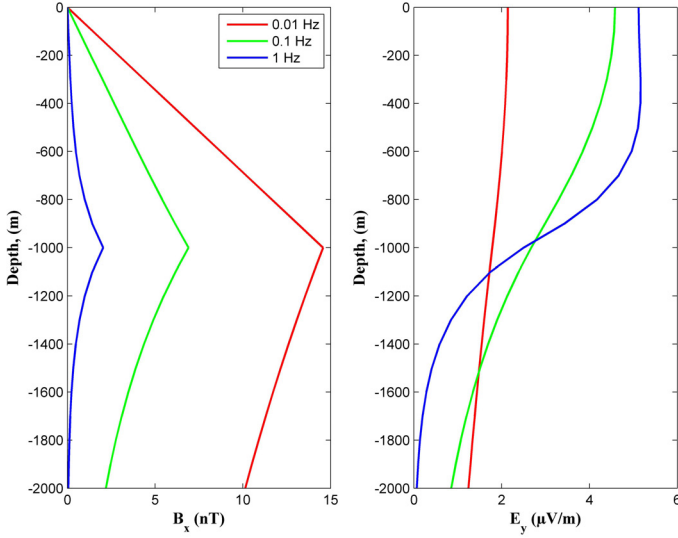
Figure 2.4: For a half-space model, the graph shows the variation of the fields E_y and B_x with respect to the depth. The response is computed for a model consisting of a dynamic ocean and a static sedimentary layer, placed below the ocean. Identical conductivity ($\sigma = 3.33$ S/m) is assumed for both the formations. The thickness of each formations are assumed 1000 m. The response is generated for three frequencies viz. 0.01, 0.1 and 1 Hz, shown in red, green and blue colors, respectively.

for the electric field, from (Eq. 2.28), is

$$\tilde{E}_y(z_0) = \int_0^d k^2(z)\tilde{V}_x(z)B_0 G(z/z_0) \, dz, \qquad -\infty < z_0 < +\infty$$

Within the ocean (i.e. $0 < z_0 < d_1$), for a conductivity of σ_1 and homogeneous velocity V (Fig. 2.3), the expression becomes

$$
\begin{aligned}
\tilde{E}_y(z_0) &= k^2 V B_0 \int_0^{d_1} G(z/z_0) \, dz \\
&= \frac{k V B_0}{2} \int_0^{d_1} [e^{-k|z-z_0|} + R_d e^{-kz} + R_u e^{+kz}] \, dz \\
&= \frac{V B_0}{2} [2 - e^{-kz_0} - e^{k(z_0-d_1)} - R_d \, (e^{-kd_1} - 1) + R_u \, (e^{+kd_1} - 1)] \, dz \quad (2.56)
\end{aligned}
$$

with $k^2 = i\omega\mu_0\sigma_1$. The expression for the magnetic field with in the ocean can be obtained from the electric field, as

$$
\begin{aligned}
\tilde{B}_x(z_0) &= \frac{1}{i\omega}\tilde{E}_y(z_0) \\
&= \frac{VB_0}{2i\omega}[k(e^{-kz_0} - e^{k(z_0-d_1)}) - R'_d(e^{-kd_1} - 1) + R'_u(e^{kd_1} - 1)]
\end{aligned}
\tag{2.57}
$$

where, R'_d and R'_u represent the vertical partial derivative of R_d and R_u, respectively.

2.3.6   Results

The field responses corresponding to the E_y and B_x fields at frequencies 0.01, 0.1 and 1 Hz for a layered model are shown in Fig. 2.5. The overlyed dotted lines represent a layered segmentation of different formations. The conductivity of the ocean, sediments and the reservoir is assumed 3.33 S/m, 1 S/m and 0.01 S/m, respectively. The assumed thickness of the ocean and the reservoir is 1000 m and 100 m. Above and below the reservoir, there exists a 1000 m thick layer of static sediments. We assume homogeneous velocity of 0.1 m/s in the ocean. The magnetic permeability is assumed constant and is equal to the free space permeability i.e. $\mu_0 = 4\pi \times 10^{-7}$ Vs/Am. The strength of the vertical geomagnetic field is assumed 5×10^{-5} T.

The primary purpose of a layered model is to study the change in response due to various formations. Evidently, the response pattern and their characteristics (like maximum and minimum strength at different depth) are same as we have observed in the previous case of half-space model. The response pattern shows two significant observations of particular interest. The first observation is that the B_x field detects the vertical conductivity variations while E_y does not see it. The second observation is that the B_x field is weaker compared to the half-space response. These two observations suggest that the B_x field notices the conductivity of the formations. Moreover, we know from the study of the halfspace response that the B_x field effectively detects the velocity variations. The combined results of the halfspace model and the layered model, therefore suggests that the B_x field is effective in detecting the velocity changes and vertical conductivity changes of the formations.

2.4   Two Dimensional Case

In the previous section, we have discussed a simple one dimensional motional induction problem. We formulated the problem with the one dimensional velocity structure $V = V(z)$. Thereafter, we solved it for two different models: the two half-space model and the layered model. The responses are studied to understand the field characteristics. In the current section, we will extend the previous formulation by assuming a 2D velocity structure i.e. $V = V(y, z)$.
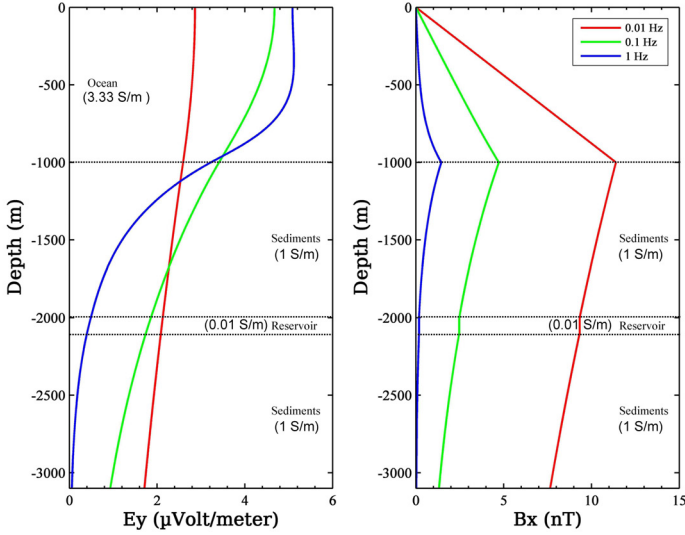
Figure 2.5: The strength of horizontal electric E_y and magnetic B_x field Vs. depth for a layered earth model. Computations are made for the three frequencies 0.01, 0.1 and 1 Hz. The model includes an ocean of conductivity 3.33 S/m and thickness 1000 m (i.e. $0 \geq z \geq 1000$ m). Below the ocean, there exists a sedimentary layer of thickness 1000 m and conductivity 1 S/m. A reservoir of thickness 100 m and conductivity 0.01 S/m is embedded in the sedimentary layer (below 2000 m depth). The same formation of the sedimentary layer is assumed to extend below the reservoir. The horizontal dotted lines mark the boundary of the different formations.

The problem of the electromagnetic field creation can be simplified by representing the field as a superposition of two distinct modes, namely, **T**angential **E**lectric mode (TE mode), in which the electric field $\vec{E}$ is tangential to the surfaces z = constant and **T**angential **M**agnetic mode (TM mode), in which the magnetic field $\vec{B}$ is tangential to the surfaces z = constant. The x-axis is the strike direction. Let us consider waves, with a wavelength λ_y in the y-direction and velocity parallel to strike direction, such that the flow is periodic and non-divergent i.e. $\nabla \cdot \vec{V} = 0$

$$V_x(y, z) = \bar{V}_x(z) \cos(Sy), \quad \text{for } -\infty < y < +\infty \tag{2.58}$$

Where, S is horizontal wave number in the direction of wavelength and is equal to $2\pi/\lambda_y$.

As velocity is function of y and z and therefore the field will not change in the x direction i.e. $\partial_x \equiv 0$. The disintegration of Eq. 2.11 and Eq. 2.12 in two systems using

Eq. 2.58 generates

<div align="center">FIRST SYSTEM</div>

$$\partial_z H_x \;=\; \sigma(E_y - V_x B_0) \tag{2.59}$$

$$-\partial_y H_x \;=\; \sigma E_z \tag{2.60}$$

$$\partial_y E_z - \partial_z E_y \;=\; -i\omega\mu_0 H_x \tag{2.61}$$

<div align="center">SECOND SYSTEM</div>

$$\partial_y H_z - \partial_z H_y \;=\; \sigma E_x \tag{2.62}$$

$$\partial_z E_x \;=\; -i\omega\mu_0 H_y \tag{2.63}$$

$$-\partial_y E_x \;=\; -i\omega\mu_0 H_z \tag{2.64}$$

It can be observed that in the first system (Eq. 2.59 to 2.61), the field $\bar{H}$ has only a component H_x which is parallel to the strike direction (i.e. x-direction) and the field $\bar{E}$ has two components (i.e E_y and E_z) which lies in the plane perpendicular to the strike direction. On the other hand in the second system (Eq. 2.62 to Eq. 2.64), the field $\bar{E}$ has a component E_x parallel to the strike direction and in the plane perpendicular to the strike direction there exist two components H_y and H_z of the field $\bar{H}$. This indicates that the first and the second system respectively represent the TM mode and the TE mode. Modal equations can be re-written as

<div align="center">THE TM MODE</div>

$$E_y \;=\; +\frac{1}{\sigma}\,\partial_z H_x + V_x B_0 \tag{2.65}$$

$$E_z \;=\; -\frac{1}{\sigma}\,\partial_y H_x \tag{2.66}$$

$$H_x \;=\; -\frac{1}{i\omega\mu_0}\left[\partial_y E_z - \partial_z E_y\right] \tag{2.67}$$

<div align="center">THE TE MODE</div>

$$H_y \;=\; -\frac{1}{i\omega\mu_0}\,\partial_z E_x \tag{2.68}$$

$$H_z \;=\; +\frac{1}{i\omega\mu_0}\,\partial_y E_x \tag{2.69}$$

$$E_x \;=\; +\frac{1}{\sigma}\left[\partial_y H_z - \partial_z H_y\right] \tag{2.70}$$

After substituting the value of E_y, E_z in Eq. 2.67, we obtain the TM mode expressions as

$$\frac{1}{\sigma}\partial_{yy}^2 H_x + \partial_z(\frac{1}{\sigma}\partial_z H_x) = i\omega\mu_0 H_x - B_0\partial_z V_x \tag{2.71}$$

with

$$E_y = +\frac{1}{\sigma} \partial_z H_x + V_x B_0 \qquad (2.72)$$

$$E_z = -\frac{1}{\sigma} \partial_y H_x \qquad (2.73)$$

and after substituting the value of H_y, H_z in Eq. 2.70, we obtain the TE mode expressions as

$$\partial_{yy}^2 E_x + \partial_{zz}^2 E_x = i\omega\mu_0\sigma E_x \qquad (2.74)$$

with

$$H_y = -\frac{1}{i\omega\mu_0} \partial_z E_x \qquad (2.75)$$

$$H_z = +\frac{1}{i\omega\mu_0} \partial_y E_x \qquad (2.76)$$

The TE mode expressions do not contain any term with velocity and magnetic field, which is a source term. The source is only present in the TM mode expressions. This indicates that a toroidal velocity field (when stream lines in horizontal plane) only creates an electromagnetic TM mode. It does not excite electromagnetic TE mode. The excitation of TE mode therefore demands a velocity field other than a toroidal field, we will back on this issue in the Section 2.6.

In the previous 1D case, we had only the two components of the electromagnetic field that is H_x and E_y. But in the present 2D case, we have three components that is H_x, E_y and E_z. The occurrence of E_z is a new feature, which is the result of the consideration $V_x = V_x(y, z)$. Introduction of a new term S, the horizontal wave number, is result this consideration. Let us evaluate the importance of this new term.
The Eq. 2.58 implies

$$H_x(y, z) = \bar{H}_x(z) \cos S y \qquad (2.77)$$

and from Eq. 2.73, we have

$$E_z = -\frac{1}{\sigma} \partial_y H_x$$

Inserting Eq. 2.77 into Eq. 2.78, we obtain

$$E_z = \frac{1}{\sigma} S \bar{H}_x \sin S y \qquad (2.78)$$

If $S = 0$, it is clear from Eq. 2.78 that E_z will be zero, which is the 1D case. Therefore, S should be greater than zero (i.e. $S > 0$) for the occurrence of E_z.

2.5 The TM Mode

In the previous section, we have observed $V_x(y, z) = \bar{V}_x(z) \cos S y$ creates only TM mode (H_x, E_y and E_z). The velocity expression represents a standing wave. For a detail study of TM mode, let us again repeat the assumptions

1. $V_x(y, z) = \bar{V}_x(z) \cos S y$ with $S > 0$ and $-\infty < y < +\infty$

2. $\sigma = \sigma(z) > 0$

3. $\vec{B} = B_0 \hat{z}$

Substituting Eq. 2.77 in Eq. 2.71 gives

$$-\frac{S^2}{\sigma}\bar{H}_x \cos(S y) + \partial_z(\frac{1}{\sigma}\partial_z\bar{H}_x)\cos(S y) = i\omega\mu_0\bar{H}_x \cos(S y) - B_0\partial_z\bar{V}_x \cos(S y) \qquad (2.79)$$

After a replacement and elimination of term $\cos(S y)$ from both the sides, we obtain

$$
\begin{aligned}
\partial_z(\frac{1}{\sigma}\partial_z\bar{H}_x) &= \frac{1}{\sigma}(S^2 + i\omega\mu_0\sigma)\bar{H}_x - B_0\partial_z\bar{V}_x \\
\partial_z(\frac{1}{\sigma}\partial_z\bar{H}_x) &= \frac{\alpha^2}{\sigma}\bar{H}_x - B_0\partial_z\bar{V}_x, \qquad \text{with } \alpha^2 = S^2 + i\omega\mu_0\sigma
\end{aligned}
\qquad (2.80)
$$

Here, α is the propagation constant. The constant α, consists of the two terms, a geometrical term S and an electromagnetic term $\sqrt{i\omega\mu_0\sigma}$, which takes care of the damping during the electromagnetic wave propagation. In order to solve the Eq. 2.80, we need boundary conditions. From Eq. 2.73, we have

$$\partial_y H_x = -\sigma E_z$$

In the air half space (i.e $z < 0$), as $\sigma = 0$, therefore H_x should be constant (say A). But as $H_x(y, 0) = \bar{H}_x(0) \cos(S y)$, this implies that $H_x(y, 0)$ will have different values for different places of y (for a fixed S). In order to satisfy the continuity of the vertical current density at air-ocean interface, the constant A must be equal to zero. Finally we obtain the conditions

1. $H_x = 0$,   at $z = 0$
2. $H_x = 0$,   at $z = \infty$

which we will use in the next section.

2.5.1 TM Mode Solution

The equation for the Green's function satisfying Eq. 2.80 can be written as

$$\partial_z(\frac{1}{\sigma}\partial_z G_H) = \frac{\alpha^2}{\sigma}G_H - \delta(z - z_0) \qquad (2.81)$$

Here, the Green's function G_H will follow a similar boundary condition as H_x. For the simplest conductivity distribution of a uniform earth half-space with $\sigma(z) = \sigma$, the Green's function G_H satisfying the above differential equation and boundary conditions is given by

$$G_H(z/z_0) = \frac{\sigma}{2\alpha}\left[e^{-\alpha|z-z_0|} - e^{-\alpha(z+z_0)} \right], \quad z, z_0 \geq 0 \tag{2.82}$$

Since $G_H(z = 0) = G_H(z = \infty) = \bar{H}_x(z = 0) = \bar{H}_x(z = \infty)$. After simplification, integration from $z = 0$ to $z = \infty$, gives

$$\bar{H}_x(z_0) = B_0 \int_0^\infty \partial_z \bar{V}_x \, G_H(z/z_0) \, dz \tag{2.83}$$

Let us solve the Eq. 2.83 for an assumed velocity structure, defined as

$$\bar{V}_x(z) = \begin{cases} 0 & \text{for } z < 0 \text{ and } z > d \\ V_0 & \text{for } 0 \geq z \geq d \end{cases} \tag{2.84}$$

then

$$\partial_z \bar{V}_x(z) = V_0[\delta(z) - \delta(z-d)] \tag{2.85}$$

Inserting the above value in Eq. 2.83, we have

$$\begin{aligned}
\bar{H}_x(z_0) &= V_0 B_0 \int_0^\infty [\delta(z) - \delta(z-d)] G_H(z/z_0) \, dz \\
&= V_0 B_0 \left[\int_0^\infty G_H(z/z_0)\delta(z) \, dz - \int_0^\infty G_H(z/z_0)\delta(z-d)] \, dz \right] \\
&= V_0 B_0 \left[G_H(0/z_0) - G_H(d/z_0) \right] \\
&= -V_0 B_0 \, G_H(d/z_0), \qquad \text{as } G_H(0/z_0) = 0
\end{aligned} \tag{2.86}$$

According to the assumption (1) and Eq. 2.72 and Eq. 2.73, the three components of the fields are

$$\begin{aligned}
H_x(y, z_0) &= \bar{H}_x(z_0) \, \cos(Sy) \\
&= -V_0 B_0 \, G_H(d/z_0) \, \cos(Sy)
\end{aligned} \tag{2.87}$$

$$E_y(y, z_0) = \left[\frac{1}{\sigma} \partial_z \bar{H}_x(z_0) + V_x B_0 \right] \cos(Sy) \tag{2.88}$$

$$E_z(y, z_0) = -\frac{S}{\sigma} \bar{H}_x(z_0) \, \sin(Sy) \tag{2.89}$$

Writing out the solution explicitly using Eq. 2.82,

For the zone $0 \leq z_0 \leq d$

$$H_x(y, z_0) \;=\; -V_0B_0\,\frac{\sigma}{\alpha}e^{-\alpha d}\,\sinh(\alpha z_0)\,\cos(Sy) \tag{2.90}$$

$$E_y(y, z_0) \;=\; +V_0B_0\left(1 - e^{-\alpha d}\cosh(\alpha z_0)\right)\,\cos(Sy) \tag{2.91}$$

$$E_z(y, z_0) \;=\; -V_0B_0\frac{S}{\alpha}\,e^{-\alpha d}\,\sinh(\alpha z_0)\,\sin(Sy) \tag{2.92}$$

For the zone $z_0 \geq d$

$$H_x(y, z_0) \;=\; -V_0B_0\,\frac{\sigma}{\alpha}e^{-\alpha z_0}\,\sinh(\alpha d)\,\cos(Sy) \tag{2.93}$$

$$E_y(y, z_0) \;=\; +V_0B_0\left(1 - e^{-\alpha z_0}\sinh(\alpha d)\right)\,\cos(Sy) \tag{2.94}$$

$$E_z(y, z_0) \;=\; -V_0B_0\frac{S}{\alpha}\,e^{-\alpha z_0}\,\sinh(\alpha d)\,\sin(Sy) \tag{2.95}$$

2.5.2 Results

The response of the TM Mode fields computed for an assumed model using MENA (Appendix-B) are shown in the Fig. 2.6. The fields are plotted on the log-scale for clarity reasons. Evidently, the fields B_x and E_z are zero at the ocean surface. The strength of these fields continuously increases within and decreases below the ocean i.e. in the sedimentary formation. At the ocean-floor, the E_z and the B_x field of a 10 km wavelength show respectively a weakest and strongest strength compared to the other two wavelengths (0.5 km and 2.2 km). The observations indicate that the damping of the fields B_x and E_z are different for different wavelengths. The observation demands a close attention to the damping issue, which we will detail in the Section 2.5.3. A significant change in the B_x and the E_z field can be observed at the ocean floor. The conductivity of both the formations (ocean and sedimentary layer) are identical (i.e. 3.33 S/m) and they differ only in their velocity state. Therefore observations suggest that the change at the floor is due to velocity change at the interface. It suggests that the B_x and E_z fields are indicators of the changes in the velocity field. We have already observed similar result for the B_x field during the study of one dimensional case. The E_z field is new in the respect, showing the potential to observe velocity changes. Moreover, the observations implies that the horizontal magnetic and the vertical electric fields at the floor will be distorted significantly due to their characteristic sensitivity for the changes in the velocity field. We have observed similar results in the practical observations too, which we will see in the next coming chapters.

Unlike B_x and E_z, the E_y is non-zero at the surface and shows a finite strength at the surface. One can observe continuous loss in the field strength as it proceeds in to the
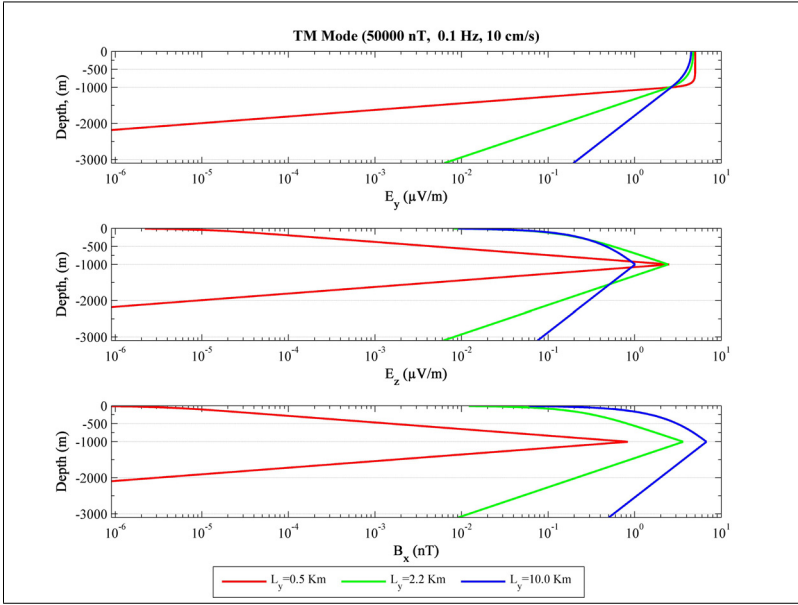
Figure 2.6: Figure showing the TM mode fields response computed at 0.1 Hz for a wave velocity of 0.1 m/s moving in a geomagnetic field of strength 50000 nT. On the top, middle and bottom, respectively the fields E_y, E_z and B_x are presented. Three colors (red, green and blue) in each panel represents the fields generated by the oceanic waves of wavelength 0.5, 2.2 and 10 km. The thickness of the ocean is 1000 m. Below the 1000 m depth the sediments extends which has same conductivity as ocean. Note, velocity with in the ocean is assumed constant

.

depth. Below the source region i.e. ocean, the decay of the field is prominent. Unlike B_x and E_z fields showing a change in response pattern at the floor, the response of the E_y field is smooth there. The observation indicates that the field is although sensitive to the velocity field, but is not an effective observer of the velocity changes.

2.5.3   Damping and Response Curve

The propagation and damping characteristics of a wave is controlled by a propagation constant. We have found the propagation constant as $\alpha = \sqrt{(S^2 + i\omega\mu_0\sigma)}$ (see Eq. 2.80). The electromagnetic damping term $i\omega\mu_0\sigma$ depends on the frequency of the oscillating wave and also it depends on the layer's characteristics like conductivity and magnetic permeability. On the other hand, the geometrical damping term S^2 only depends on the wavelength of an oscillating wave and is independent of the geological characteristics. To

visualise the effect of both the terms, let us apply two approximations,

1. Let $\omega = 0$. This will remove the electromagnetic (EM) damping and lead us to visualise only geometrical damping effects.

2. Let us assume a huge wavelength so that $S^2 \approx 0$. This will remove the geometrical damping and lead us to visualise only EM damping effects.

The obtained responses are shown in Fig. 2.7. The B_x and E_z field amplitude at the surface is zero but is not apparent because of the logarithmic scale plotting of the fields. We represent damping (geometrical + EM) by the solid line and geometrical damping (damping without EM damping) alone by the dotted line with cross symbols. Please note each panel contains four responses in total. Corresponding to 1 km wavelength, evidently in each panels (i.e. top: E_y field, middle: E_z field and bottom: B_x field) there exists a superimposition between the solid and the cross symbol dotted line. The superimposition of response is only possible when EM damping has no role and field experiences only geometrical damping. Unlike 1 km wavelength case, in the case of 10^{15} km wavelength evidently the symboled dotted cyan line and the solid cyan lines are distinct. For the case, the observation indicates for a significant role of the EM damping. The comparisons corresponding to a large and a small wavelength therefore suggest that the EM damping is significant for large waves and is negligible for small waves. Small waves only experience a geometrical damping.

The comparison corresponding to 1 km and 10^{15} km waves is equivalent to a comparison of situation $S \neq 0$ and $S \approx 0$, respectively. Please note the cyan and red solid lines in each panel. At a frequency of 0.01 Hz, when $S \approx 0$ (EM damping only), it is apparent in the bottom panel (i.e. B_x field) that the strength of the field is stronger than the corresponding to 1 km wavelength (i.e. $S \neq 0$). While, in the middle panel (i.e. E_z field), the strength is weaker for $S \approx 0$ than the $S \neq 0$. In the top panel, a comparison between $S \neq 0$ and $S \approx 0$ shows that the strength of the E_y field is weaker in the ocean but stronger in the below half-space for $S \approx 0$ case. Please note strength corresponding to the cyan solid line, which is weaker in ocean but stronger below it if compared with the red solid line. For an identical situation, with in the ocean the corresponding strength of the cyan solid lines are weaker, than the red solid lines, for the E_y and the E_z field but is stronger for the B_x field. The observation indicates that the B_x field experiences more geometrical damping in the ocean than E_y and E_z field.

We mentioned that the EM damping is significant for large waves, but how large is still matter of investigation. Let us observe the field strength at the ocean-floor for various waves at different frequencies. The obtained response patterns are shown in the Fig. 2.8. The red line represents the situation of geometrical damping (no EM attenuation). In general, smaller waves (< 1.5 km) experience only geometrical damping. The fields E_y and B_x experience the EM damping for a wave greater than 2 km while the length is even less and is 1.5 km for E_z field. A careful inspection of the response suggests a significant difference between E and B field. For small wavelengths, E-fields are constant

at the ocean-floor while B-field strengthens up with increase in the wavelength. This is an important result as B_x field might prove to be a tool in providing the wavelength information. Measurement at a place at two different depths, one at the ocean floor and other little above it may help in this regard.

2.5.4 The Static Field

The static field is a DC field which is measured at zero frequency (i.e. $\omega = 0$). This is also known as galvanic field. If $S = 0$ and $\omega = 0$, the field equations (see Eq. 2.90 to 2.95) are zero. In words, a static ocean without a wave will neither have a horizontal nor a vertical component of the electric field i.e. in general, no electric field. But, the case when $S > 0$, the DC field is no longer zero because of accumulation of the charges. Let us examine the DC state after substituting $\omega = 0$ in Eq. 2.90 to 2.95. We obtain non-zero fields with in the ocean and even below the ocean i.e.

For the zone $0 \leq z_0 \leq d$

$$H_x(y, z_0) = -V_0 B_0 \frac{\sigma}{S} e^{-Sd} \sinh(S z_0) \, \cos(S y) \tag{2.96}$$

$$E_y(y, z_0) = +V_0 B_0 \left(1 - e^{-Sd} \cosh(S z_0) \right) \cos(S y) \tag{2.97}$$

$$E_z(y, z_0) = -V_0 B_0 \, e^{-Sd} \sinh(S z_0) \, \sin(S y) \tag{2.98}$$

For the zone $z_0 \geq d$

$$H_x(y, z_0) = -V_0 B_0 \frac{\sigma}{S} e^{-S z_0} \sinh(S d) \, \cos(S y) \tag{2.99}$$

$$E_y(y, z_0) = +V_0 B_0 \left(1 - e^{-S z_0} \sinh(S d) \right) \cos(S y) \tag{2.100}$$

$$E_z(y, z_0) = -V_0 B_0 \, e^{-S z_0} \sinh(S d) \, \sin(S y) \tag{2.101}$$

This suggests that the accumulation of the charges may create a static potential field U such that $E = -\nabla U$, where

$$U(y, z_0) = \begin{cases} -\frac{B_0 V_0}{S} [1 - e^{-Sd}] \, e^{-S z_0} \sin(S y) & \text{for } z_0 \leq 0 \\[2mm] -\frac{B_0 V_0}{S} [1 - e^{-Sd} \cosh(S z_0)] \, \sin(S y) & \text{for } 0 \leq z_0 \leq d \\[2mm] -\frac{B_0 V_0}{S} [1 - e^{-S z_0} \sinh(S d)] \, \sin(S y) & \text{for } z_0 \geq d \end{cases} \tag{2.102}$$
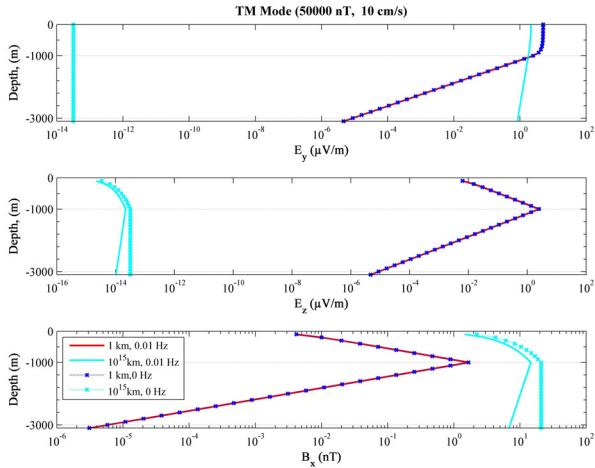
Figure 2.7: Figure for visualisation of the damping terms. The dotted and solid lines respectively represent zero and 0.01 Hz frequency. The responses with cross symbols represent only the damping by the geometrical attenuation. The response is computed for two different wavelengths that is 1 km and 10^{15} km. The B_x and E_z fields are zero at the surface (z=0) but is not evident in the figure because of the used log scale
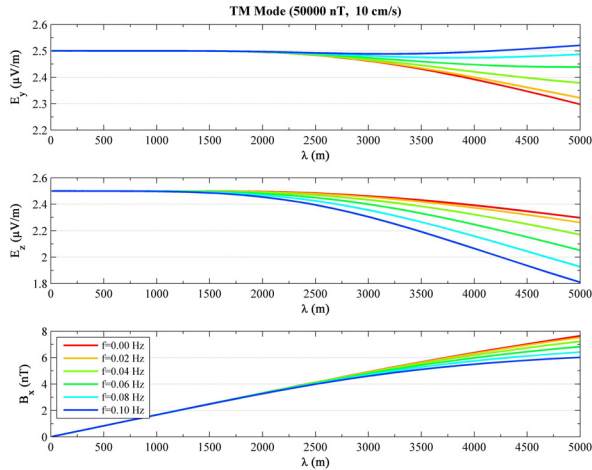

Figure 2.8: The fields strength observed at the at the ocean-floor for various wavelengths at different frequencies. Response is computed for 6 frequencies (0 to 0.1 Hz)

Now, since the potential is known, we can easily determine the electrical volume charges ρ_e and surface charges σ_e. As $\nabla \cdot \vec{E} = \rho_e/\epsilon_0$. So, the volume charge ρ_e is given as

$$
\begin{aligned}
\rho_e &= \epsilon_0 \nabla \cdot \vec{E} \\
&= \epsilon_0 \nabla^2 \cdot \vec{U} \\
&= \begin{cases} 0 & \text{for } z_0 < 0 \\ -B_0 V_0 S \, \epsilon_0 \sin(S\,y) & \text{for } 0 \leq z_0 \leq d \\ 0 & \text{for } z_0 > d \end{cases}
\end{aligned} \tag{2.103}
$$

and surface charge σ_e at $z = 0$, which causes a discontinuity in E_z is given as

$$
\begin{aligned}
\sigma_e &= \epsilon_0 \, [E_z]_{z=0^-}^{z=0^+} \\
&= -B_0 V_0 \epsilon_0 \left[1 - e^{-Sd} \right] \sin(S\,y)
\end{aligned} \tag{2.104}
$$

It is evident that electrical charges depend on the wavelengths (i.e. S) of the wave.

2.5.5   Physical situation in the static limit

The stream lines of the present velocity field $\vec{V}(y,z) = V_x(z) \cos(S\,y)\hat{x}$ are in the horizontal plane. The phases of the water waves are present in the y-direction. The velocity field will point in to the sheet at $y = 0$ and out of the sheet at $y = \pi/2S$. A diagrammatic representation is shown in Fig. 2.9. The velocity field situation is described in subsection I. Here, the filled and hollow circles represent the situation of velocity field pointing into and out of the sheet, respectively. We retain our initial assumptions, for simplicity, that the velocity is not varying with depth and the magnetic field is vertical. This shows that the motionally induced current density $\vec{J}_e = \sigma(\vec{V} \times \vec{B})$ will point in the y-direction and will form a divergent and convergent systems such that $\nabla \cdot \vec{J} \neq 0$. But conditionally $\nabla \cdot \vec{J} = 0$ i.e. the divergence of the current density in not allowed. Therefore, for the completion of the divergent current $\vec{J}_e$ system to a non-divergent $\vec{J}$ current system, surface and volume charges are required to create an electric field $\vec{E}$. This electric field will act such that $\vec{J} = (\sigma\vec{E} + \vec{J}_e)$ becomes a non-divergent system. The horizontal component of the created electric field $\vec{E}$ will point opposite to the direction of motionally induced field. The accumulated surface charges (at $z = 0$) will create the vertical component of the field.

With in the ocean ($0 \leq z_0 \leq d$) the components of the current density, are

$$
\begin{aligned}
J_y &= -B_0 V_0 \sigma e^{-Sd} \cosh(S\,z_0) \cos(S\,y) \tag{2.105} \\
J_z &= -B_0 V_0 \sigma e^{-Sd} \sinh(S\,z_0) \sin(S\,y) \tag{2.106}
\end{aligned}
$$

Below the ocean ($z_0 \geq d$) the components of the current density, are

$$
\begin{aligned}
J_y &= +B_0 V_0 \sigma e^{-Sz_0} \sinh(S\,d) \cos(S\,y) \tag{2.107} \\
J_z &= -B_0 V_0 \sigma e^{-Sz_0} \sinh(S\,d) \sin(S\,y) \tag{2.108}
\end{aligned}
$$

Therefore, the current density for $(0 < z_0 < \infty)$ will satisfy

$$\nabla \cdot \vec{J} \;=\; \partial_y J_y + \partial_z J_z \tag{2.109}$$

$$=\; 0 \tag{2.110}$$

As the derivative of J_y and J_z are,

$$\partial_y J_y \;=\; -B_0 V_0 \sigma S \, \sin(Sy)[-e^{-Sd} \cosh(Sz_0) + e^{-Sz_0} \sinh(Sd)] \tag{2.111}$$

$$\partial_y J_z \;=\; -B_0 V_0 \sigma S \, \sin(Sy)[+e^{-Sd} \cosh(Sz_0) - e^{-Sz_0} \sinh(Sd)] \tag{2.112}$$

2.5.6   TM Mode: Layered Model Green's Function $G_h(z/z_0)$

Let us assume a layered model shown in Fig. 2.10. Model consists of various conductivity discontinuities of different thicknesses. Let thickness of the ocean be d_1. The transmission of the field through various conductivity boundaries and its reflection from various interfaces can be governed by assuming a Green's function (for $0 \geq z \geq d_1$ and $0 \geq z_0 \geq d_1$).

$$G_h(z/z_0) = \frac{\sigma}{2\alpha}[e^{-\alpha|z-z_0|} + Ae^{-\alpha z} + Be^{+\alpha z}] \tag{2.113}$$

Here, A and B are constants. The constant A describes the field reflected from the surface $z = 0$ and stands for a downward diffusing field. The constant B describes the field reflected from the ocean bottom $z = d_1$ and stands for an upward diffusing field. Our aim is to determine constants A and B, which could be obtained using some boundary condition. As the the function $G_h(z/z_0)$ is zero at the surface, we can use this as our first boundary condition. Further, we find our second boundary condition from the continuity of the field at conductivity discontinuities. The continuity suggest a continuous transfer function (Weidelt 2007) $G_h(d_1/z_0) = -\frac{1}{\sigma b_m(d_1)}\partial_z G_h(d_1/z_0)$ with a transfer function b_m which can be determined via a recursion relation (Appendix A). Calculation for A and B in Eq. 2.113, using the above boundary conditions yields

$$A \;=\; -\frac{2R \sinh(\alpha z_0)}{R - e^{2\alpha d_1}} + e^{-\alpha z_0} \tag{2.114}$$

$$B \;=\; +\frac{2R \sinh(\alpha z_0)}{R - e^{2\alpha d_1}} \tag{2.115}$$

with R as,

$$R = \frac{\sigma(z)b_m(d_1) - \alpha}{\sigma(z)b_m(d_1) + \alpha} \tag{2.116}$$

The Greens function $G_h(z/z_0)$ for the layered model is now known. The value of $G_h(d_1/z_0)$ in the Eq. 2.87 will yields $H_x(y, z_0)$ for the layered case. Once $H_x(y, z_0)$ is known we can
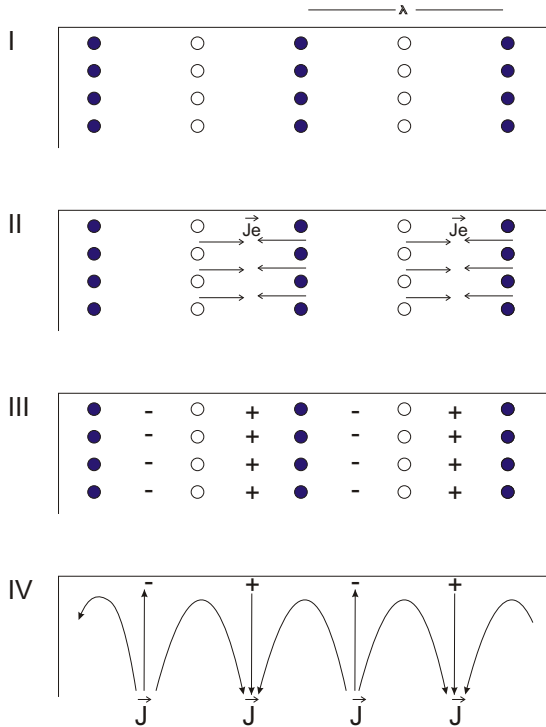
Figure 2.9: Schematic diagram representing the situation of current density for a static limit case. I) Represents the velocity field $\vec{V} = V_x\hat{i} = V_0 \cos(Sy)\hat{i}$. The filled and hollow circles respectively represent the velocity pointing into and out of the sheet. II) Represents the direction of the motionally induced current density. Evidently, there exist divergence and convergence of the current density. III) To satisfy the non-divergence condition $\nabla \cdot \vec{J} = 0$, the motionally induced current system demands generation of volume and surface charges to convert the system in to a non-divergent system. The charges leads to the creation of an electric field. The horizontal component of the field will be opposite to the motionally induced field. The vertical component of the field is created by the surface charges. IV) Represents the current line pattern in the ocean, for static limit case
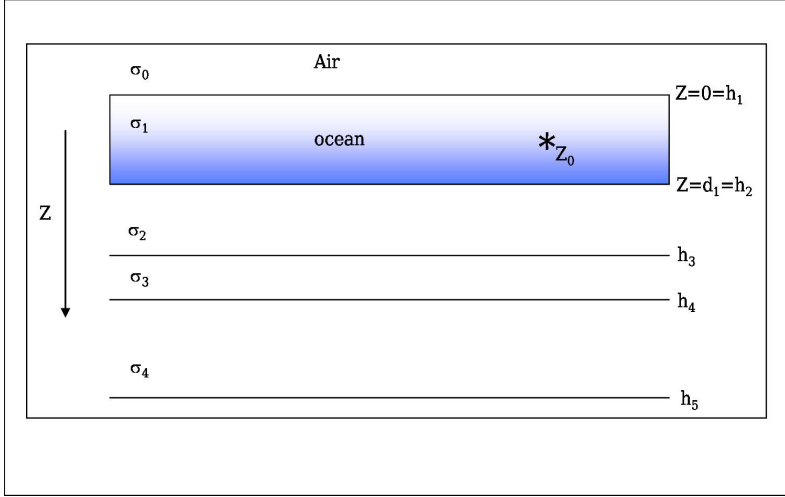
.

Figure 2.10: Sketch of a layered model used for defining the layered Green's function. Here, h_n and σ_n respectively represent the thickness and conductivity of the different layers. The star with Z_0 represents the observation position. Depth (z) is considered positive in downward direction.

easily calculate $E_y(z_0)$ and $E_z(z_0)$. Finally, we obtain

$$H_x(y, z_0) = -B_0 V_0 G_h(d_1/z_0) \cos(Sy) \tag{2.117}$$

$$
\begin{aligned}
E_y(y, z_0) &= +\left[\frac{1}{\sigma}\partial_z H_x(z_0) + V_0 B_0\right]\cos(Sy) \\
&= V_0 B_0 \left[1 - e^{\alpha d_1}\cosh(\alpha z_0) - \frac{2R\cosh \alpha z_0 \cosh \alpha d_1}{R - e^{2\alpha d_1}}\right]\cos(Sy)
\end{aligned}
\tag{2.118}
$$

$$E_z(y, z_0) = -\frac{S}{\sigma}B_0 V_0 G_h(z/z_0) \cos(Sy) \tag{2.119}$$

The equation's 2.117, 2.118 and 2.119 are the desired solution in TM mode for a layered earth. Let us observe the response corresponding to these fields.

2.5.7   Results

The segmentations of the used layered model for the response study are represented by the dotted lines. The conductivity of ocean, sediments and reservoir is assumed 3.33 S/m, 1 S/m and 0.01 S/m. Depth of the dynamic ocean is assumed 1000 m. A 1000 m thick layer of static sediments are assumed above and below the reservoir zone of thickness 100 m,
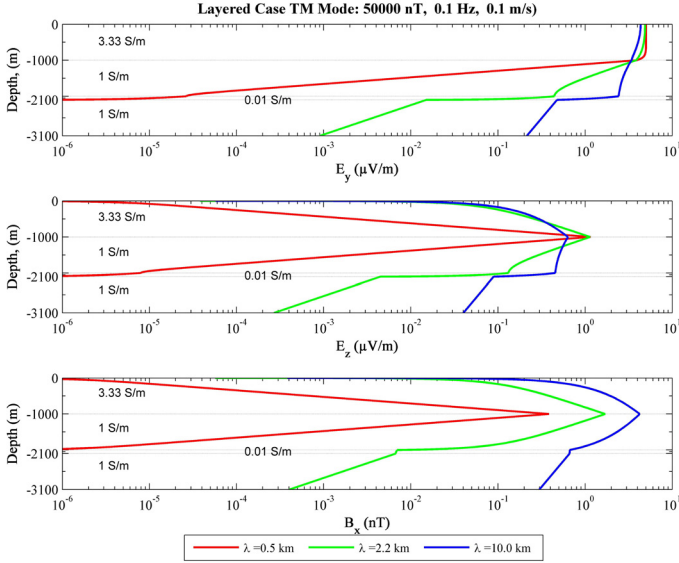
Figure 2.11: The response of the TM mode fields for a layered earth model. Computations are made for three wavelengths 0.5 km, 2.2 km and 10 km, which are respectively represented by red, green and blue lines. The conductivity values are shown in the corresponding layers of ocean (3.33 S/m), sediments (1 S/m), reservoir (0.01 S/m) and sediments (1 S/m). The horizontal dotted lines mark the boundary of the different formations.

which is present at the depth range 2000 m to 2100 m. Velocity of the ocean is assumed homogeneous (0.1 m/s). Vertical geomagnetic field strength is assumed 5×10^{-5} T. The obtained responses corresponding to wavelengths 0.5 km, 2.2 km and 10 km are shown in the Fig. 2.11. The half-space model (Fig. 2.6, see section 2.5.2) and the layered model (Fig. 2.11) responses with in the ocean are similar in behavior (not in amplitude). But below the ocean, as conductivity structures are different and therefore observed responses are different. In the reservoir zone, the difference is more prominent. Please note, all the three fields B_x, E_z and E_y are sensitive to the reservoir zone.

In the layered 1D case (Section 2.3.6), the E_y field was insensitive and only the B_x field was detecting the reservoir but in the present case, all the TM mode fields are sensitive to reservoir zone. This is because the present TM mode electric fields are derived from the horizontal magnetic field, which is sensitive to the reservoir zone. With the present result we are not claiming that the reservoirs detection is possible by the motion contributed TM mode signals. Our aim is only to show a plausible side.

The mCSEM spatial measurements are made at the ocean floor, which might be sen-
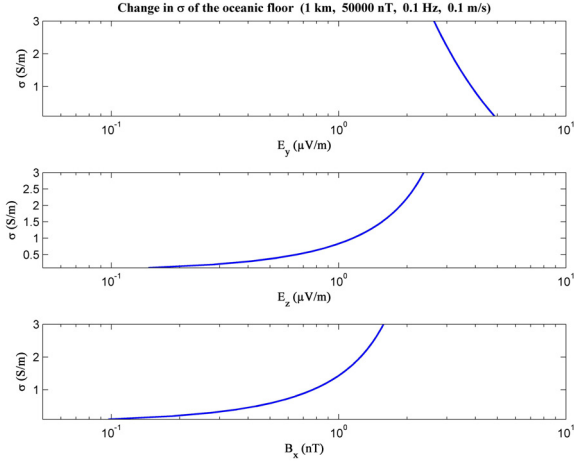
Figure 2.12: The B_x, E_z and E_y fields showing the influence of the changing conductivity of the ocean floor. For calculation the used parameters are frequency 0.1 Hz, velocity 0.1 m/s, wavelength 1 km and vertical geomagnetic field of 50000 nT.

sitive to the conductivity changes of ocean and oceanic floor as a function of the spatial locations. Two different experiments are done, one by changing the conductivity of the ocean floor and other by changing the conductivity of the ocean. For both the experiments, a wavelength of 1 km, vertical geomagnetic field of 5×10^{-5} T, frequency 0.1 Hz and homogeneous velocity of 0.1 m/s is assumed. The observations are made at the ocean floor (1000 m depth). The obtained fields responses by varying the ocean floor conductivity and ocean conductivity are shown in Fig. 2.12 and Fig. 2.13, respectively. In Fig. 2.12, the strength of the B_x and E_z fields are increasing while the E_y field is decreasing with the increase in the floor conductivity. On the other hand, in Fig. 2.13, the strength of the B_x and E_y fields are increasing while the E_z field is decreasing with the increase in the oceanic conductivity. In other words, an increase in the oceanic conductivity in the TM mode causes increase in the in the horizontal and decrease in the vertical electromagnetic fields. Please note that the B_x field is increasing in both the cases. The observation suggest that B_x field is more prone to distortion in the mCSEM/mMT recordings.

2.5.8   Layered Velocity Model

We have, till now assumed a model with a constant velocity field through out the oceanic depth. Let us now assume a layered velocity model shown in Fig. 2.14. From Eq. 2.83,
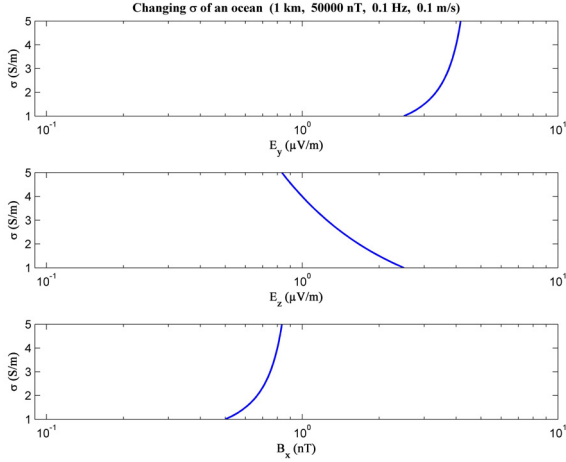
Figure 2.13: The B_x, E_z and E_y fields showing the influence of the changing conductivity of the ocean. For calculation the used parameters are frequency 0.1 Hz, velocity 0.1 m/s, wavelength 1 km and vertical geomagnetic field of 50000 nT.

we have

$$\bar{H}_x(z_0) = B_0 \int_0^\infty \partial_z \bar{V}_x \, G_H(z/z_0) \, dz$$

As the velocity field is confined to the zone $z = 0$ to $z = d$, therefore calculation by parts gives

$$
\begin{aligned}
\bar{H}_x(z_0) &= -B_0 \int_0^d \bar{V}_x \partial_z G_H(z/z_0) \, dz \\
&= -B_0 \sum_{i=1}^n V_i \left[G_H(H_i/z_0) - G(H_{(i-1)}/z_0) \right]
\end{aligned}
\tag{2.120}
$$

where,

$$G_H(H_i/z_0) = \frac{\sigma}{\alpha} e^{-\alpha H_i} \sinh(\alpha z_0) \quad \text{for } H_i \geq z_0 \geq 0 \tag{2.121}$$

$$G_H(H_i/z_0) = \frac{\sigma}{\alpha} e^{-\alpha z_0} \sinh(\alpha H_i) \quad \text{for } z_0 \geq H_i \tag{2.122}$$

Using Eq. 2.87, Eq. 2.88 and Eq. 2.89, we get the final expression as

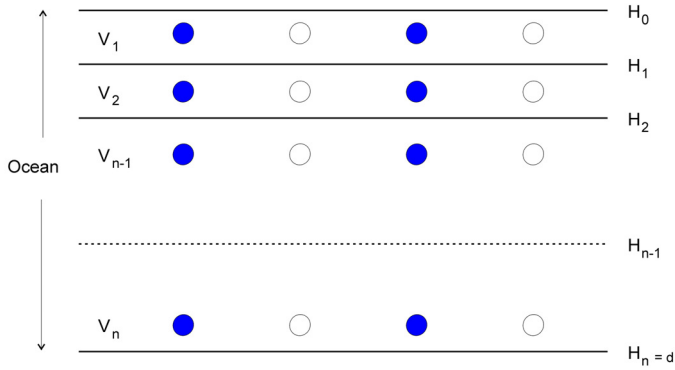**For the zone** $0 \leq z_0 \leq H_r$, r representing the depth index corresponding to the receiver

45

Figure 2.14: Schematic view of the n-layered ocean. The entities $V_1, V_2, ..., V_n$ represent the velocity in the layers with depths $H_1, H_2, ..., H_n$, respectively. The total oceanic depth is d. The filled and hollow circles respectively represent the velocity pointing into and out of the sheet

.

depth.

$$H_x(y, z_0) = -B_0 \sum_{i=1}^{r} V_i \left[G_H(H_i/z_0) - G(H_{(i-1)}/z_0) \right] \cos(Sy) \tag{2.123}$$

$$= -B_0 \sum_{i=1}^{r} V_i \left[\frac{\sigma}{\alpha} (e^{-\alpha H_i} - e^{-\alpha H_{i-1}}) \sinh(\alpha z_0) \cos(Sy) \right. \tag{2.124}$$

$$E_z(y, z_0) = \frac{S}{\sigma} B_0 \sum_{i=1}^{r} V_i \left[G_H(H_i/z_0) - G(H_{(i-1)}/z_0) \right] \sin(Sy) \tag{2.125}$$

$$= -B_0 \sum_{i=1}^{r} V_i \left[\frac{S}{\alpha} (e^{-\alpha H_i} - e^{-\alpha H_{i-1}} \sinh(\alpha z_0) \sin(Sy) \right. \tag{2.126}$$

$$E_y(y, z_0) = \left[B_0 V_r - B_0 \partial_z \left(\sum_{i=1}^{r} \frac{V_i}{\sigma} (G_H(H_i/z_0) - G(H_{(i-1)}/z_0)) \right) \right] \cos(Sy) \tag{2.127}$$

For $0 \leq z_0 \leq d$, **within the ocean**

$$E_y(y, z_0) = [B_0 V_r - B_0 \sum_{i=1}^{r} V_i (e^{-\alpha H_i} - e^{-\alpha H_{i-1}}) \cosh(\alpha z_0)] \; \cos(Sy) \qquad (2.128)$$

For $z_0 \geq d$, **below the ocean**

$$E_y(y, z_0) = [-B_0 \sum_{i=1}^{r} V_i (e^{-\alpha H_i} - e^{-\alpha H_{i-1}}) \cosh(\alpha z_0)] \; \cos(Sy) \qquad (2.129)$$

For the zone $z_0 \geq H_r$, r representing the depth index corresponding to the receiver depth.

$$H_x(y, z_0) \;\; = \;\; -B_0 \sum_{i=r}^{n} V_i \, [\frac{\sigma}{\alpha} e^{-\alpha z_0} (\sinh(\alpha H_i) - \sinh(\alpha H_{i-1}))] \; \cos(Sy) \quad (2.130)$$

$$E_z(y, z_0) \;\; = \;\; -B_0 \sum_{i=r}^{n} V_i \, [\frac{S}{\alpha} e^{-\alpha z_0} (\sinh(\alpha H_i) - \sinh(\alpha H_{i-1}))] \; \sin(Sy) \quad (2.131)$$

For $0 \leq z_0 \leq d$, **within the ocean**

$$E_y(y, z_0) = [B_0 V_r - B_0 \sum_{i=r}^{n} V_i \, e^{-\alpha z_0} (\sinh(\alpha H_i) - \sinh(\alpha H_{i-1}))] \; \cos(Sy) \qquad (2.132)$$

For $z_0 \geq d$, **below the ocean**

$$E_y(y, z_0) = [-B_0 \sum_{i=r}^{n} V_i \, e^{-\alpha z_0} (\sinh(\alpha H_i) - \sinh(\alpha H_{i-1}))] \; \cos(Sy) \qquad (2.133)$$

2.5.9   Results

A five layer velocity model is used for the response study. The assumed velocities for the depth zones 0-200 m, 200-300 m, 300-400 m, 400-700 m and 700-1000 m are 0.1 m/s, 0.08 m/s, 0.06 m/s, 10^{-4} m/s and 10^{-6} m/s, respectively. Conductivity within and below the ocean is assumed constant and is 3.33 S/m. The obtained responses for the E_y, E_z and B_x fields are shown in the top, middle and bottom panel of the Fig. 2.15. The E_z and B_x fields are zero at the surface but is not evident in the figure because of the log scale plotting. In former case of constant velocity model (see Fig 2.6), we observed maximum strength of the B_x field at the ocean bottom. But this is not the case with the layered velocity model. The B_x field shows a maximum strength at the depth 400 m and thereafter a rapid decay in the field strength is evident with increase in the depth. Please note, the upper and lower adjoining boundary of 400 m depth holds velocity 0.06 m/s and 0.0001 m/s, respectively. Moreover, the response shows a change in the slope at depth 300 m and 400 m due to the velocity gradient at these depths. The depths 700 m and 1000 m (at ocean floor) although also hold a velocity gradients but the absence of any
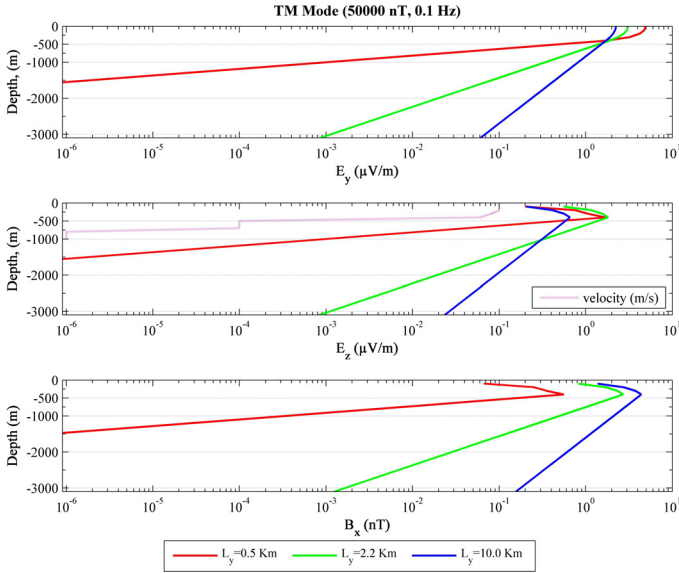
Figure 2.15: Figure showing the TM mode fields response at 0.1 Hz, computed for a constant geomagnetic field of 50000 nT. A velocity model (shown in the middle plot in magenta) is used for the computation. On the top, middle and bottom, respectively the fields E_y, E_z and B_x is presented. Three colors (red, green and blue) in the each plot represents the fields generated by the oceanic waves of wavelength 1, 10 and 100 km. The thickness of the ocean is 1000 m. Below the 1000 m depth the sediments extends.

.

observable slope change suggest that the distinguishable change is only offered with a significant velocity gradient. Evidently, the field strength significantly depends on the wavelength. The largest wavelength (10 km) of the B_x field holds maximum strength with in and below the ocean compared to other two wavelengths (0.5 Km and 2.2 Km). Like the B_x field, the E_z field also shows a maximum field strength and changes in slopes at similar depths. But they (B_x and E_z fields) are dissimilar in their wavelength based strengths. The E_z field holds maximum strength with in the ocean (at 400 m depth) for 2.2 km wavelength. Comparative to 2.2 km and 10 km response, the 0.5 km response shows a rapid decay below 400 m depth which is due to a prominent geometrical damping (see subsection 2.5.3). All the three wavelengths responses of the E_z field show the maximum strength at 400 m depth. Among these three, minimum strength at this depth is offered by the largest wavelength (10 km) response. To understand the observation please see Eq. 2.126 which suggests that the E_z fields depends on S. The observation therefore suggests that other than the damping factor, the geometry (wavelength) of a wave also

play a role deciding the field strength. The E_y field, unlike B_x and E_z fields, shows a continuous decrease in strength with the increasing depth. At the ocean floor (1000 m depth) the minimum and maximum strengths are evident corresponding to 0.5 km and 10 km wave. The observation suggests that compared to small waves, a larger waves hold stronger strength of E_y field at the ocean floor.

2.6 The TE mode

In the previous section we have seen that a velocity vector which lies in a horizontal plane $\vec{V} = V_x(y,z)\hat{x}$ only creates a TM Mode. Therefore to create a TE mode field, we assume a velocity field

$$\vec{V}(y,z) = \nabla \times [w(y,z)\,\hat{x}] \tag{2.134}$$

$$= \partial_z w(y,z)\,\hat{y} - \partial_y w(y,z)\,\hat{z} \tag{2.135}$$

which lies in the (y,z)-plane. Here, w is a stream function given as (Lamb 1932)

$$w = -\frac{V_0}{S} \sinh[S(d-z)]\cos(Sy + \omega t) \tag{2.136}$$

with d and ω representing the ocean depth and the angular frequency, respectively. The conservation of mass is satisfied with the satisfaction of the divergence condition $\nabla\cdot\vec{V} = 0$. Please note that the assumed velocity field satisfies the divergence condition. The current density will be

$$\vec{J} = \sigma(\vec{V} \times \vec{B}_0) \tag{2.137}$$

$$= \sigma B_0\,\partial_z w(y,z)\,\hat{x} \qquad \text{for, } \vec{B}_0 = B_0\,\hat{z} \tag{2.138}$$

in the x-direction. The mode decomposition assuming $\partial_x \equiv 0$ creates an electromagnetic field consisting of the three components E_x, H_y and H_z. From Eq. 2.11 and Eq. 2.12,

$$\nabla \times \vec{H} = \sigma\,(\vec{E} + \vec{V} \times \vec{B}_0)$$
$$\nabla \times \vec{E} = -i\omega\mu_0\,\vec{H}$$

follows,

$$\partial^2_{yy}\,E_x + \partial^2_{zz}\,E_x = i\omega\mu_0\sigma\,E_x + B_0\,\partial_z w \tag{2.139}$$

$$H_y = -\frac{1}{i\omega\mu_0}\,\partial_z\,E_x \tag{2.140}$$

$$H_z = +\frac{1}{i\omega\mu_0}\,\partial_y\,E_x \tag{2.141}$$

We assume $w(y, z) = \bar{w}(z) cos(S y)$, with S is a horizontal wave number in the y-direction, equal to $2\pi/\lambda_y$, where λ_y represents the wavelength. This implies $E_x(y, z) = \bar{E}_x(z) cos(S y)$. Substituting these value in Eq. 2.139 gives

$$\partial_{yy}^2 \bar{E}_x \; cos(S y) + \partial_{zz}^2 \bar{E}_x \; cos(S y) = i\omega\mu_0\sigma \bar{E}_x \; cos(S y) \; + \; B_0 \partial_z \bar{w} \; cos(S y) \qquad (2.142)$$

After a replacement and elimination $cos(S y)$ from both the sides, we obtain

$$\begin{aligned} \partial_{zz}^2 \bar{E}_x &= [S^2 + i\omega\mu_0\sigma(z)]\bar{E}_x + i\omega\mu_0\sigma(z)B_0 \; \partial_z\bar{w} \\ \partial_{zz}^2 \bar{E}_x &= \alpha^2 \bar{E}_x + i\omega\mu_0\sigma(z)B_0 \; \partial_z\bar{w}, \qquad \alpha^2 = S^2 + i\omega\mu_0\sigma \end{aligned} \qquad (2.143)$$

Here, α is the propagation constant with geometrical and electromagnetic term. The field E_x will be zero at limits $+\infty$ and $-\infty$. The Eq. 2.143 can be solved by means of the Green's function $G_e(z/z_0)$ satisfying

$$\partial_{zz}^2 G_e(z/z_0) = \alpha^2 G_e(z/z_0) - \delta(z - z_0) \qquad (2.144)$$

with the same limits as the field E_x i.e. $G_e(z/z_0)$ is zero at $+\infty$ and $-\infty$. We obtain,

$$\bar{E}_x(z_0) = -i\omega\mu_0 B_0 \int_0^\infty \sigma(z)\partial_z\bar{w}G_e(z/z_0)dz \qquad (2.145)$$

This is the solution of the Eq. 2.142.

2.6.1 Green's Function

The Eq (2.145) involves a Green's function $G_e(z/z_0)$. The function for a simple case of two uniform half-space, containing earth half-space ($z > 0$) with $\sigma(z) = \sigma$ and air-half-space ($z < 0$) with $\sigma(z) = 0$, can be written as

$$G_e(z/z_0) = \begin{cases} \frac{1}{2\alpha}[e^{-\alpha|z-z_0|} + \frac{\alpha-S}{\alpha+S}e^{-\alpha(z+z_0)}] & \text{for } z, z_0 \geq 0 \\ \\ \frac{1}{\alpha+S}e^{Sz_0-\alpha z} & \text{for } z \geq 0, z_0 \leq 0 \end{cases} \qquad (2.146)$$

2.6.2 Surface Gravity Waves

The assumed velocity field $\vec{V}(y, z)$ lies in the (y,z)-plane. The surface gravity waves could be treated as an example corresponding to the assumed velocity field $\vec{V}(y, z)$. From Eq. 2.134, we obtain

$$\begin{aligned} V_y &= \partial_z w - \partial_x w && (2.147) \\ &= V_0 \cosh[S(d - z)] \cos(S y + \omega t) && (2.148) \end{aligned}$$

and

$$V_z = \partial_x w - \partial_y w \qquad (2.149)$$
$$= V_0 \sinh[S(d-z)] \sin(Sy + \omega t) \qquad (2.150)$$

At the ocean bottom $z = d$, the normal component of the velocity will be zero. Thus

$$V_z(z = d) = 0 \qquad (2.151)$$
$$V_y(z = d) = V_0 \cos(Sy + \omega t) \qquad (2.152)$$

The displacement ψ_y and ψ_z of a particle is

$$\partial_t \psi_y = V_y \qquad (2.153)$$
$$\partial_t \psi_z = V_z \qquad (2.154)$$

Integration of the above equation gives

$$\psi_y(t) = +\frac{V_0}{\omega} \cosh[S(d-z)] \sin(Sy + \omega t) \qquad (2.155)$$
$$\psi_z(t) = -\frac{V_0}{\omega} \sinh[S(d-z)] \cos(Sy + \omega t) \qquad (2.156)$$

If $a(z) = \frac{V_0}{\omega} \cosh[S(d-z)]$ and $b(z) = \frac{V_0}{\omega} \sinh[S(d-z)]$ such that $b(z)/a(z) = 0$ at $z = d$. The elimination of the trigonometric function from Eq. 2.155 and Eq. 2.156 yields

$$\left(\frac{\psi_y}{a}\right)^2 + \left(\frac{\psi_z}{b}\right)^2 = 1 \qquad (2.157)$$

This is the equation of an ellipse, representing the elliptical trajectory of the water particles with axes as $a(z)$ and $b(z)$. For two different times i.e. $t_1 = 0$ and $t_2 = (\pi/2\omega)$, various y-positions of the particle at the ocean surface($z = 0$) are shown in Fig. 2.16. It is evident, for a wavelength $\lambda_y = 2\pi/S$, the crest position of the particle for $t_1 = 0$ and $t_2 = (\pi/2\omega)$ is respectively at $y = 2\pi/S$ and $y = 3\pi/2S$. Therefore, the time difference between the same phase is

$$\Delta t = \frac{\pi}{2\omega} \qquad (2.158)$$

and position difference is

$$\Delta y = -\frac{\pi}{2S} \qquad (2.159)$$

The phase velocity is

$$\frac{\Delta y}{\Delta t} = \frac{-\frac{\pi}{2S}}{\frac{\pi}{2\omega}} \tag{2.160}$$

$$V_{ph} = -\frac{\omega}{S} \tag{2.161}$$

Evidently, the phase velocity is inversely proportional to the wavenumber S or directly proportional to the wavelength λ_y. Therefore larger waves would have higher phase velocity. The important property of the surface wave is that the frequency and wavelength is coupled by the dispersion relation
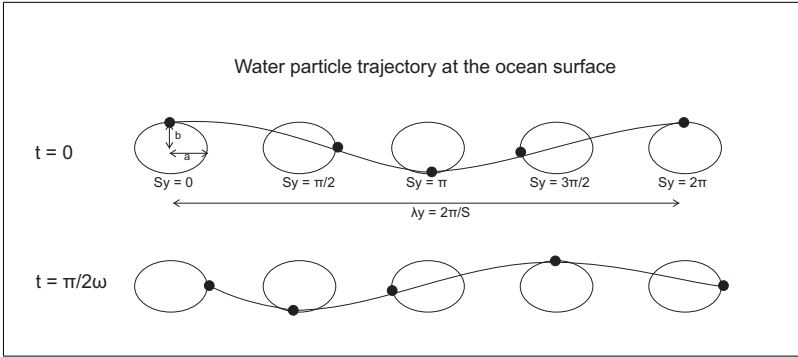

Water particle trajectory at the ocean surface

$t = 0$

$Sy = 0$ $Sy = \pi/2$ $Sy = \pi$ $Sy = 3\pi/2$ $Sy = 2\pi$

$\lambda y = 2\pi/S$

$t = \pi/2\omega$

Figure 2.16: Schematic diagram representing the particle situation at time $t = 0$ and $t = (\pi/2\omega)$ for various position of y. The line connecting the focii of the ellipse represents the surface i.e. $z = 0$

.

$$\omega^2 = gS \tanh(S d) \tag{2.162}$$

where, $g = 9.81 m/s^2$ is the acceleration due to gravity and d is the ocean depth. The Eq. 2.145 can be easily calculated for a earth half-space by using Eq. 2.146 and Eq. 2.148. The substitution gives,

$$
\begin{aligned}
\bar{E}_x(z_0) = & - i\omega\mu_0\sigma B_0 V_0 \frac{1}{2\alpha} \int_0^d [e^{-\alpha|z-z_0|} + \frac{\alpha - S}{\alpha + S} e^{-\alpha(z+z_0)}] \cosh[S(d-z)]dz \\
= & - \frac{1}{2} B_0 V_0 \Big[2\cosh[S(d-z_0)] - e^{-\alpha(d-z_0)} - \frac{\alpha - S}{\alpha + S} e^{-\alpha(d+z_0)} \\
& - \frac{2S}{\alpha + S} e^{(Sd-\alpha z_0)} \Big]
\end{aligned} \tag{2.163}
$$

The magnetic field is

$$\bar{H}_y(z_0) = -\frac{B_0 V_0}{2i\omega\mu_0}\Big[-2S\,\sinh[S(d-z_0)] - \alpha e^{-\alpha(d-z_0)} + \alpha\frac{\alpha-S}{\alpha+S}e^{-\alpha(d+z_0)}$$
$$+\frac{2\alpha S}{\alpha+S}e^{(Sd-\alpha z_0)}\Big] \tag{2.164}$$

$$\bar{H}_z(z_0) = +\frac{S}{\omega\mu_0}\bar{E}_x(z_0) \tag{2.165}$$

A time dependent surface elevation in a flow is a prominent aspect of the surface waves. Therefore, instead of V_0, the strength of surface waves will be described more appropriately by the wave height h_w, as it is an observable quantity. From Eq. 2.148, we have

$$V_y = V_0 \cosh[S(d-z)]\cos(Sy+\omega t) \tag{2.166}$$

At $z = d$, $V_z = 0$ (Eq. 2.150). Therefore, V_0 is the amplitude of V_y at the ocean floor $z = d$. At the surface $z = 0$, V_y would attain much bigger amplitude $V_0\cosh(Sd)$. As Eq. 2.156 reads

$$\psi_z(t) = -\frac{V_0}{\omega}\sinh[S(d-z)]\cos(Sy+\omega t) \tag{2.167}$$

Therefore

$$h_w = \frac{V_0}{\omega}\sinh(Sd) \tag{2.168}$$

Solving for V_0 yields,

$$V_0 = \frac{\omega h_w}{\sinh(Sd)} \tag{2.169}$$

Inserting Eq. 2.169 in Eq. 2.163, Eq. 2.164 and Eq. 2.165 gives

$$\bar{E}_x(z_0) = -\frac{\omega h_w B_0}{2\sinh(Sd)}\Big[2\cosh(S(d-z_0))$$
$$- e^{-\alpha(d-z_0)} - \frac{\alpha-S}{\alpha+S}e^{-\alpha(d+z_0)} - \frac{2S}{\alpha+S}e^{(Sd-\alpha z_0)}\Big] \tag{2.170}$$

$$\bar{H}_y(z_0) = -\frac{h_w B_0}{2i\sinh(Sd)\mu_0}\Big[-2S\,\sinh[S(d-z_0)]$$
$$- \alpha e^{-\alpha(d-z_0)} + \alpha\frac{\alpha-S}{\alpha+S}e^{-\alpha(d+z_0)} + \frac{2\alpha S}{\alpha+S}e^{(Sd-\alpha z_0)}\Big] \tag{2.171}$$

$$\bar{H}_z(z_0) = +\frac{S h_w}{\sinh(Sd)\mu_0}\bar{E}_x(z_0) \tag{2.172}$$

the desired solution of the TE mode fields. The graphs illustrating the behavior of the fields are shown in the Fig. 2.18.

2.6.3   TE Mode: Layered Model Green's Function $G_e(z/z_0)$

Let us repeat the assumed layered model shown in the Fig. 2.10. Model contains various electrical formations of different thicknesses. Let the depth of the ocean be d_1. Let us assume a Green's function $G_e(/z/z_0)$ for $0 \geq z \geq d_1$ and $0 \geq z_0 \geq d_1$, which can account the transmitted and reflected signals by the various electrical formations

$$G_e(z/z0) = \frac{1}{2\alpha}[e^{-\alpha|z-z_0|} + Ae^{-\alpha z} + Be^{\alpha z}] \tag{2.173}$$

Here, A and B are constants. The constant A corresponds to the field reflected from the surface $z = 0$ and stands for a downward diffusing field. While the constant B corresponds to the field reflected from the ocean bottom $z = d_1$ and stands for a upward diffusing field. The constants A and B can be determined using the transfer function a_e and b_e (Weidelt 2007) which at $z = 0$ and $z = d_1$ yields $G_e(0/z_0) = +\frac{1}{\mu_0 a_e(0)}\partial_z G_e(0/z_0)$ and $G_e(d_1/z_0) = -\frac{1}{\mu_0 b_e(d_1)}\partial_z G_e(d_1/z_0)$, respectively. The positive and negative signs cares the amplitude of the upward and downward propagating waves as they respectively increases and decreases with the depth. The transfer function a_e is equal to S/μ_0 and b_e is determined via a recursion relation (Appendix A). Solving the Eq. 2.173 for A and B using the above two boundary conditions give

$$A = \frac{R_d e^{-\alpha(d_1-z_0)} - e^{\alpha(d_1-z_0)}}{R_0 e^{\alpha d_1} - R_d e^{-\alpha d_1}} \tag{2.174}$$

$$B = -(AR_0 + e^{-\alpha z_0}) \tag{2.175}$$

with

$$R_0 = \frac{\mu_0 b_e(0) - \alpha}{\mu_0 b_e(0) + \alpha} \tag{2.176}$$

$$R_d = \frac{\mu_0 b_e(d_1) - \alpha}{\mu_0 b_e(d_1) + \alpha} \tag{2.177}$$

The Greens function for the layered earth is now known. The Eq. 2.145 can be written as

$$\bar{E}_x(z_0) = -i\omega\mu_0 B_0 \int_0^{d_1} \sigma(z)V_0 \cosh[S(d_1 - z)]G_e(z/z_0)dz \tag{2.178}$$

Conductivity of the ocean is assumed constant. If we assume a constant velocity in the ocean, the Eq. 2.178 becomes

$$\bar{E}_x(z_0) = -i\omega\mu_0\sigma B_0 V_0 \int_0^{d_1} \cosh[S(d_1 - z)]G_e(z/z_0)dz \tag{2.179}$$

Inserting the value of $G_e(z/z_0)$ in the Eq. (2.179) yields $\bar{E}_x(z_0)$ and with $\bar{E}_x(z_0)$ known, we can easily calculate $\bar{H}_y(z_0)$ and $\bar{H}_z(z_0)$. Finally, we get

$$\bar{E}_x(z_0) = -\frac{V_0 B_0}{2\alpha}\Big[2\alpha \cosh[S(d_1 - z_0)] - \alpha e^{-\alpha(d_1 - z_0)} - e^{-\alpha z_0}[\alpha \cosh(S d_1) + S \sinh(S d_1)]$$
$$+ \alpha \cosh(S d_1)[A - B] - S \sinh(S d_1)[A + B] - A\alpha e^{-\alpha d_1} + B\alpha e^{\alpha d_1}\Big] \quad (2.180)$$

$$\bar{H}_y(z_0) = +\frac{V_0 B_0}{2i\alpha\omega\mu_0}\Big[-2S\alpha \sinh[S(d_1 - z_0)] - \alpha^2 e^{-\alpha(d_1 - z_0)}$$
$$+ \alpha e^{-\alpha z_0}[\alpha \cosh(S d_1) + S \sinh(S d_1)] + \alpha \cosh(S d_1)[\partial_z A - \partial_z B]$$
$$- S \sinh(S d_1)[\partial_z A + \partial_z B] - \partial_z A\alpha e^{-\alpha d_1} + \partial_z B\alpha e^{\alpha d_1}\Big] \quad (2.181)$$

$$\bar{H}_z(z_0) = -\frac{S}{i\omega\mu_0}\bar{E}_x(z_0) \quad (2.182)$$

Renormalising the above equation in terms of wave height h_w by replacing V_0 using the Eq. 2.169 yields

$$\bar{E}_x(z_0) = -\frac{\omega h_w B_0}{2\alpha \sinh(S d_1)}\Big[2\alpha \cosh[S(d_1 - z_0)]$$
$$- \alpha e^{-\alpha(d_1 - z_0)} - e^{-\alpha z_0}[\alpha \cosh(S d_1) + S \sinh(S d_1)]$$
$$+ \alpha \cosh(S d_1)[A - B] - S \sinh(S d_1)[A + B] - A\alpha e^{-\alpha d_1} + B\alpha e^{\alpha d_1}\Big] \quad (2.183)$$

$$\bar{H}_y(z_0) = +\frac{\omega h_w B_0}{2i\alpha\omega\mu_0 \sinh(S d_1)}\Big[-2S\alpha \sinh[S(d_1 - z_0)] - \alpha^2 e^{-\alpha(d_1 - z_0)}$$
$$+ \alpha e^{-\alpha z_0}[\alpha \cosh(S d_1) + S \sinh(S d_1)] + \alpha \cosh(S d_1)[\partial_z A - \partial_z B]$$
$$- S \sinh(S d_1)[\partial_z A + \partial_z B] - \partial_z A\alpha e^{-\alpha d_1} + \partial_z B\alpha e^{\alpha d_1}\Big] \quad (2.184)$$

$$\bar{H}_z(z_0) = -\frac{S}{i\omega\mu_0}\bar{E}_x(z_0) \quad (2.185)$$

2.6.4 Results

We studied the TE mode responses for the two different models i.e. a) half-space model and b) layered model using MENA (Appendix-B). The sketch of these models along with various parameters value are shown in Fig. 2.17. For two different wavelengths of 1 km and 100 km, each of 1 m height, the responses are computed over these two models and are shown in the Fig. 2.18. The fields analogous to 1 km and 100 km wavelength are plotted respectively in the left and the right panels. The wavelengths and frequencies in
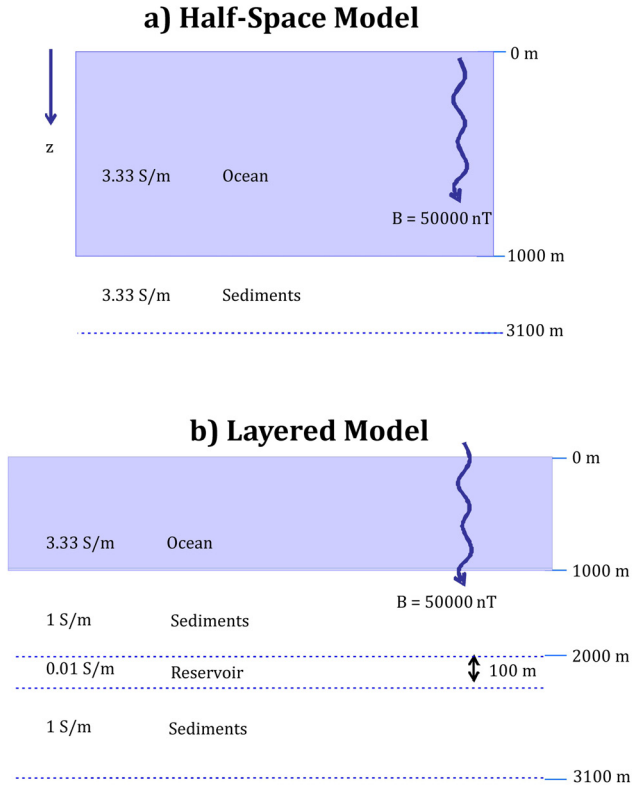
55

a) Half-Space Model

b) Layered Model

Figure 2.17: Sketch of two models used for the calculation of TE mode responses. **Top:** a) Half-space model, the model consists of a dynamic ocean and static sediments, each of conductivity 3.33 S/m. **Bottom:** b) Layered model, the model contains layers of ocean, sediments, reservoir and sediments of conductivities 3.33 S/m, 1 S/m, 0.01 S/m and 1 S/m, respectively. The thickness of the sedimentary layer above and below the 100 m thick reservoir zone is 1000 m. For both the models, the depth of the ocean and strength of the vertical geomagnetic field is respectively assumed 1000 m and 50000 nT.
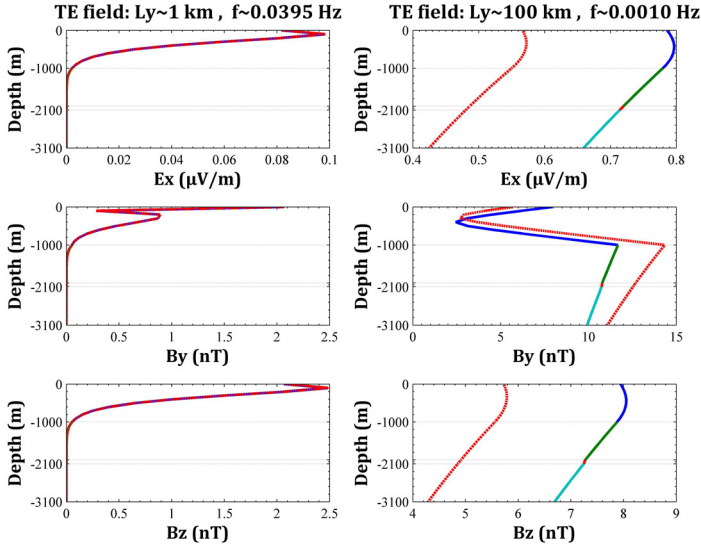
.

Figure 2.18: Figure showing the TE mode response of the fields for two different wavelengths of 1 km and 100 km. The responses corresponding to 1 km and 100 km wavelengths are shown in the left and right panels, respectively. The E_x, B_y and B_z fields are respectively presented in the top, middle and bottom panels. Each panel contains the two response curves analogous to half space model and layered model respectively represented by the dotted red line and multi-color solid lines. The change in color of solid line denotes the change in geological formations assumed in the layered model

.

the TE mode are coupled by the dispersion relation (Eq. 2.162), suggesting 0.0395 Hz and 0.001 Hz with the wavelengths of 1 km and 100 km, respectively. Please note, each panel contains the two responses, one represents the half-space (dotted red line) and other represents the layered model (solid multi-color line). These two responses superimpose each other for case of 1 km wavelength but are distinct for 100 km wavelength case. The superimposition implies that there is no difference between the half-space and the layered model response and therefore suggesting that the 1 km wave is not capable to reach the ocean floor. In addition, the horizontal electric and vertical magnetic field first gradually increases with in the ocean to a maximum and thereafter it gradually decreases. As conductivity of the ocean is homogeneous (i.e. 3.33 S/m) and therefore the increase in field strength indicates for a source process. Due to the assumed velocity of elliptical trajectory, which lies in the (y,z) plane, a horizontal electric field E_x is created in the vertical geomagnetic field which will show maximum strength at the foci depth of the

ellipse. The strength to the explanation is further provided by the observation of maximum strength of the E_x field at depths of 85 m, 170 m, 255 m, 340 m and 425 m for 1 km, 2 km, 3 km, 4 km and 5 km wavelengths, respectively (results are not shown). Please note for every a kilometer increase in wavelength leads 85 m increase in depth. These calculations are made for model parameters (both half-space and layered model) shown in Fig. 2.17.

The B_z field senses y-derivative of the E_x field (Eq. 2.141) and therefore it will follow the same pattern like the E_x field. The horizontal magnetic field B_y is sensitive to the vertical derivative of the E_x field and therefore causing a gradual decrease leading to a minimum close to the maximum of E_x field (also see Chave (1983)). Please note the responses corresponding to the 100 km wavelength (right panel fields), here depth of maximum and minimum strength for half-space and layered model are different because large wavelengths are capable to read the vertical conductivity structure. Moreover, the depth of minimum (please see the B_y field) response for layered model is greater than the half-space model, again because of the vertical conductivity structure. The cause of the effect is reflection and transmission of the waves due to various conductivity discontinuities.

3 The Data Analysis

3.1 The marine Controlled Source Electromagnetic (mC-SEM) Method

The marine Controlled Source Electromagnetic (mCSEM) method is an offshore survey-ing technique which provides geological information and fluid properties (Chave *et al.* 1991). In recent years, this technique has been used mostly for hydrocarbon exploration (Ellingsrud *et al.* 2002; Eidesmo *et al.* 2010) in conjunction with seismic (Weitemeyer *et al.* 2006). Seismic method traces a geological structure while mCSEM defines the content of a reservoir (Hesthammer & Boulaenko 2005; Christensen & Dodds 2007). The integrated interpretation of mCSEM with seismic is a proven tool to reduce exploration risk (Camara *et al.* 2007; Edwards 2005).

The mCSEM data acquisition methodology is shown in Fig. 3.1. In practice, an elec-tromagnetic transmitter is towed close to the sea floor to maximize the coupling of electric and magnetic field with sea floor rocks. A transmitter (T) transmits the EM field which couples with the surrounding and is recorded by receivers (R) deployed on the sea floor. The obtained signals are further processed to extract the concealed geological informa-tions (particularly of hydrocarbon reservoir interest). The data acquisition practice in both time and frequency domain of mCSEM is well documented in the article by Constable & Srnka (2007).

Generally, the characteristic reservoir signal in the mCSEM data is found small (Ei-desmo *et al.* 2010; Constable & Srnka 2007; Constable & Key 2006) and thus even small noise can be important in the context. The prime aim of the present data analysis is the un-derstanding of these noise sources, which create the oceanic background electromagnetic field.

3.2 Oceanic Waves

For an oceanic background electromagnetic field, a knowledge of the oceanic waves are significant as they play prime role in the field creation. Waves are created because of the action of the forces. It would be therefore appropriate to classify the oceanic waves genesis based on the forces (LeBlond & Mysak 1978; Mei 1989), which are as follows:
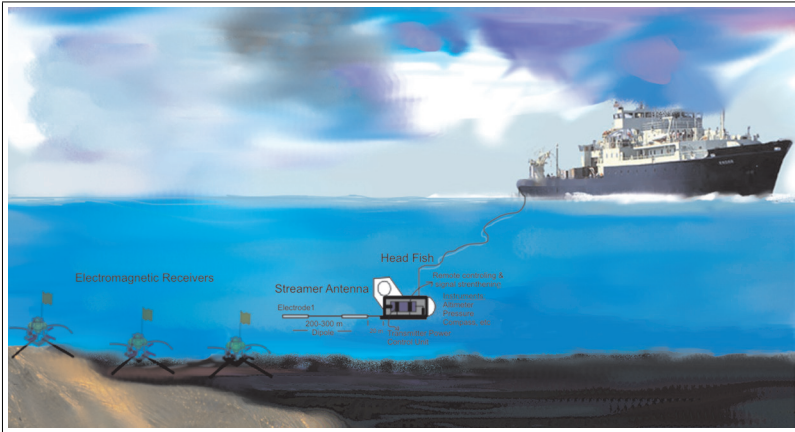
Figure 3.1: Schematic diagram showing the field layout for mCSEM sounding. An electromagnetic transmitter unit, which is towed close to the ocean floor with the data acquisition vessel, comprises a head fish and a streamer antenna. The streamer antenna connects the end of dipole electrodes via two cables and the head fish contains the power unit and instrumentation. The orthogonal dipole antennas and two induction coil magnetometers of the electromagnetic receives unit, placed at the floor, measures the horizontal components of the electric and the magnetic field, respectively.

1. The restoring action of the gravity, acting of the water particles, creates gravity waves.

2. At the contact of two different fluids (air and water), surface tension acts as a restoring force and creates a capillary wave.

3. The Coriolis force creates inertial or gyroscopic waves.

4. The change in latitude or depth causes a change in equilibrium position and leads to a large scale oscillation known as planetary or Rossby waves.

5. The slight compressible nature of the oceanic water waves allows the existence of sound waves.

All the above mentioned different forces act simultaneously. In combination they produce complicated and mixed type of oscillations. With the naked eye, we observe these mixed oscillations at the ocean surface known as surface waves (LeBlond & Mysak 1978). Surface waves involve a very broad range of wavelength and time period. Their classification based on the time period is shown in Table-3.1.

The mCSEM interest lies in the frequency range between 10 to 0.01 Hz. We will confine detail of the oceanic waves therefore in this range only. Particularly, two waves

Table 3.1: **Classification of the surface waves** (Reddy 2001; Sundermann 1994; Pinet 2006)

Wave Type	Period Range	Frequency	Wavelength	Restoring Force
Capillary Waves	< 0.1 s	> 10 Hz	2 cm	Surface tension (ST)
Ultra Gravity Waves	0.1 - 1 s	1 - 10 Hz	1 m	ST and Gravity
Gravity Waves (Chop, Swell etc)	1 - 30 s	0.03 - 1 Hz	1 - 100 m	Gravity
Infra-gravity Waves	30 s - 5 min	0.003 - 0.03 Hz	10 m - 10 km	Gravity and Coriolis
Long Period Waves (Seiche, Tsunami etc)	5 min - 12 hr	0.00003 - 0.003 Hz	up to some 100 km	Gravity and Coriolis
Tidal Waves	12 - 24 hr	1×10^{-5} - 3×10^{-5} Hz	up to some 1000 km	Gravity and Coriolis
Trans-tidal Waves	>24.8 hr	<0.00001 Hz	up to some 1000 km	Gravity and Coriolis

namely gravity waves and infra-gravity waves (Webb *et al.* 1991) are in the probable list (see Table-3.1). We are excluding ultra gravity waves as they can not influence electromagnetic recording near to the ocean floor because of their high frequency nature. The gravity and infra-gravity waves require a common force for their generation, which is gravity. The restoring action by the gravity attempts to control the instability (created by a wind) on the water surface due to the tangential drag that consequently lead to a formation of a surface wave in the ocean. The genesis scenario suggests four prime factors controlling the size and type of these waves:

1. Wind velocity

2. Wind duration

3. Area of the prevailing wind (fetch)

4. Original sea state

Once the waves are created, they grow until they obtain their maximum. The maximum is decided by wind speed and fetch. Swell is a one example of such a wave which originates at a remote location by the action of wind/storm (Pinet 2006). At a considerable distance

from the origin, they attain their full development and posses no further growth. With increasing distance swell looses its energy and height because of geometrical spreading, adverse winds obstructs and energy loss by friction with atmosphere. The wave-wave interaction some times lead in the generation of a long wave known as infra-gravity wave (Carter 1988).

3.3   Microseisms

Microseism is like a soft earth tremor originating with in the ocean by non-linear interaction of oceanic waves, which causes a continuing oscillation of the ocean floor. The broad frequency range for microseisms are between 0.05 to 1 Hz (Kedar *et al.* 2008), which mainly depends on the ocean depth and oceanic conditions. Longuet-Higgins (1950) proposed a mechanism for microseisms and showed that if two identical progressive waves traveling in opposite directions interact with each other, there is a second order pressure term effect which does not vanish with depth and can thus reach the deep ocean bottom. Consider two surface waves of frequencies f_1 and f_2, moving with approx. the same velocity in opposite direction. Let the wave number of frequencies be respectively k_1 and $-k_2$. Interaction of these waves will leave behind a wave with very small wave number (i.e. $k_1 + (-k_2)$ = diminutive) and very large wavelength. The large wavelength is capable of creating a pressure disturbance effectively at the ocean floor. The amplitude of the pressure disturbance is proportional to the product of the interacting wave heights and the frequency. These pressure fluctuations in the water column might then excite Rayleigh waves in the solid earth and be observed as microseisms. In short, the favorable oceanic conditions for microseisms generation are:

1. Shoreline geological setting creating ground for nonlinear interaction of surface waves.

2. Near shore reflection of high frequency surface waves and thereafter head on interaction.

3. A fast moving storm creating a sequence of wave in different directions.

4. High frequency wave interaction may generate whitecaps (a wind blown wave whose crest is broken and appears white), which leads to acoustic energy transmission to ocean bottom.

The depth of the ocean is another important factor in the creation of microseisms. The wave generation in the ocean depends on the wind velocity. Velocity of the ocean wave (V) is, approximately, (gD) where D is ocean depth and g is acceleration due to gravity. Therefore, for a 4 km deep ocean and a 500 m shallow ocean, the velocity V is approximately 200 m/s and 70 m/s respectively. A typical wind velocity rarely exceeds a few tens of m/s. This suggests wind velocities are quite close to the oceanic velocities especially

in the shallow oceans. Therefore the generation of microseisms are likely to be efficient in shallow oceans (Tanimoto 2005).

As we discussed in section-3.2 that storm thousands of kilometer away from the seashore creates swell. The distance allows the waves comprising of the swells to become more stable, clean, and continuous. For microseisms generation, in general, higher frequency waves are more efficient than the lower frequency waves like swell. Swells are more directional and therefore chances for non-linear interactions are not as much as of higher frequency gravity waves (Webb & Cox 1986), which are generated with in the ocean by the influence of gravity at the interface involving the density contrast. Microseisms are a time localized feature, the duration of which depends on the time of effective nonlinear wave interaction.

3.4 Aim of the analysis and data

As mentioned earlier, the characteristic reservoir signals in mCSEM data are very small and thus small noise can even perturb the signal. The present study is therefore intended to
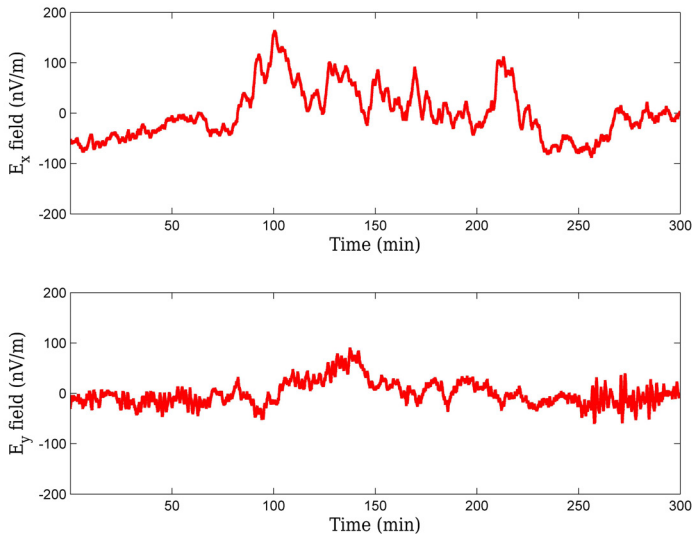

Figure 3.2: Five hour times-series of two orthogonal horizontal components of the electric field. E_x (top) and E_y (bottom). The x-axis makes -8° with respect to North (angle in clockwise direction). The recording is made at the sea floor, approx. 500 m below the sea surface.

understand the oceanic background electromagnetic noise sources, which may facilitate in enhancing the probability of reservoir detection. The oceanic waves and various oceanic features could motionally create electromagnetic field. We started the chapter with the short introductory knowledge (like oceanic waves and microseisms) and now can proceed for the data analysis.

We utilised mCSEM electric field data set, which was provided to us by KMS Technologies - KJT Enterprises Inc. The data was recorded in December 2006. Recording was made at the ocean-floor at a depth of approximately 500 m. To study the electromagnetic oceanic background noise, we analyzed only those segments where the transmitter was not active. Components of the horizontal electric field of such a segment are shown in Fig. 3.2. Evidently, the amplitude of E_x in a certain bandwidth corresponding to the visible range is larger than E_y. Since the electric field can be created by the oceanic movements and therefore to investigate the field strength correspondence with the velocity field let us recall Section 2.1, which suggest that in a stationary frame of reference electric field creates the current density given by

$$\vec{J} = \sigma(\vec{E} + \vec{V} \times \vec{B}_0) \tag{3.1}$$

where, σ is the conductivity of the ocean, σE is the current density generated by both galvanic and inductive processes and $\sigma \vec{V} \times \vec{B}_0$ is the source current term for the field creation. In the component form, Eq. 3.1 can be written as,

$$J_x = \sigma(E_x + V_y B_z - V_z B_y) \tag{3.2}$$
$$J_y = \sigma(E_y + V_z B_x - V_x B_z) \tag{3.3}$$

We write only the horizontal current densities (skipped J_z component) as in mCSEM only the horizontal electric fields are measured. The recordings are made at the ocean-floor and therefore we make simplified consideration that V_z is very very small. Elimination of the terms involving V_z simplifies the horizontal current density as,

$$J_x = \sigma(E_x + V_y B_z) \tag{3.4}$$
$$J_y = \sigma(E_y - V_x B_z) \tag{3.5}$$

Finally, we obtain,

$$E_x = -\left(\frac{1}{\sigma} J_x + V_y B_z\right) \tag{3.6}$$

$$E_y = +\left(\frac{1}{\sigma} J_y + V_x B_z\right) \tag{3.7}$$

Noticeably, the velocity V_x and V_y are the source for the field E_y and E_x, respectively. We obtain an equation suggesting that V_x and V_y principally controls the strength of the E_y and E_x, respectively. We observe $E_x > E_y$ in the time series (Fig. 3.2), which suggests V_y

$> V_x$. Further, normally the surface wave moves towards the coast. Accordingly, in the continental shelf and slope region the velocity component pointing towards the coast may have higher velocity than the other horizontal component. The present data is recorded with a setting that the y-component of the receiver points towards the cost and constructs an angle of approx. 55° with it. The setting suggests $V_y > V_x$. Based on above two reasoning, we presume that $V_y > V_x$.

3.5 Time-Series Analysis

A time-series of the horizontal electric fields E(t), is shown in Fig. 3.2. This is a stochastic time-series as the future electric field is only partially dependent on past values and cannot be predicted exactly. Such a time-series E(t) can be expressed in frequency domain E(f) in terms of the amplitude and phase via the Fourier Transform (Bendat & Piersol 1986)

$$E(f) = \int_{-\infty}^{\infty} E(t)e^{-i2\pi f t} \, dt \qquad (3.8)$$

As the time-series E(t) is a finite time-series E(n) of length N with a uniform sampling interval Δt of 20 ms. The Eq. 3.8 can be expressed in terms of the Discrete Fourier Transform as

$$E(f) = \sum_{n=0}^{N-1} E(n)e^{-i2\pi kn/N} \qquad k = 0, 1, 2, ..., N-1 \qquad (3.9)$$

Using Euler's formula in complex polar notation

$$E(k) = \sum_{n=0}^{N-1} E(n)\left(\cos\frac{2\pi kn}{N} - i\sin\frac{2\pi kn}{N}\right) \qquad k = 0, 1, 2, ..., N-1 \qquad (3.10)$$

$$= I(k) - iQ(k) \qquad k = 0, 1, 2, ..., N-1 \qquad (3.11)$$

with

$$I(k) = \sum_{n=0}^{N-1} E(n)\cos\frac{2\pi kn}{N} \qquad (3.12)$$

$$Q(k) = \sum_{n=0}^{N-1} E(n)\sin\frac{2\pi kn}{N} \qquad (3.13)$$

The Fourier-coefficients I(k) and Q(k) are the basis of Fourier-based spectral analysis. However, the direct calculation of these coefficients using Eq. 3.12 and 3.13 is particularly inefficient because of large time consumption. The Fast Fourier transform (FFT) (Cooley and Tukey, 1965) is the most efficient method for the calculation. The Eq. 3.11 provides

the electric field values corresponding to the frequencies f_k, where

$$f_k \quad = \quad \frac{k}{N\Delta t} \tag{3.14}$$

$$= \quad \frac{kf_s}{N} \tag{3.15}$$

Therefore, the quantity f_s/N defines a frequency resolution with f_s as sampling frequency. To understand the frequency content of the time-series E(t), we calculated the power spectral density (PSD) by determining the auto-spectrum. The one sided PSD can be defined as

$$P(k) \quad = \quad \frac{\Delta t}{N}|E(k)|^2 \qquad \text{for } k = 0 \text{ and } N/2 \tag{3.16}$$

$$= \quad \frac{2\Delta t}{N}|E(k)|^2 \qquad \text{for } k = 1, 2..., (N/2) - 1 \tag{3.17}$$

The phase (in radian) corresponding to each frequency can be expressed as

$$\theta(k) = \tan^{-1}\frac{Q(k)}{I(k)} \qquad \text{for } k = 0, 1, 2..., (N/2) \tag{3.18}$$

The phase $\theta(k)$ of a single time-series is a random entity and therefore it has no statistical importance. The detailed steps followed for the calculation of a PSD are as follows:

1. **Inspection of time-series**: Inspection is done to recognize glitches or other outliers in the data that are not consistent with the rest of the time-series.

2. **Detrending**: We subtracted the mean and any linear trend from the time-series to ensure that the energy at the lower end of the frequency scale do not dominate.

3. **Windowing**: Because of the finite length of the time-series, a distortion due to spectral leakage was observed in the PSD. To minimize this leakage a Hanning taper (Shin & Hammond 2008) is applied. This introduces a decrease in the spectral power.

4. **Calculation of the Fast Fourier Transform**

5. **Calculation of PSD**: PSD is calculated using time averaging method (Welch 1967).

6. **Smoothing**: To increase the reliability and decrease the variance, smoothing is done.

7. **Scaling**: To compensate the decrease in the spectral power due to windowing effect (item: 3), a correction factor of $\sqrt{8/3}$ (Shin & Hammond 2008) is applied.

The PSD for E_x and E_y is shown in Fig. 3.3. A general trend of power increase with decrease in frequency can be observed. Based on the power growth, four different slopes
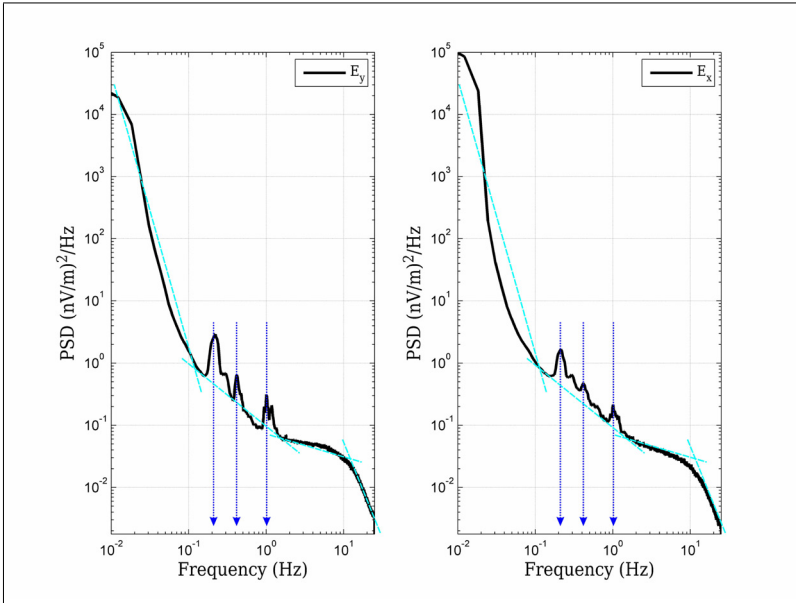
Figure 3.3: The log-log plot showing PSD of the two horizontal electric components. E_x (left) and E_y (right). Anomalous peaks are visible at 0.2, 0.4 and 1 Hz. Four slopes (cyan dashed lines) are marked in the spectra for discussion.

can be alienated in both E_x and E_y PSD's. Let the slope involving band of frequencies between 0.01 - 0.1 Hz, 0.1 - 2 Hz, 2 - 10 Hz and 10 - 25 Hz represent lower, intermediate, sub-high and high spectral range, respectively. Evidently for decreasing frequencies, a sharp power rise in the high spectral range (10-25 Hz) can be noticed, which might be a result of digitization noise (Chave & Filloux 1984). The sub-high spectral range (2-10 Hz) is nearly flat in slope. A flat PSD, generally, corresponds to a field which contains equal power within a fixed bandwidth which resembles noise. The intermediate range (0.1-2 Hz) contains three distinct peaks at 0.2, 0.4 and 1 Hz. The power in this range has a significant rise, representing involvement of high power. The PSD slope is approximately f^{-1}. A much higher rise in the PSD slope is observed in the lower spectral range (0.01-0.1 Hz). Here, the PSD shows a f^{-3} dependence. Differences in the slopes are indicative that different spectral bands are gaining their power from different sources or combination of them. Possible sources energizing different spectral bands are listed in Table-3.2, which will be justified later in the corresponding section of the spectral band. Principally, the major portion of the oceanic energy is, evidently encompassed in two major spectral ranges, namely lower and intermediate range.

Table 3.2: **Spectral Range and Possible Sources:** Top row defines the spectral ranges and respective column contains the possible sources.

Lower	Intermediate	Sub-high	High
0.01 - 0.1 Hz	0.1 - 2 Hz	2 - 10 Hz	10 - 25 Hz
1. External Field	1. Mud Volcano	Noise	Digitization noise
2. Eddies	2. Microseisms	(complex seismic	
3. Infra-gravity waves	3. Gravity waves	background noise)	
4. Microseisms			

3.5.1   Lower Spectral Band (0.01 - 0.1 Hz)

In the lower spectral band (Fig. 3.3) the significant observations are:

1. PSD of $E_x > E_y$.

2. There exist a sharp rise in spectral power compared to other three spectral bands.

As in section 3.4, we have presumed V_y greater than V_x to support greater strength of E_x than E_y and data acquisition setting. Obviously, same reasoning satisfies the first observation. The second observation might be expected as an effect of two origins. External (outside ocean) origin and internal (within ocean) origin. The external electromagnetic field contribution is via the induction process by the magnetospheric and ionospheric current system (Cox 1980). The electromagnetic damping exponentially reduces the field amplitude, which becomes $1/e$ of the surface amplitude at a skin depth (δ)

$$\delta \approx 500 \sqrt{\frac{1}{\sigma f}} \qquad \delta \text{ in m, if conductivity } \sigma \text{ in } S/m \text{ and frequency } f \text{ in Hz} \qquad (3.19)$$

This implies,

$$f = \frac{76,000}{\delta^2} \qquad \text{for an ocean of 3.3 S/m } (f \text{ in Hz and } \delta \text{ in m}) \qquad (3.20)$$

At the ocean-floor, therefore only those external fields can make contribution which have frequencies less than or equal to $76,000/D^2$, where D is the ocean depth (in meters). We made the recordings approximately at 500 m depth. The external contribution at this depth should be less than 0.3 Hz (Eq. 3.20). Since the current spectral band encompasses frequencies lower than 0.3 Hz and therefore, influence by the external field is expected.

Involvement of the internal contributions are equally expected as oceanic features like eddies, infra-gravity waves and microseisms can contribute appreciable power to the present spectral band.

The sharp rise in the electric field power is also noticed by Cox (1981) and Chave & Filloux (1984) and they presumed oceanic eddy as cause. Eddies form when a bend in a surface current lengthens and eventually makes a loop. Looping supports the separation of the eddy from the main current. Eddy leads the swirling water which last for at least a few months and can contribute significant electromagnetic field. They are therefore expected to empower the present spectral band. Like oceanic eddy, infra-gravity waves could also supply a considerable power. Infra-gravity waves are more directional than eddies. The strong strength of E_x PSD implies involvement of a directional source and therefore suggests for their powerful inputs. Microseisms (Kedar *et al.* 2008) can also contribute energy to the present spectral band.

3.5.2   Intermediate Band (0.1 - 2 Hz)

Three distinct peaks corresponding to 0.2, 0.4 and 1 Hz can be observed is the PSD (Fig. 3.3). Most likely, they are internally contributed because of the restrictive spectral skin depth. There could be three main source processes which may contribute these spectral peaks. They are volcanoes, microseisms and gravity waves.

There is a known mud volcano at some distance from the data acquisition area. In an analysis of Stromboli volcano, a significant strength in the range 0.2 - 0.5 Hz is found (De Lauro *et al.* 2006). We do observe peaks in this spectral range. Mud-volcano therefore could be presumed as a plausible source for the peaks at 0.2 and 0.4 Hz.

The energetic type of microseisms occur in frequency band 0.1 - 1 Hz (Kedar *et al.* 2008). This creates a possibility that one/some of the peak/s is/are contributed by microseisms. This looks plausible as the data was acquired in a shallow ocean (500 m), where high frequency microseisms are plausible. Generally, high frequency waves are less directional and can easily go through a non-linear interaction. These interaction might create a sufficient long wavelength to reach to the ocean bottom to produce microseisms. The large wavelength of microseisms makes it directional in nature. This suggests microseisms might influence field component measurements depending on its direction.

Gravity waves might contribute an oscillatory field at the ocean bottom. Oscillations in turn will generate an electromagnetic field, which is sensed by the electric field sensors. It is easy to differentiate gravity waves from mud-volcanoes and microseisms as the first is time ambient while the last two show a temporary nature in time.

3.5.3   Results (from Section: 3.5.1 & 3.5.2)

Table- 3.2 provides a summary of the possible sources in various spectral bands. The sub-high (2-10 Hz) and high (10-25 Hz) spectral ranges are probably noise. Particularly, frequencies in the sub-high range holds equal power (flat PSD) and therefore suggestive

of a random signal i.e. noise, probably a contribution by the seismic background signals. The seismic signals from different directions (by the various sources like topographic frictions, man made cultural noises etc) may superimpose to a complex signal, more or less like a random noise. Ramblingly, the power rise in the high spectral range is rapid that it can not be by natural means and therefore is probably a digitization noise (Chave & Filloux 1984 and Peterson 1993).

In the lower spectral band (0.01-0.1 Hz), only with the PSD information it is difficult to isolate a major source among external field, eddies and infra-gravity waves. The directional analysis, of the observations, can possibly provide some clue. The observation (1) (in Section-3.5.1) supports $E_x > E_y$ in the PSD. Microseisms effectively explain the high power of the E_x field compared to the E_y field. But despite that we are now excluding microseisms from possible source list because microseisms will create an oscillation in a narrow band such that they would offer a spectral peak (not a broad range) in the spectrum. We do not observe any spectral peak in the lower band.
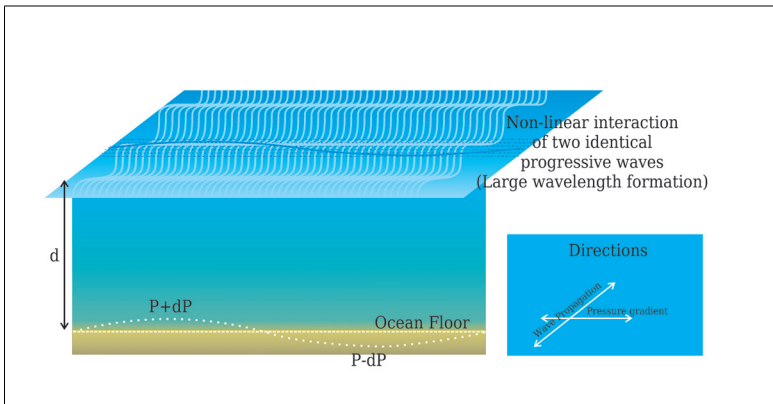
Figure 3.4: Idealistic diagram showing the mechanism of microseisms generation. The interaction of two identical progressive waves, traveling in the opposite direction leads to a long wavelength creation, which creates a pressure difference at the ocean floor. Please note orthogonal direction of wave propagation and pressure gradient with respect to each other.

In the intermediate spectral band (0.1-2 Hz), all the three peaks hold strong power in the E_y component (than E_x component). The mechanism of microseisms generation suggests that electric field will hold maximum power in the component perpendicular to the wave propagation direction (Fig. 3.4). This information suggests for $V_x > V_y$. But the previous consideration is $V_x < V_y$ (see Section-3). Microseisms violates the previous consideration and thus is a doubtful source. But before rejecting completely, it would be justified to observe the time characteristics of the peaks.

3.6   Time-series Splitting and Corresponding PSD's

Time based characteristics of a source can be evaluated by splitting a time series. Each time segment yields a different spectrum. If the source is time ambient, a spectral peak will be observed in each spectrum otherwise, the peak is a temporary source contribution. We divide the five hour time-series in to three equal segments, each of 100 minute length. The segmented time-series is shown in Fig. 3.5. Corresponding to each segment the obtained PSD is shown in Fig. 3.6.
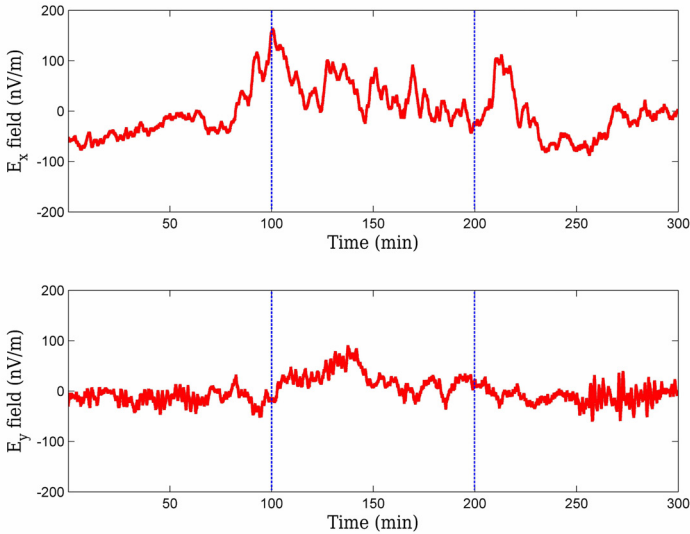
Figure 3.5: Figure showing three segments of the splitted five hour times-series. Ex (top) and Ey (bottom). The length of the each segment is 100 minutes. The splitting is denoted with vertical blue dashed lines.

Evidently, the lower spectral band is consistent with the previous observations (also see Fig. 3.3). No further significant observation can be noticed in all the three spectra. In the intermediate spectral band, we can observe a peak corresponding to 0.3 Hz, which was less clear in the Fig. 3.3. The peak at 0.3 Hz can be spotted in all the three spectra i.e. I, II, and III. In the I and III, its presence is noticeable but in the II it is hazy and slightly masked due to the strong adjacent peak at 0.2 Hz. The spectral peak at 0.3 Hz is the only peak to show its presence in all the three spectra and therefore indicating their contribution by a time ambient source. Gravity waves are therefore a likely explanation. To check this hypothesis, we will be back with a modeling of the gravity waves in the later section.
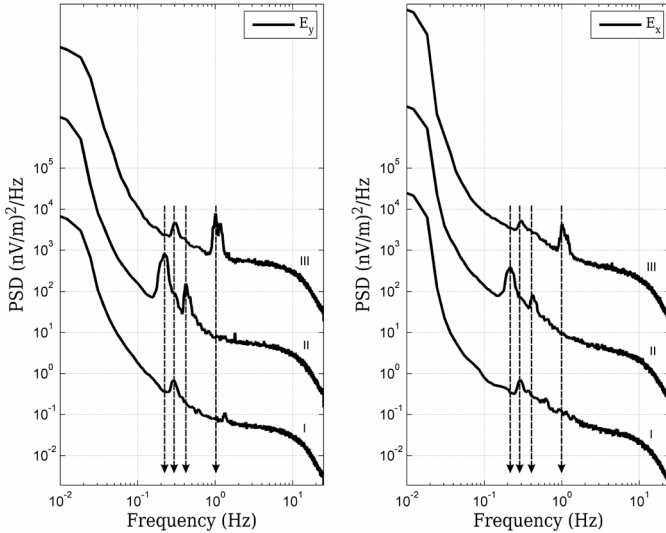
Figure 3.6: PSD's of the splited segments of a five hour times-series [Fig. 3.5]. Ex component (right) and Ey component (left). Three PSD's corresponding to the time segments (0-100 min), (100-200 min) and (200-300 min) are respectively denoted by I, II, and III. The I PSD lies in the bottom, II in the middle and III at the top. Each PSD is plotted 100 units apart for clarity. The scale is appropriate for the lowermost PSD.

The spectral peak at 0.2 and 0.4 Hz is evident in the II spectra while 1 Hz is visible in the III spectra. The different peaks in different time spectra might indicate the possibility of two different sources. In the Section-3.5.2, we surmised a mud-volcano for the spectral peaks at 0.2 Hz & 0.4 Hz, which due to degassing may create these peaks (De Lauro *et al.* 2006). The strong power of these peaks in E_y component suggests a directional nature of the source. Generally, a degassing may circulate an isotropic velocity field in the vicinity of the volcano. The velocity field radially away from the volcano would be directional and can influence the electric fields components (Fig. 3.7). In actuality, our acquisition region lies far from the known mud-volcano and therefore it can influence PSD components. The situation intuitively will support the state of $V_x > V_y$. Eventually, it fits with the spectral peak observations i.e. peak in E_y PSD > E_x PSD.

The peak at 1 Hz could be a microseisms contribution. Evidently, the spectral peak holds strong power in the y-component (i.e. PSD peak: $E_y > E_x$). The directional characteristic (elucidated in Section-3.5.2) of a microseism contradicts the above observation (see last paragraph of Sub-section-3.5.3). The spectral peak at 1 Hz therefore, is possibly
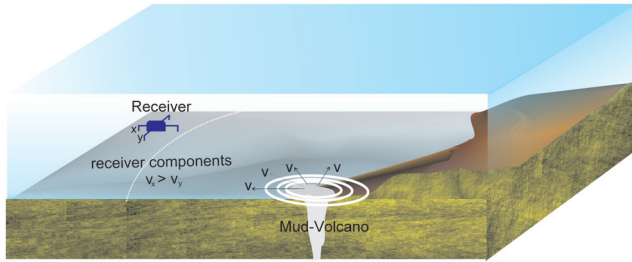
Figure 3.7: Idealistic diagram showing the velocity field radially away from the mud-volcano. The components of the receiver will experience different velocity and thus reading by the electric field components will be different.

not a contribution by a microseism. Moreover, its possibility as a contribution by a gravity wave is unlikely too as

1. 1 Hz is a temporary peak while a gravity wave may lead to a time ambient peak.

2. 1 Hz can not travel a depth of 500 m from the sea surface, due to skin depth limitation.

The high frequency (1 Hz) of the peak suggests for a source near the ocean-floor. It is difficult, at moment, to even presume a source for this spectral peak.

The discussion allows us now to discriminate the spectral peaks by their most likely sources. The updated discussed information is shown in Table-3.3.

Table 3.3: **Update-1: Spectral Range and Possible Sources**

Lower	**Intermediate**	**Sub-high**	**High**
0.01 - 0.1 Hz	0.1 - 2 Hz	2 - 10 Hz	10 - 25 Hz
External Field	Mud Volcano (0.2 & 0.4 Hz)	Complex seismic background noise	Digitization noise
Eddies	Gravity waves (0.3 Hz)		
Infra-gravity Waves	Unknown Source (1 Hz)		

3.7   Spectrogram

As it was shown in Fig. 3.6, the spectral content of the time series varies with time, which may be useful to gain information on the source. In order to gain more resolution in time we carry out a spectrogram analysis. A spectrogram is the discrete-time Fourier transform of a sequence, computed using a sliding window. For a spectrogram calculation, the time series is divided in to segments equal to the length of the Hanning window (Shin & Hammond 2008). Each segment overlaps 50 percent of the samples with the adjacent segment. PSD is calculated for a defined time length. The process is repeated again and again by sliding the window to build a spectrogram. The Spectrogram corresponding to the time series (Fig. 3.2) is shown in Fig. 3.8.
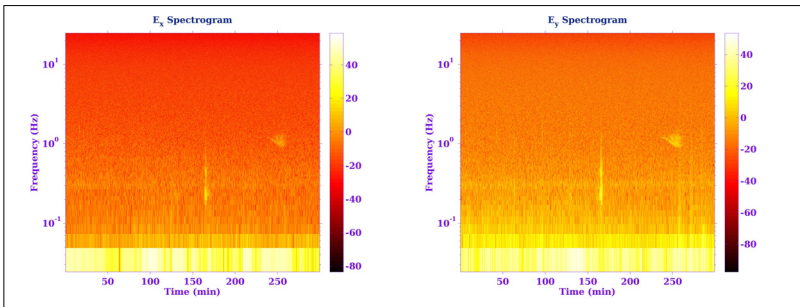
Figure 3.8: Spectrogram for E_x (left) and E_y (right). Electric field power is color coded in dB and is displayed as function of time and frequency.

Evidently, two temporary features are evident. The first correspond to time 250 min. and frequency 1 Hz. For weak reasons, we have already rejected microseisms form the probable source list for 1 Hz peak. It is still hard to place any other oceanic source for the current feature. The second feature can be noticed at approx. time 160 min. This feature correspond to the spectral peaks of 0.2 Hz and 0.4 Hz observed in the PSD. A gain by a spectrogram can be noticed at this juncture. Here, the spectrogram identifies a broad spectral range of the feature present from 1 to 0.1 Hz, rather than a peak at 0.2 Hz and 0.4 Hz,. This observation is not causing any change in its plausibility as a contribution by a mud volcano.

Corresponding to 0.3 Hz, a constant feature is apparent which runs through out the time. The time ambient feature can be presumed to be contributed by a gravity waves.

3.8   Modeling of a Gravity Wave

The electromagnetic contribution by a gravity wave can be addressed via the TE mode theory (Section 2.6). Theory demands knowledge of the wave velocity for the field amplitude calculation. A wave height estimate can determine the velocity (see Eq. 2.169).
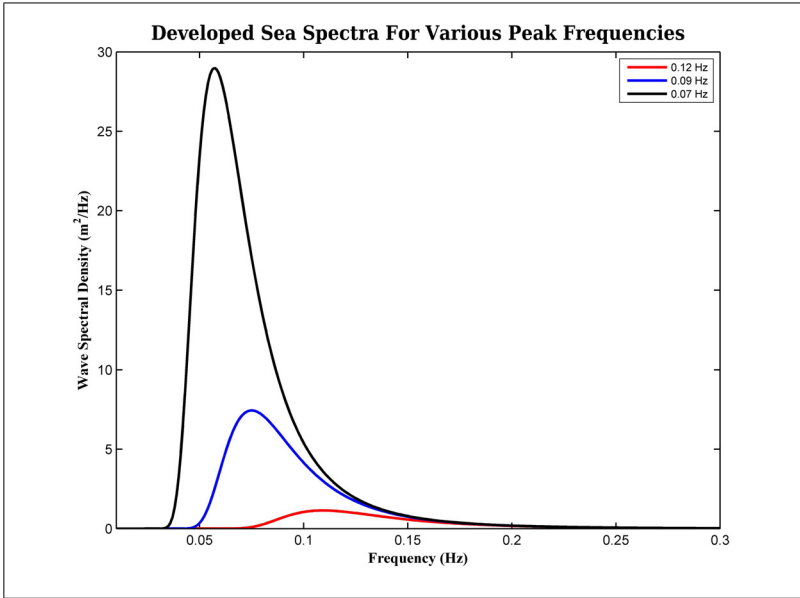
Figure 3.9: Pierson and Moskowitz spectra for fully developed sea (a sea produced by winds blowing steadily over a long duration of time). Legend marks the peak frequencies for which various spectra's are calculated.

We used the Pierson-Moskowitz wind wave spectra (Phillips 1977; Chave & Cox 1982) to estimate a spectral wave height. The spectrum reads

$$w(f) = \frac{2\pi\alpha g^2}{\omega^5} e^{-0.74(\frac{f_m}{f})^4} \tag{3.21}$$

spectral wave amplitude in m^2/Hz. Here, g is acceleration due to gravity, $\alpha = 0.001$ a dimensionless constant, f is frequency, f_m is peak frequency and $\omega = 2\pi f$ is angular frequency. The wave spectra of a fully developed sea at different peak frequencies are shown in Fig. 3.9. The comparison of the true PSD (III spectra in Fig. 3.6) and a gravity wave generated PSD is shown in the Fig. 3.10. Please note that we are not able to provide the simulation results for actual observation depth of 500 m, as peak velocity at the depth is of order of 10^{-35} m/s. We are therefore showing a simulation results at much shallower depth. We obtain a good simulation for the 0.3 Hz peak by a gravity wave having a peak oscillation period (frequency) of 1/0.53 s (i.e. 0.53 Hz) at the 20 m depth. The depth 20 m is too shallow compared with original observation depth (500 m). Therefore we can discard the presumption of 0.3 Hz peak by the gravity wave. The skin depth calculation allows an existence of 0.3 Hz at ocean-bottom but

modeling contradicts it. The answer lies in the Section-2.5.3, which explains that a wave not only experiences an electromagnetic damping (which is a basis of the skin depth calculation), but also a geometrical damping. Geometrical damping dominates more than electromagnetic damping for smaller wavelengths. This prevents 0.3 Hz from reaching the ocean-floor. Based on the discussion in Section-2.5.3, which supports the observation too, we propose a formula for the penetration depth (skin depth is valid for zero wave-number case) as

$$\delta \approx \frac{0.0616}{f^4} \quad \text{for } f \text{ in Hz and } \delta \text{ in meters} \tag{3.22}$$

The relation (Eq. 3.22) is a significant relation to estimate the penetration depth of a motionally contributed electromagnetic field. An electromagnetic contribution is directly related to the oceanic oscillations and therefore this relation might be valid as well for penetration depth calculation of oceanic waves. Joint look of Eq. 3.21 and Eq. **??** indicates a plausibility but still it demands an establishment by oceanographic observations.
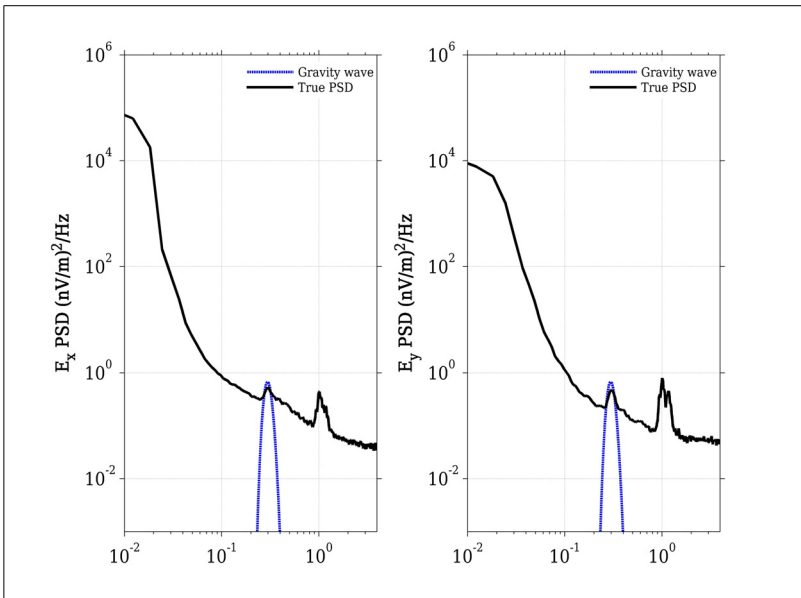

Figure 3.10: Comparison of a measured PSD (measured at 500 m depth, black solid line) and a calculated PSD of a gravity wave measured at 20 m depth. (blue dashed line).

In an electromagnetic field observation at an approximate depth of 3.5 km, Cox *et al.* (1978) observed a spectral peak at 0.2 Hz. They proposed a mechanism to explain the peak. Unlike microseisms, which requires interaction of two opposite wave trains of the

same wavelength, they proposed if two wave trains are not exactly opposed or do not have exactly the same wavelength, the standing waves will have phases varying slowly over the sea surface. Consequently at deeper depth, they will create a horizontal pressure gradient and therefore horizontal water current, which will induce EM field. This mechanism may plausibly also explain observed spectral peak at 0.3 Hz.

3.9   Analysis of Lower Spectral Band

We try to explain the lower spectral band by

a) Naturally contributed signals (natural field) created by the ionospheric and magnetospheric current system, normally used as signal for MT (Vozoff 1991), and

b) Motionally contributed signals (motional field) created by the oceanic movement in the geomagnetic field (Young *et al.* 1920).
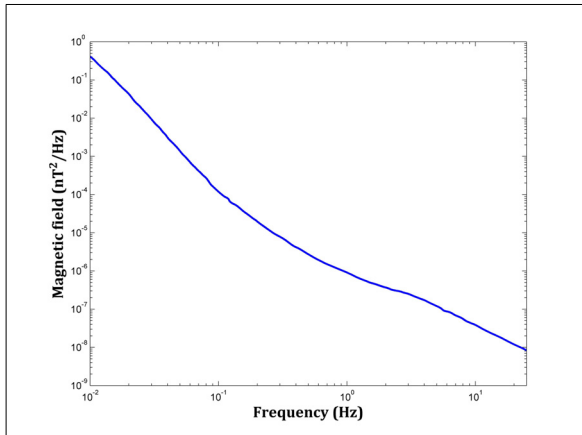
Figure 3.11: The PSD derived from the average PSD (Vozoff 1991) measured on land. The PSD is used to generate the PSD at the ocean floor.

The natural contribution is analyzed by using a spectrum derived from the average power spectrum measured on land (Vozoff 1991). We assume that over a day the spectrum is approximately same everywhere and want to explain only roughly the shape. We use downward continuation (using the electromagnetic damping theory) of the natural field PSD measured at surface, shown in Fig. 3.11, to obtain the PSD at the ocean floor, which is shown in Fig. 3.12-a (black line). Note that the usage of present land spectra is crude as it belongs to another locality. An electromagnetic field measurement in the vicinity of data acquisition area would be a more reliable in this context.
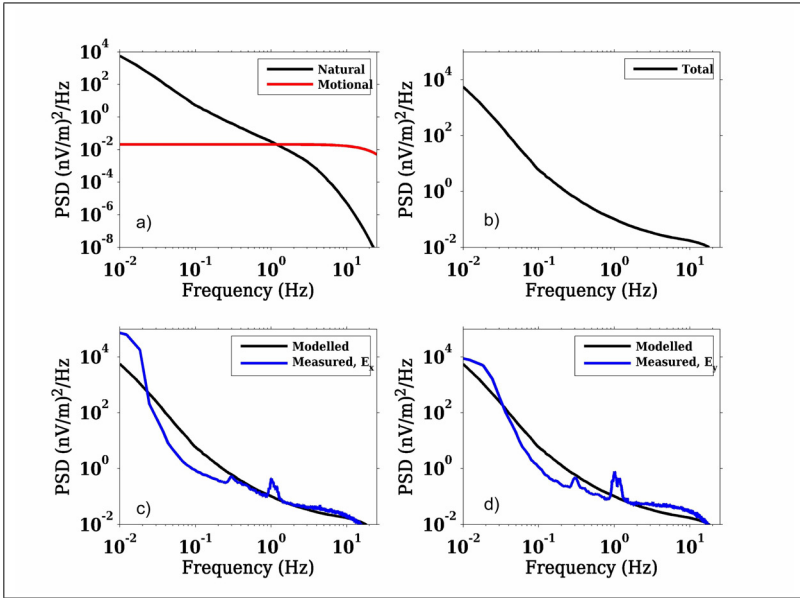
Figure 3.12: PSD contribution by external and internal sources measured at 500 m depth in the ocean. a) the black line represents the power contributed by ionospheric and magnetospheric current system (natural field). The red line represents the power contribution by an oceanic movement (motional). b) Total PSD representing the combined influence of natural and motional field. c) Comparison of the total PSD with the measured E_x component's PSD (IIIrd PSD in Fig. 3.6 (right)). d) Comparison of the total PSD with the measured E_y component's PSD (IIIrd PSD in Fig. 3.6(left)).

The natural field alone does not explain the the background energy between 0.1 and 10 Hz. Therefore, we check that whether this can be explained by the motional field together with natural field. We made an estimate for the motional field based on the TM mode theory (Section 2.5) and find that small and moderate horizontal velocities are sufficient to explain the measured spectra.

An eddy is a rotation element of moving fluid which occur when water current doubles back on itself, moves against the direction of main flow or experiences large shear (Nichols & Williams 2008). They lead to a circular flow of water along the edge of the main current. The horizontal eddy diffusivity is 10^5 - 10^8 times larger than vertical eddy diffusivity (Stewart 2007). This suggests an eddy contains much strong horizontal velocity than the vertical one. The TM mode theory assumes a horizontal movement and therefore keeping this in mind, we used TM mode theory to analyze the contributions. It might be possible that the effect by the eddies would be different than that of the TM mode. A five layer oceanic model is used for computations. The conductivity of the ocean

is kept constant (3.33 S/m). The thickness of each layer is maintained 100 m, which defines a 500 m deep ocean. Each layer has a different velocity. The used velocity model and other parameters are shown in Table-3.4. The obtained motional-PSD is shown in Fig. 3.12-a (red line). We used a constant wavelength (175 m) to simulate the response. In general, frequency, velocity and wavelength are coupled with each other. Usage of constant wavelength therefore makes modeling very crude. Nevertheless, it will generate a suitable response in lower frequency range, where effect of wavelength and velocity are very small and frequency principally plays a dominant role in deciding the field strength (see Section-2.5.3).

Table 3.4: **Parameters used for the TM mode simulation**

Oceanic layers	Velocity (m/s)	Other Parameters:-
Layer 1.	0.1	Ocean conductivity: 3.33 S/m,
Layer 2.	0.01	Thickness of each layer: 100 m,
Layer 3.	1×10^{-4}	Total ocean depth: 500 m,
Layer 4.	1×10^{-5}	Wavelength: 175 m (constant),
Layer 5.	4×10^{-7}	Ambient Geomagnetic field: 3×10^{-5} T

By combining natural-PSD and motional-PSD, we obtained a total-PSD shown in Fig. 3.12-b. The comparison of the total-PSD with the measured E_x and E_y PSD's are shown in Fig. 3.12-c & d, respectively. Evidently, we are not able to provide exact match, but still the modeled PSD in general satisfies the observed PSD. The peak power at 0.01 Hz, offers a reasonable match with the E_y PSD but a clear unmatch with the E_x PSD. We presumed an infra-gravity wave as cause of the effect.

In order to simulate high power by infra-gravity wave (Kinsman 2002; Leont'yev 2009) in vicinity of 0.01 Hz, we used TE mode theory (Section 2.6). In a 500 m deep ocean, an infra-gravity wave of height 1.2 cm approximates the power peak of E_x component, as shown in Fig. 3.13. The modeling parameters are shown in the Table-3.5. A choice of frequency dependent wave height will improve the match which one can understand and therefore we are leaving it.

Above we observed a PSD match by different presumed sources of external and internal origin (Section-3.5.1). The modeling study suggests a dominant role of the ionospheric currents (natural field), potentially horizontal velocity background noise possibly related to eddies and infra-gravity waves to influence the lower spectral band. Evidently, the combined PSD of natural field and horizontal velocity background noise related to eddies satisfies a general power level measured at the ocean floor. They show a reasonable

Table 3.5: **Parameters to simulate an infra-gravity wave**

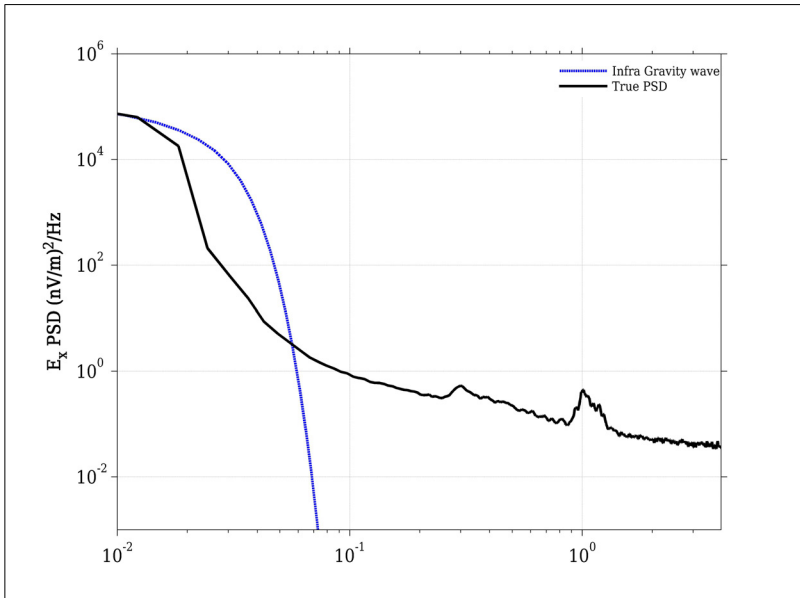| Parameters	Value
Ocean conductivity	3.33 S/m
Ocean depth	500 m
Wave height	1.2 cm
Ambient Geomagnetic field	3×10^{-5} T

Figure 3.13: Simulation result for an infra-gravity wave. At a depth of 500 m the observed PSD is shown by a black solid line. The dotted blue lined represents a simulated PSD

match with the E_x component. However, the E_y PSD in lower spectral range can not be explained by natural field and therefore is simulated with the infra-gravity wave. Normally, the Pearson-Moskowitz spectra generated wave height is used to model a gravity wave. But as the spectral wave height of a fully developed sea is wind velocity dependent. A peak wave height at 0.01 Hz (using the Pearson-Moskowitz spectra) requires a wind speed of 130 m/s at a height of 19.5 m above the sea surface [as $f_m = \{g/(2 \times pi \times v_{19.5})\}$ where

$v_{19.5}$ wind speed at a height of 19.5 m above the sea surface (Phillips 1977)]. The obtained wind speed is not practical and therefore for the power simulation of the E_y PSD at 0.01 Hz, we choose a infragravity wave of a fixed wave-height (1.2 cm). Note, here the frequencies and the wavelengths are coupled together with a dispersion relation (Eq. 2.162).

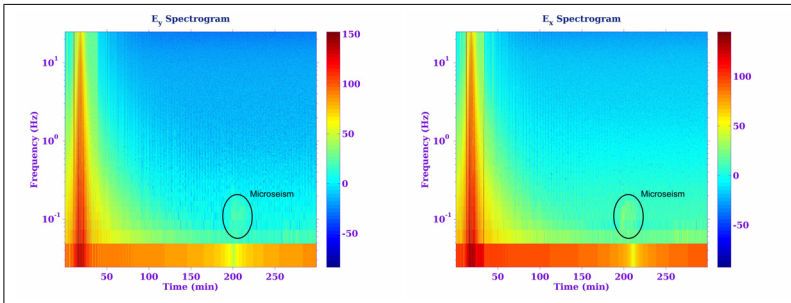## 3.10   Microseisms during mCSEM data recording

Figure 3.14: Presence of microseisms during mCSEM data recording. The left and right panel respectively represents the E_y spectrogram and E_x spectrogram. The electric field power is color coded in dB and displayed as function of time and frequency. Corresponding to frequency 0.1 Hz and time 200 min (approx), a yellow colored high power patch is evident, which may be contributed by microseisms. The other high power patches in the spectrogram is by the transmitter current

Microseisms are generated at the ocean-floor by a non-linear interaction of waves (under some special conditions) at the sea-surface. Despite the source at the surface, microseisms create significant oscillations at the ocean floor which may generate powerful electromagnetic signals. It is worth mentioning that the mCSEM recordings are made at the ocean floor therefore, presence of microseisms might induce a significant noise in mCSEM signal.

The possible significance of microseisms for the mCSEM studies can be visualized from the spectrogram shown in Fig. 3.14. A time segment, where the transmitter was active (transmitting the signals), is used to generate the current spectrogram. Close to 25 minute, strongest powers (red in color) are evident that cover a broad spectral range. At this time, the transmitter was close to the receiver. Further, with increase in time a systematic decay in the power can be noticed. This is because as the transmitter departs away from the receiver. Approximately at 200 min. a yellow colored high power (black ellipse) patch can be noticed corresponding to 0.1 Hz frequency. This plausibly is a contribution by microseisms. Quantitatively, a peak power by the transmitter is approx. 150 dB while

the microseisms contributes approx. 40 dB. Clearly, at a larger T-R separation, the power contribution of microseisms would be enough to contaminate a mCSEM signal.

To understand the details of microseisms, we confined the spectrogram to a time zone involving microseisms. The obtained spectrogram of 90 min. duration is shown in Fig. 3.15 (top). Evidently, microseisms can be noticed up to approx. 20 min. duration. The spectral range is in between 0.07 - 0.2 Hz. The peak frequency is 0.1 Hz. It would be difficult to judge from the spectrogram that component holds higher power. The corresponding PSD is shown in Fig. 3.15 (bottom).

3.11   Discussion and Results

We have analyzed four spectral ranges based on the slope changes (Fig. 3.3). We presume sub-high (2 - 10) range and high (10 - 25) range as noise. The sub-high range is possibly a contribution by the seismic background signals of complex nature, which is more or less like a random noise. The slope of PSD is flat, which also corresponds for a random noise. The high spectral range PSD slope offers a f^{-3} dependence. Although the slope indicates for an active source but at the ocean floor background oscillation between 10 to 25 Hz is not physical and therefore we presume it as a digitization noise. The ionospheric and magnetospheric current system created external field can supply significant signals in spectral range less than 0.3 Hz, as skin depth at the frequency is similar to the data acquisition depth (for σ = 3.33 S/m). The external field therefore can influence mainly two spectral ranges that is lower (0.01 - 0.1 Hz) range and intermediate (0.1 - 2 Hz) range. The motional field created by the oceanic movements will also significantly influence the same spectral range and therefore is of particular interest.

We list three possible sources which can influence the lower spectral range. These sources are external field, potentially horizontal background noise possibly related to eddies and infra-gravity waves. Integral contribution by first two fields satisfies a general power level of the PSD as shown in Fig. 3.12. The presented modeling is although crude but a good agreement between the power levels of the observed PSD and predictions is encouraging. A modeling with spectrum generated from the similar time data acquired in close vicinity of marine acquisition area might offer a more reliable result. The modeling result show a good match close to 0.01 Hz for the E_y PSD than the E_x component. We presume high power at 0.01 Hz as an influence of the infra-gravity wave and the conjecture is encouraged by the modeling results (Fig. 3.13).

In the intermediate spectral range, three spectral peaks in PSD and spectrogram at 0.3 Hz, 0.2 & 0.4 Hz and 1 Hz suggests for three possible sources. Spectrograms helps in finding the time based characteristics of these sources, suggesting the last two peaks and the first peak as a contribution by the temporary sources and a time ambient source, respectively. A gravity wave is a time ambient source and therefore we first presumed it for 0.3 Hz. modeling for the 0.3 Hz by the gravity wave was failed for 500 m depth and we observed a match for 20 m depth. The observation suggested that gravity wave
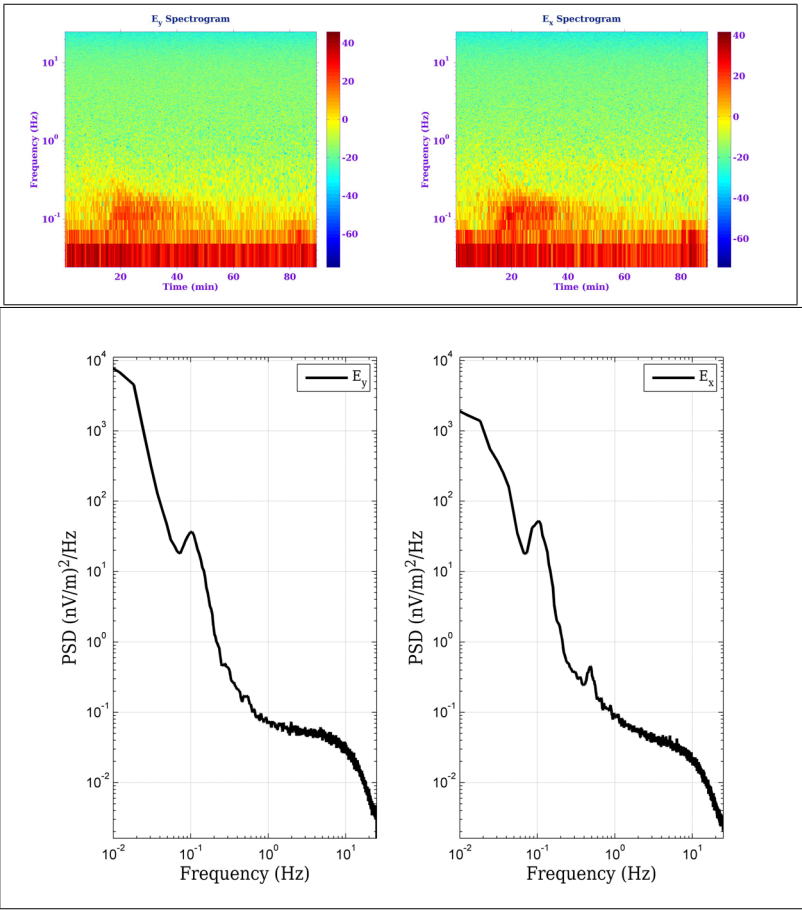
Figure 3.15: Presence of microseisms during mCSEM data recording. **Top**: Spectrogram representing the power in dB (color coded scale). The horizontal and vertical axis respectively represents time and frequency. E_y component (Left); E_x Component (Right). A feature localized at the spectral range between 0.07 to 0.2 Hz and time between 15 to 40 min (approx), representing a high power patch is microseisms. **Bottom**: PSD of the corresponding time segment. E_y component (Left); E_x Component (Right). The horizontal and vertical axis respectively represents frequency and PSD. Two peaks are evident, one at 0.5 Hz and other at 0.1 Hz.

of 0.3 Hz is significant at 20 m depth but can not penetrate to the ocean-floor (500 m). However, skin depth for 0.3 Hz is 500 m. The depth calculation by the modeling esti- mate and the skin depth relation are disagreeing. The reason is the geometrical damping, which is not included in skin depth relation. We present a formula (Eq. 3.22) for the case which accounts for both geometrical and electromagnetic damping, to estimate the penetration depth of a frequency. Later, we presumed other possible mechanism for 0.3 Hz creation and is the non-linear interaction of the two opposite wave trains of slightly different wavelength. Due to the interaction they from standing waves such that they have phases varying slowly over the ocean surface. The process will create a horizontal pres- sure gradient which might induce the field in the ocean. The 1 Hz peak is possibly not a micoseisms contribution. We are leaving it unexplained but will back with an elucidation in the next chapter. The last peak 0.2 & 0.4 Hz is again not contributed by a microseism and we presume a mud-volcano as a responsible source.

We observed a microseism during the recording. The strength is significant and there- fore negligence of microseisms in the mCSEM modeling estimate might lead to an erro- neous result.

4 Spectral Directionalogram

4.1 Introduction

We use the direction of the electric field to draw conclusions on the nature of the source. We have developed a new approach named "spectral-directionalogram (SD-gram)", which maps the direction of the vector field lines of the registered frequencies with respect to time.

The chapter is intended to discuss the theory and usefulness of the SD-gram technique. We have done simulations with the synthetic data generated by various superpositions of different signals to check the limitations and advantages of the SD-gram. Finally, the SD-gram is applied on the mCSEM data set and we show that consideration of both amplitude and direction is useful to identify possible sources of noise.

4.2 Spectral-Directionalogram

The spectral-directionalogram (SD-gram) is an artificial term, denoting collective plot of the time, frequency and direction, which represents time varying directions of frequency contents of a vector field.

4.3 Theory and Methodology

Consider a vector field $\vec{E}$, which is a function of frequencies f i.e.

$$\vec{E} = \vec{E}(f_i), \quad i = 1, 2, 3, ..., N-1, N \tag{4.1}$$

The subscript 'i' denotes number of frequencies. For a two dimensional Cartesian coordinate system, let E_x and E_y represent the x and y component of $\vec{E}(f_i)$. The adopted convention suggests that the angles will be measured in the clockwise direction. The components of $\vec{E}$ can be expressed as:

$$\vec{E} = \hat{x}E_x + \hat{y}E_y \tag{4.2}$$

We now determine the direction θ of $\vec{E}(f)$ by projecting vector $\vec{E}(f)$ successively onto directions defined by testing angles ($0 < \theta < 180$) via:

$$E = E_x \cos(\theta) + E_y \sin(\theta) \tag{4.3}$$

The length of the projection E will adopt a maximum if the vector was projected onto its own direction, and thus the θ which fulfills the condition

$$\left| E_x \cos(\theta) + E_y \sin(\theta) \right| = \text{maximum} \tag{4.4}$$

is the direction of $\vec{E}(f)$ with respect to the x-axis. Eq. 4.4 will facilitate the determination of the azimuthal angle of field lines.

The Windowed Fourier Transform (WFT) technique (Griffin 1984) together with the maximization condition (Eq. 4.4) is utilized to produce the SD-gram. In the Fourier transform framework, time localization can be achieved by windowing the data at various times using a Hanning window (Bendat & Piersol 1986) function W(t) and then taking Fourier Transform. The WFT is given by

$$X(\omega, \tau) \quad = \quad \int_{-\infty}^{-\infty} x(t)W(t - \tau)e^{-i\omega t}dt \tag{4.5}$$

$$= \quad \int_{-\infty}^{-\infty} x(t)W_{\omega,\tau}(t)dt \tag{4.6}$$

where, $x(t)$ represents a time-series data for time t; $\omega = 2\pi f$ represents the angular frequency; $W_{\omega,\tau}(t) = W(t - \tau)e^{-i\omega t}$ is integration kernel. The transform $X(\omega, \tau)$ measures locally, around a point τ, the amplitude of the frequency ω. The vector field in Eq. 4.1 is $\vec{E}$ and the component in Eq. 4.5 is E_x and E_y.

The SD-gram as utilises the WFT, which has a fixed resolution depending on the width of the window function W. The width therefore in Eq. 4.5 decides the time and frequency resolution of the SD-gram. A wide window gives better frequency resolution but poor time resolution. A narrower window gives good time resolution but poor frequency resolution. Use of wavelet transform, which is our outlook, may help in improving the resolution as they gives good time resolution for high-frequency events and good frequency resolution for low-frequency events.

4.4 Simulation with synthetic data

We assume an oscillating signal from an azimuth and try to determine the direction of field lines close to the receiver (which excludes the circularly polarized waves there). We have done experiments to test it for various superpositions of different signals. The direction of the source might be determined from the direction of field lines if further assumptions on the source mechanism are made.

We present four different experiments to evaluate the efficacy of the SD-gram. For

each experiment, using frequency, time and direction (azimuth) as parameters two components of a time-series are generated. For that, we first assumed a fixed receiver (sensor) with the x- and y-components. Secondly, we assumed arrival of the oscillating field lines to the receiver space. The possible cases and their details are presented in the various sub-sections.

4.4.1   Single Frequency and Single Azimuth

For the experiment, the components of a test time-series signal are generated using the following steps.

1. We first generated a single frequency ($f = 0.5$ Hz) time-series (T) of time length t i.e. $T = \sin(\omega t) + \cos(\omega t)$, where $\omega = 2\pi f$, which is shown in the top panel of Fig. 4.1.

2. The time-series (T) is now divided in to two horizontal components by assuming that the oscillating field lines hold an azimuth (θ) of 110° with respect to components of the receivers. Therefore, the components are $X = T\cos(\theta)$ and $Y = T\sin(\theta)$. The obtained components are shown in the middle panel of Fig. 4.1.

3. In order to bring the test signal close to noisy scenario, contamination of both x- and y-components are done by adding a white Gaussian noise (such that the signal to noise ratio is always unit (i.e. $S/N = 1$)). The contaminated components are shown in the bottom panel of Fig. 4.1.

For the clarity reasons each panels is plotted for time length of only 12 sec., although we assumed bigger time length for the SD-gram.

The test data is now utilised to generate the SD-gram. The obtained output is shown in Fig. 4.2. The given model parameters was $f = 0.5$ Hz and $\theta = 110°$. Evidently, corresponding to 0.5 Hz, an azimuth of 100° is apparent in the SD-gram. The good agreement between the modeling parameters and obtained SD-gram result therefore shows a resolving potential of the method, for this case. Although the signal to noise ratio of the utilised test time-series was small (S/N=1), the azimuth resolvability of the SD-gram is reasonable.

4.4.2   Multi-frequency and Single Azimuth

Following the same steps as described above, two components of multi-frequency time-series are generated encompassing frequencies of 0.5 Hz, 1 Hz and 3 Hz. We assumed an azimuth of $\theta = 110°$ for the oscillating field lines. Along with the modeling parameters, the obtained SD-gram of the test signal is shown in Fig. 4.3. A permanent azimuth of 110° is evident corresponding to 0.5 Hz, 1 Hz and 3 Hz. In the previous case, we observed that the SD-gram is capable of resolving the azimuth of a frequency. The observation further adds that the SD-gram can resolve the azimuth of the different oscillations of an identical azimuthal construction.
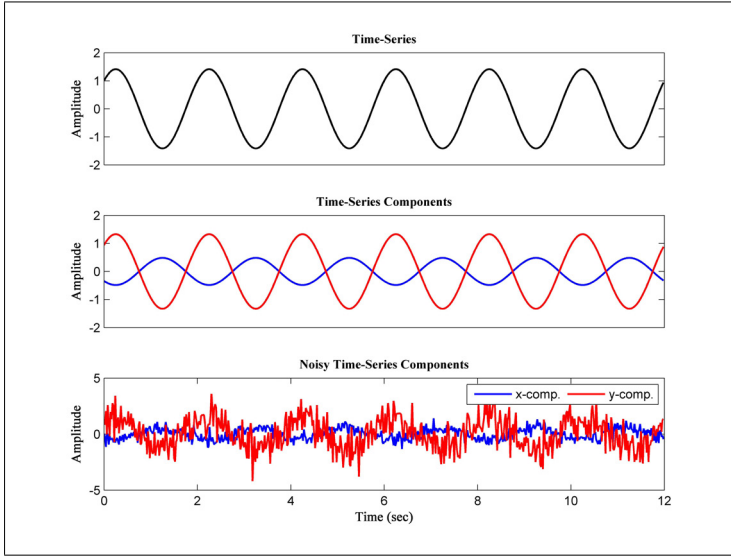
Figure 4.1: **Top Panel:** The test time-series signal of 0.5 Hz. **Middle Panel:** The x- and y-components of the top-panel signal assuming an azimuth of 110°. **Bottom Panel:** Noise added middle panel time-series. The x- and y-components are represented by the blue and the red line, respectively. Note the time scale of the top two panels plot (not shown) is identical bottom panel plot.

4.4.3 Identical multi-frequencies in different time and Three Azimuths

The SD-gram can not resolve the two azimuths of the identical frequencies at an identical time. This is because we can find only one maximum of Eq. 4.4. But from the time-series, we may resolve different angles of frequencies provided field lines hold only one angles at a time. Experiment is done to check the case with a time-series which contains three azimuths in three different segments of time. The test time-series components are generated by using the steps, which are as follows:

1. Three time-series T_1, T_2 and T_3 of identical length and frequency content are generated.

2. The time-series T_1 is multiplied with the cosine of azimuth-one ($\theta_1 = 30°$) i.e. $T_1 \cos(\theta_1)$. Similarly, cosine of the azimuth-two ($\theta_2 = 100°$) and azimuth-three ($\theta_3 = 170°$) are respectively multiplied with the T_2 and T_3 time-series.

3. Addition of these three outputs give the X-component of the time series i.e. $X = T_1 \cos(\theta_1) + T_2 \cos(\theta_2) + T_3 \cos(\theta_3)$.
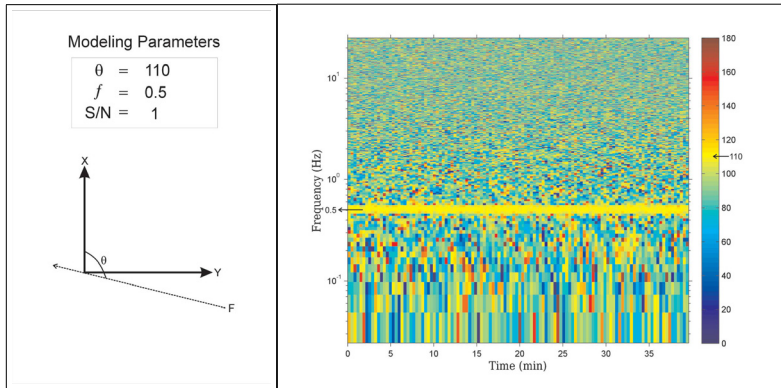
Figure 4.2: The modeling parameters (left) and SD-gram of the test signal (right). **Left:** X and Y represent the two horizontal axis (solid bold lines) of a receiver, θ represents an azimuth (with respect to the X-axis) of the oscillating field lines F (dotted arrow) of frequency f. **Right:** Corresponding to 0.5 Hz an azimuth of 110° (yellow color) is evident. A vertical color bar placed right of the SD-gram represents the azimuth, from (0° to 180°).
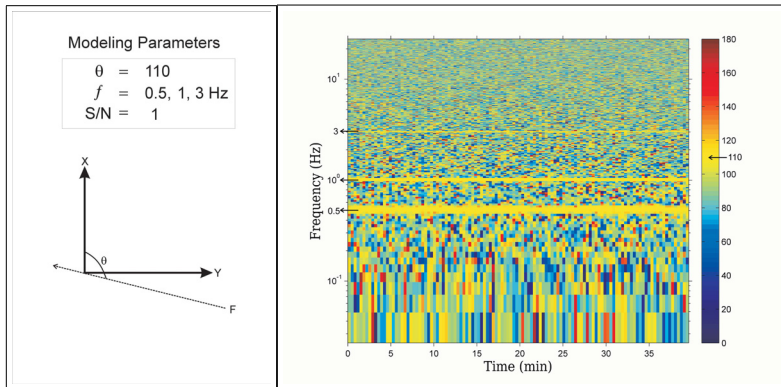

Figure 4.3: Figure showing the modeling parameters (left) and SD-gram of the test signal (right). **Left:** The field lines F are oscillating with multiple frequencies of 0.5 Hz, 1 Hz and 3 Hz. They construct an azimuth of $\theta = 110°$ with the X-axis of the receiver. **Right:** The SD-gram shows an azimuth of 110° corresponding to 0.5 Hz, 1 Hz and 3 Hz. The color bar has yellow color for 110°.

4. Similar steps are followed to obtain the Y component of time-series, we only re-placed the cosine function by the sine function i.e. $Y = T_1 \sin(\theta_1) + T_2 \sin(\theta_2) + T_3 \sin(\theta_3)$.

5. Noise is added to the components such that $S/N = 1$.

Note that the three azimuths are not assigned to the entire time length. The azimuth-one ($\theta_1 = 30°$) to $1/3$ of time length, azimuth-two ($\theta_1 = 100°$) to $1/3$ to $1/4$ of time length and azimuth-three ($\theta_1 = 170°$) is assigned to rest of the time length. The time-series is superposition of the frequencies 0.5 Hz, 1 Hz and 3 Hz.
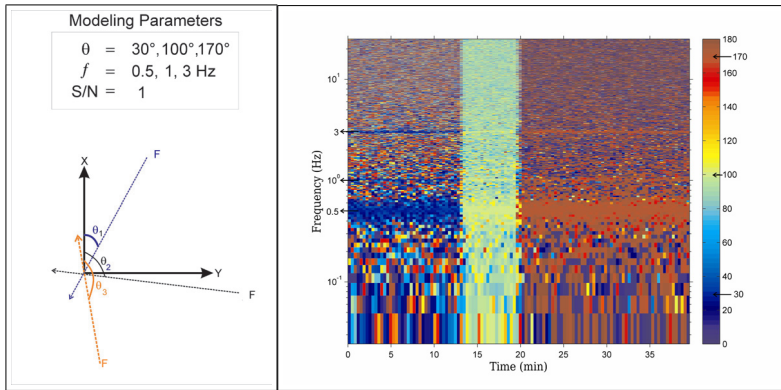
Figure 4.4: **Left:** Schematic representation of different constructions of field line with two components of a receiver. **Right:** the SD-gram of the test signal (right). Three azimuths are evident corresponding to three frequencies in three different times. The time interval between 0 to 13 min., an azimuth is 30°; between 13 to 20 min., an azimuth is 100° and between 20 to 100 min., an azimuth is 170°.

The obtained SD-gram is shown in Fig. 4.4. Corresponding to 0.5 Hz, three different azimuths are evident in time. From 0 to 13 min., 13 to 20 min. and 20 to 40 min. respective azimuths of 30°, 100° and 170° are evident. Similar azimuths are also apparent corresponding to 1 Hz and 3 Hz. The match between the consideration and observation certifies the resolvability of the case by the SD-gram. We have also done a similar experiment by taking different series of frequencies for an azimuth in different times and observed a successful result. Since it is obvious by the similarity in experimental considerations we are not presenting the SD-gram for this experiment. For the SD-gram generation, the adopted sampling frequency (f_s) is 50 Hz and number of FFT points (nFFT) is 2^{11} and therefore, the frequency bin width is 0.0244 Hz (as, bin-width = f_s/nFFT). It is apparent that the 0.5 Hz has a broad peak, compared to the 1 Hz and 3 Hz. In the lower frequency range, the bin-width will be wider on a log-scale plot and therefore, the occurrence of the broad peak is due to the log scale plotting. Moreover, neighboring frequencies (of 0.5

Hz) has tendency to show the similar or adjacent azimuths, which sometimes also help in broadening the peak. The changes in background directions during the times 0 to 13 min., 13 to 20 min. and 20 to 40 min, where the directions of the field lines are 30°, 100° and 170°, respectively is another striking observation. Closeness between the background and the field lines direction self explains the reason. The observation indicates that the a background direction depends on the potential direction of the field lines.

4.4.4 Dissimilar multi-frequencies in same time and Three azimuths

Two components of test time-series are generated by considering three azimuths and series of multi-frequencies. The first series of frequencies (f_1 = 0.5 Hz, 1 Hz and 3 Hz) hold an azimuth of 30°, the second series (f_1 = 0.7 Hz, 1.2 Hz and 4 Hz) holds 100° and third series (f_1 = 0.9 Hz, 1.4 Hz and 6 Hz) holds 170°. The obtained response of SD-gram is shown in the Fig. 4.5. Evidently, we observe consistent azimuths corresponding to frequencies 0.5 Hz, 0.7 Hz, 0.9 Hz, 1 Hz, 1.2 Hz, 1.4 Hz, 3 Hz, 4 Hz and 6 Hz. The respective azimuths corresponding to these frequencies are 30°, 100°, 170°, 30°, 100°, 170°, 30°, 100° and 170°. The observation agrees with the input parameters.
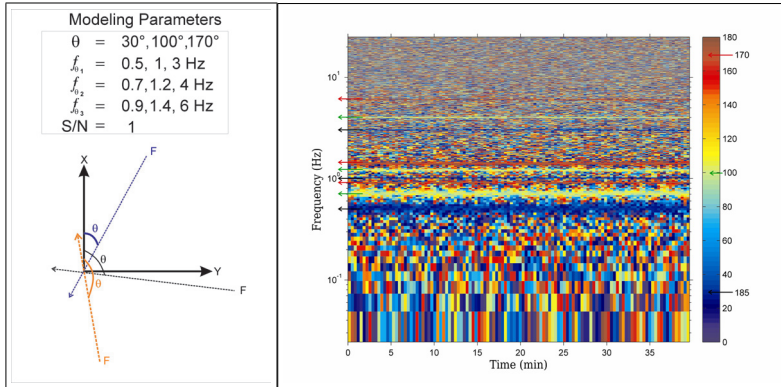

Figure 4.5: **Left:** Modeling parameters and schematic diagram showing the scenario of interaction of field lines F with two components of a receiver. **Right:** Twelve frequencies are evident in the SD-gram showing azimuths of 30°, 100° and 170°.

The modeling summery is presented in the table 4.1. Out of five experiments , in four experiments the SD-gram was able to resolve the azimuths of the oscillating field lines. The exception was the case when identical frequencies were holding different azimuths with a receiver. Therefore, the SD-gram is useful in resolving the azimuths of the oscillating field lines, provided identical frequencies are not holding different azimuths in the receiver space.

Table 4.1: **Modeling Summary:** Experiment for various situations and resolution of directions by the SD-gram.

Experiment	Azimuths	Frequencies	Direction Resolvability
I	One	One	Yes
II	One	Multi-frequencies	Yes
III	Three (at a time only one azimuth)	Multi-frequencies	Yes
IV	Three	Different Multi-frequencies	Yes

4.5   Results

The SD-gram has been applied to the mCSEM electric field data, which were already analyzed in the previous chapter. Responses from two receivers R1 and R2 are presented. Both the receivers are present in the same region and the recordings are made at the same time at the ocean floor, at a depth of 500 m from surface. The x-components of receivers R1 and R2 are deviated -8 and 25 from the North direction, respectively. The recording was supposed to done in the absence of transmitter current, but, as will be shown, might have been running during certain periods of time.
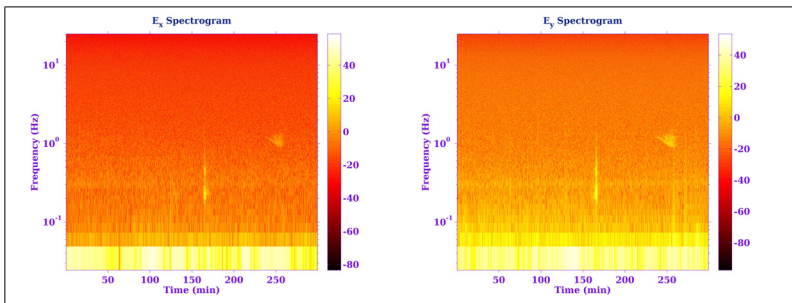

Figure 4.6: Spectrogram of the electric field (Ex and Ey) components of sensor R1. Two events can be seen approximately at 160 and 250 mins. The power is color coded in dB.

The spectrogram (not SD-gram) corresponding to the same time segment of receiver R1 and R2 are presented in Fig. 4.6 and Fig 4.7, respectively. Unlike the SD-gram where color represents the azimuth, here color represents the strength of the electric field. Note
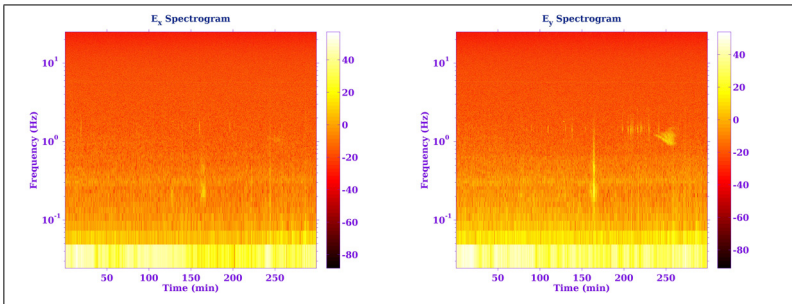
Figure 4.7: Spectrogram of the electric field components of sensor R2. Two events can be seen approximately at 160 and 250 mins. The power is color coded in dB.

that the Fig. 4.6 is repetition of the Fig. 3.8 and is shown here just for an ease. Evidently, in both the spectrograms two events can be easily identified. The first event is visible at time 250 minutes and frequency 1 Hz and the second event approx. at 160 min and to a broad frequency range varying from 0.08 to 1 Hz. Both the events look quite different from each other as their frequency contents and amplitudes are dissimilar. In the previous chapter, we were not able to interpret the first event. The second event was interpreted as a contribution by a volcanic source.
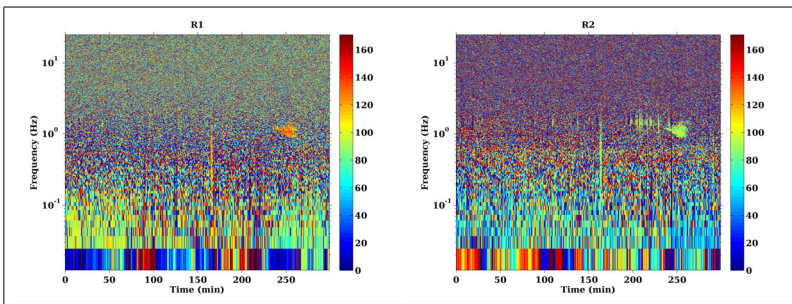

Figure 4.8: Spectral-directionalogram of receiver R1 (left) and R2 (right) in the absence of transmitter current. The electric field lines F of R1 receiver holds an azimuth of 125° for both events (250 min and 160 min). For the same events the azimuth in R2 receiver is 90°.

The SD-gram images of the receivers R1 and R2 are shown in Fig. 4.8. The horizontal axis and vertical axis represent time and frequency scale, respectively. The color bar represents the azimuth of the electric field, measured from the x-component in the clockwise direction. Evidently, the electric field lines of both the events (one at 160 min and other at 250 min) hold an azimuth of 125° for receiver R1 (Fig. 4.8, left panel)). For receiver R2 (Fig. 4.8, right panel) the field lines hold an azimuth of 90°.
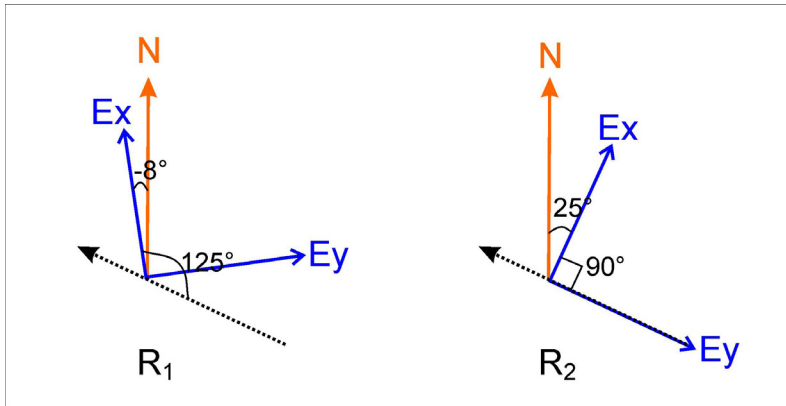
Figure 4.9: Position of the components of receivers Ex and Ey with respect to North (N) is shown by dark blue orthogonal lines. Receiver R1 is shown at the top and R2 at the bottom. The dotted black line denotes the direction of the electric field lines.

The directional information of receivers R1 and R2, including the correction of the angle between x-component and north direction for each receiver, are shown in Fig. 4.9. The orientation of the R1 and R2 receivers are displayed in the blue. Dotted black arrows represent the direction of the electric field lines. It is evident from the figure that the field lines (dotted black arrow) of both the receivers hold an identical azimuth (approx. 125°) with respect to north.
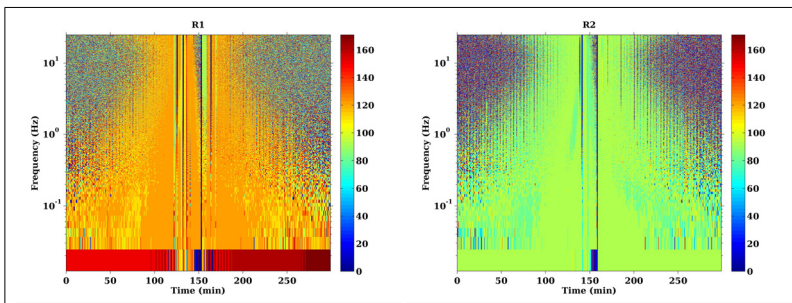

Figure 4.10: Spectral-directionalogram of receiver R1 (left) and R2 (right) in the presence of the transmitter current. The electric field lines of transmitter current in R1 receiver holds an azimuth of 125° while the R2 receiver hold and azimuth of 90°.

The Fig. 4.6 and Fig 4.7 use a time series segment when the transmitter current is supposed to be off. Fig. 4.10 shows the result when the transmitter current is on. The SD-gram is now dominated by the transmitter signal, i.e. there is a broad range of time and

frequency with a coherent direction. For R1, the dominant electric field azimuth is 125° and for R2 it is 90°. These are the same azimuths observed for the events in the signal free data (Fig. 4.8). This suggests that the two events might be caused by the transmitter, which might have been operating at certain times, possibly for testing purposes. This constitutes a new hypothesis in addition to volcanic source for event close to 160 min. with broad spectral range varying from 0.08 to 1 Hz. The 1 Hz event at 250 min. is most likely, as is evident, by the transmitter currents.

4.6   Conclusion

The spectral-directionalogram (SD-gram) seems a powerful tool to obtain directional information. The knowledge of the azimuth (direction) corresponding to frequencies together with the time is certainly a useful asset for an interpretation methodology. The example presented here demonstrates that the observed events at 160 min and 250 min. is likely a contribution by a common source as both the events hold an identical direction. Alone with the amplitude information, we could reach only to a result that the event at 160 min. is plausibly a contribution by a mud volcano. It is the directional information which is suggesting a most likely contribution by a transmitter current. The observation signifies that the characterization of a vector field is never complete with the amplitude information (like power spectral density, spectrogram, etc) only and sometimes they may deceive the interpretation. Directionality consideration is therefore necessary and useful asset for a reliable result.

The modeling experiments suggest that SD-gram is well applicable for the cases where the different frequencies hold different azimuths. Any change in azimuth of a frequency with progressing time is resolvable by the SD-gram. However, it fails to resolve the azimuths when different azimuthal field lines oscillate with the same frequency.

5 Analysis of marine Magnetotelluric data

5.1 The data

In this chapter, we analyze a marine Magnetotelluric (mMT) data set (Constable *et al.* 2009) to improve the quantitative understanding about the ambient electromagnetic noise, present in the ocean as a function of time and location. By analyzing the mCSEM data in the previous chapter, we have found a possible presence of transmitter signal during the times when it was supposed to be absent. Our prime aim is to understand the ambient natural electromagnetic signals rather than the artificial signals (like generated by transmitters).We here therefore use mMT data set, first because it guarantees for the absence of artificial signals and second we expect strong bathymetry, and local currents effect in the data.

The used data was collected in the Thirtymile Bank area, which lies in the vicinity of San Diego Trough (Constable *et al.* 2009). The sea-floor geology of the trough region presents an interest for offshore exploration industry which motivated and helped funding of the data acquisition.

Our analysis is confined to understand the electromagnetic noise scenario present in the ocean. Six stations are selected for the purpose, three of shallow depth ($\approx$ 300 m) and other three of greater depth ($\approx$ 600 m). The stations are identified by names: Currawong, Bunyip, Goanna, Shark, Lorrie and Corella. The shallow stations include, Currawong, Bunyip and Goanna. The deeper stations include Shark, Lorrie and Corella. All the six station data were acquired simultaneously starting from 9 April 2005. Time 19:00:00 UTC (12 PM local time) was the wake-up time of all the instruments. The detail about the equipment system can be found in article by Constable *et al.* (1998). Five channel recording was made with a sampling frequency of 31.25 Hz. The first two channels represent the B_x and B_y component of the magnetic field. The third and fourth channels corresponds to the E_x and E_y component of the electric field, and the fifth channel observes the pressure variations. The location details of the station are shown in Table-5.1. Fig. 5.1 is a Matlab generated bathymetry contour map showing the station locations.

Table 5.1: **Station Details:** Location (latitude and longitude) and depth of the six stations, divided in to two depths zones of shallow and deep nature.

Type	Instrument/Station	Lat. (deg.min)	Long. (deg.min)	Depth (m)
Shallow	Currawong (Cur)	32°46.936	117°50.176	300
	Bunyip (Bun)	32°51.726	117°51.205	325
	Goanna (Goa)	32°38.314	117°44.694	360
Deep	Shark (Sha)	32°41.72	117°52.87	651
	Lorrie (Lor)	32°45.275	117°58.147	675
	Corella (Cor)	32°37.36	117°49.62	700

5.2   Analysis of the shallow station data

The marine MT method (Constable 1990; Palshin 1996) records the MT (Webb & Cox 1972) data in the marine environment; recordings are made at the ocean floor. We studied these data sets by separating them into two depths i.e. shallow (300 m) and deep (600 m). The reason for the separation is the initial thought that the shallow depth stations will be more influence by the oceanic dynamics than the greater depth stations. Let us start the analysis with the three shallow stations namely Currawong, Bunyip and Goanna. The depth information of the respective stations are in the Table 5.1. The depth columns in the table indicate the distance from the sea surface.

5.2.1   Power Spectral Density

Due to lack of calibration information, we are not showing the time-series. We have frequency based calibration information and therefore we start with the PSD. The PSD is plotted using the initial six minutes of data. The purpose of the PSD plotting is to get information on the spectral energy distribution, which lead us to choose the frequency or frequency range of interest. The obtained electric and magnetic field spectra of the three shallow stations are shown in Fig. 5.2. A sharp rise in the spectral energy below 0.12 Hz is apparent in all the three stations. Above 0.12 Hz, the two spectral peaks are prominent, one at 1.2 Hz and other at 0.32 Hz. The vertical dotted lines are drawn corresponding to these peaks. The 1.2 Hz peak is evident only in the Goanna station and is apparent in both
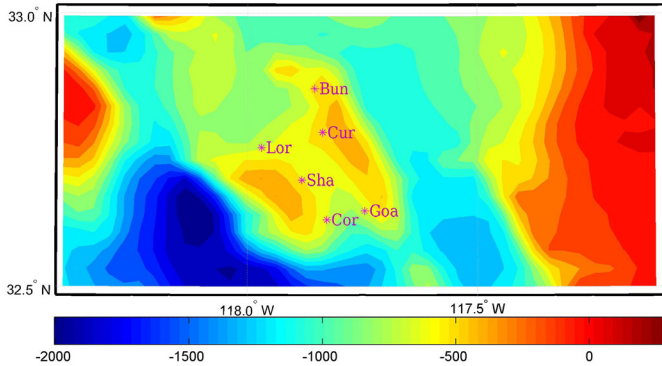
Figure 5.1: Depth contour map (approx. 115 m spacing) of the acquisition area. Magenta stars show the station locations and their short names. Color bar represents respective depth from the surface.

electric and magnetic field spectrum. The absence of the spectral peak in the other two stations suggests an influence by a local source. The other peak at 0.32 Hz is apparent in all the three stations. The presence can be noted in both the electric and the magnetic PSD. In Currawong and Bunyip, the presence is clear, while it is less clear in Goanna. The presence in every station indicates the possibility of a regional source in the formation. Spectrograms may help in providing the further details on the sources of 0.32 Hz and 1.2 Hz peak.

5.2.2   Spectrogram

Spectrograms, which preserve both time and frequency information are displayed to understand the time based spectral characteristics of the electromagnetic signals. We use 5 hour data of particular interest, to plot the spectrogram. The obtained electric and magnetic field spectrograms of the stations Currawong, Bunyip and Goanna are shown in Fig. 5.3, Fig. 5.4 and Fig. 5.5, respectively. The Influences by the external fields (like MT field) are although significant, specially in the lower frequencies of the data even though throughout the analysis we will restrict only to influences by the oceanic origin. The ocean
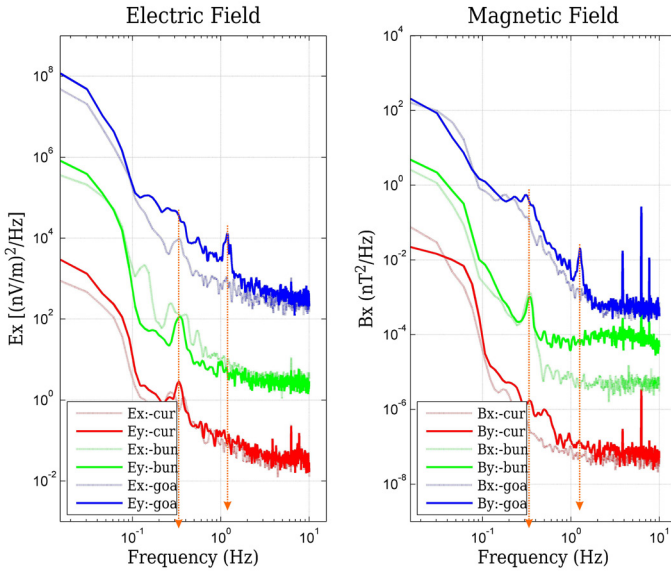
Figure 5.2: The PSD of the shallow stations. Dotted and solid lines represent the E_x and E_y components, respectively. Red, green and blue lines represent the stations Currawong, Bunyip and Goanna, respectively. The stations are displayed 100 units apart form each other for clarity. The scales are appropriate for the lower most spectra. The orange dotted two vertical lines show the prominent peaks observed in the PSD.

is known to act as low-pass filter, which restrict higher frequencies to reach at the ocean floor. Therefore, from the sea surface only frequencies lower than a limiting frequency can reach to the ocean floor. A calculation using the penetration depth formula (Eq. 3.22) suggests that the limiting frequency is 0.12 Hz, 0.118 Hz and 0.115 Hz for Currawong, Bunyip and Goanna respectively. This suggests that from the sea-surface, say less than 0.12 Hz can only reach to the ocean-floor. In spectrograms, strong peaks are apparent in the frequency range greater than 0.12 Hz, which suggest that their origin is by the internal oceanic processes. A detailed analysis of these features might help in understanding their source nature. In the spectrogram the noted significant observations are as follows:

Currawong (Fig. 5.3)

1. E_x *component :* A high power feature is evident in the frequency range around at 0.32 Hz. With increasing time, the power of the feature migrates towards lower frequencies (towards 0.2 Hz).
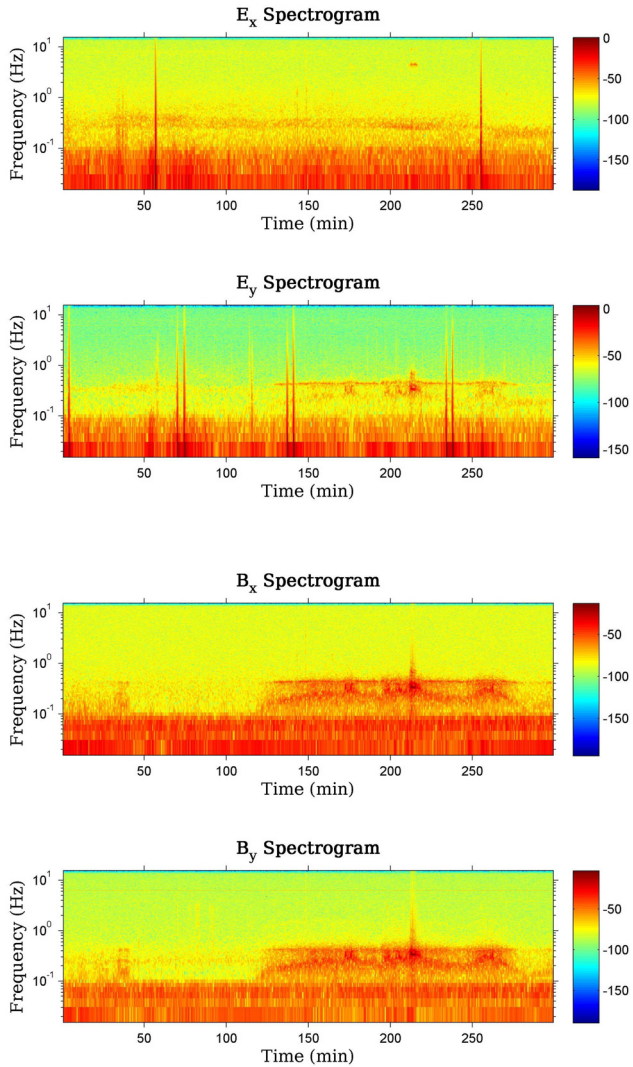
Figure 5.3: The electric and magnetic field spectrogram of the Currawong (300 m) depth station.
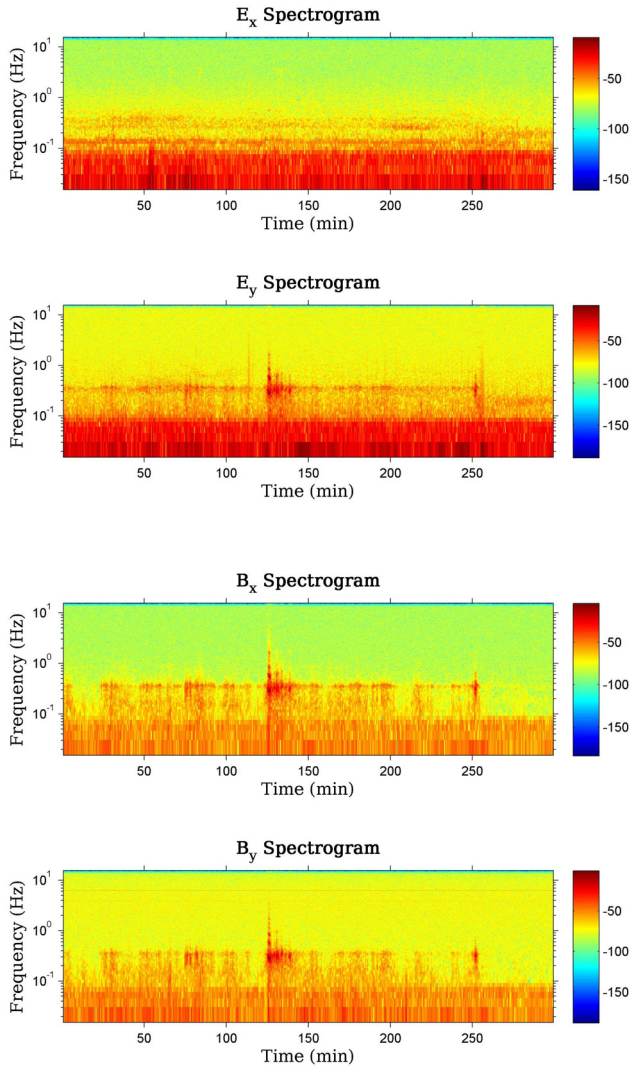
Figure 5.4: The electric and magnetic field spectrogram of the Bunyip (325 m) depth station.
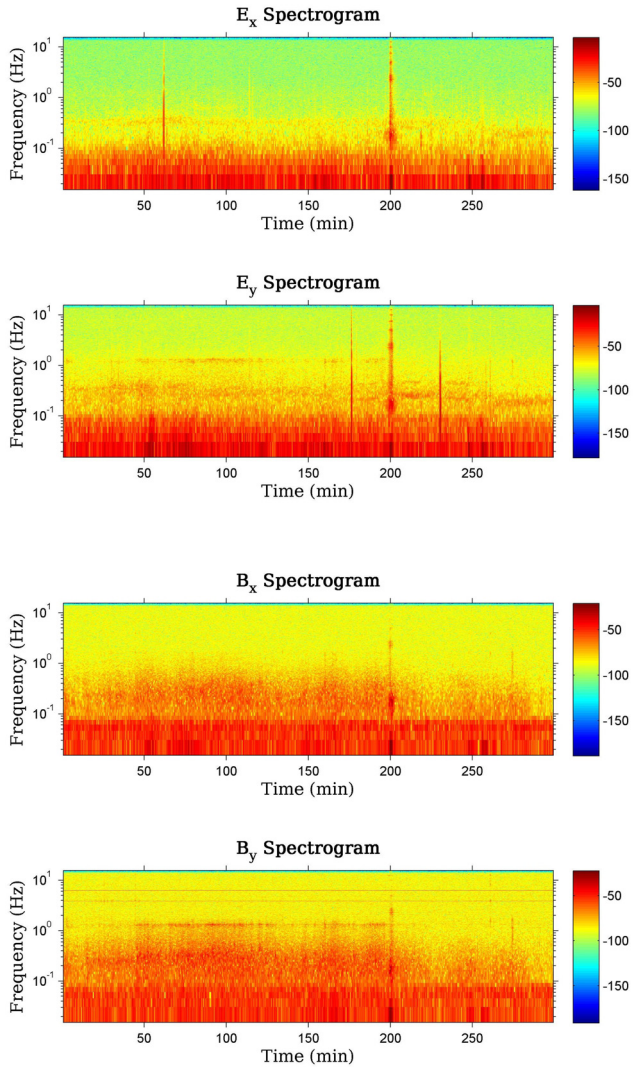
Figure 5.5: The electric and magnetic field spectrogram of the Goanna (360 m) depth station.

2. E_y *component :* In the time interval between 130 and 270 minutes, a high power feature at 0.4 Hz is apparent. An associated haziness (in same time range as 0.4 Hz) is evident, which extends towards the lower frequencies. The term haziness denotes the spectral energy distribution over a limited frequency range. Note, we will use haziness term quite often in this chapter.

3. B_x *and* B_y *components :* The spectral contents are similar to that of the E_y component observations. The hazy features associated with 0.4 Hz, extending towards the lower frequencies are prominent. The similar time range of the 0.4 Hz and haziness suggest that they are associated with each other.

Bunyip (Fig.5.4)

1. E_x *component :* A feature corresponding to 0.32 Hz is evident. Like the Currawong E_x component, the power shifts towards lower frequencies (0.2 Hz) are also apparent in this station. Another prominent steady time ambient feature can be observed at 0.13 Hz.

2. E_y *component :* A steady feature at 0.37 Hz is evident, with an associated haziness extending towards lower frequencies.

3. B_x *and* B_y *components :* The observations are similar to that of the E_y component.

Goanna (Fig.5.5)

1. E_x *component :* A feature at 0.32 Hz is evident, with increase in time power of this feature shifts towards the lower frequencies.

2. E_y *component :* Two features, one at 1.2 Hz and the other at 0.32 Hz are evident. The 0.32 Hz feature shows a power shift towards the lower frequencies (0.2 Hz), with increasing time.

3. B_x *and* B_y *components :* A haziness involving a broad frequency range (0.7 to 0.1 Hz) is evident. The 1.2 Hz peak is evident in the B_y component.

Oceanic processes are a likely source for the above observed features. A significant contribution at the ocean bottom by direct influence of the swell is unlikely as swells experience heavy damping and can hardly penetrate some tens of meters. However, some surface gravity waves like ocean tides and tsunamis can reach the ocean floor. Note that the starting day of data acquisition (i.e. 9 April 2005) is a new moon day. Oceanic tides influence is therefore expected, prominently in the shallow stations. The 0.32 Hz is of course not a tidal frequency but tides can induce waves with higher frequencies (Ezer *et al.* 2010) and therefore let us hypothesize 0.32 Hz as a contribution by the tidal induced motion. To support the hypothesis, it would be logical to show a time dependence and regional nature of the feature. The regional nature demands a presence in every station. The time dependence demands a similar time presence in each station. Evidently, 0.32 Hz can

be noted in all the three stations. The observation therefore satisfies the regional nature demand. We will now look the spectrogram to find the observation for another demand. We observed a spectral power shift towards the lower frequencies corresponding to 0.32 Hz. The time presence of the feature in each station is similar(from 0 to 300 minutes). The shift in the frequency content is possibly due to change in oceanic environment caused by the rotation of the earth ($\approx 15°$ in 1 hr). The start time of the spectrogram corresponds local time of 12 PM (night side). In 5 hour duration (time length of spectrogram), the facing of a station will change from the night side to the day side. Tidal influence will be more in the night time than the day time and thus can change the properties of the tidal induced waves. The observation of the spectral power shift therefore satisfies our another demand of the time dependency too. Moreover, a further strength to the hypothesis is provided by the strong presence of 0.32 Hz in the E_x component (in Bunyip and Currawong station). Stronger strength in one component represents the directional nature of the source. A directional tide might induce a directional motion. The overall observations indicates 0.32 Hz as a possible contribution by a tidally induced motion.

The spectrograms of the magnetic components (B_x and B_y) show a strong identical feature between the time interval 125 to 275 min., approximately. The peak frequency of the feature is about 0.4 Hz. We observe an associated haziness which extends towards the lower frequencies starting form 0.4 Hz. The time duration and peak frequency of the feature resembles with the feature observed in the E_y component. We observe similar observations in the Bunyip station too. Here, the B_x and the B_y spectrograms show 0.37 Hz and associated haziness which extend towards the lower frequencies in a time interval between 0 to 250 min. The time duration and peak frequency of the feature also resemble the E_y component. The pattern resemblance of the E_y, B_x and B_y components is a significant observation and demands an explanation. Before presenting an explanation, we will analyze the spectrograms of the deeper stations.

5.3   Analysis of the deeper station data

The deeper stations are Shark, Lorrie and Corella with depths 650 m, 675 m and 700m, respectively. Let us examine the spectral nature of the data recorded in these stations.

5.3.1   Power Spectral Density

Six minutes of data is utilized to generate the PSD. The obtained electric and magnetic field spectra are shown in the Fig. 5.6. Three station spectra show a sharp increase in the power below 0.1 Hz. Above 0.1 Hz, many peaks are evident. Two spectral peaks are distinct, one at 1.2 Hz and other at 0.25 Hz. They are evident in the both electric and magnetic spectra. Corella and Lorrie show a clear presence of 1.2 Hz, while it is not very clear in the Shark data. A strong power of the spectral peak in the Corella data signifies an influence of a local source. Plausibly the topography might have played a role
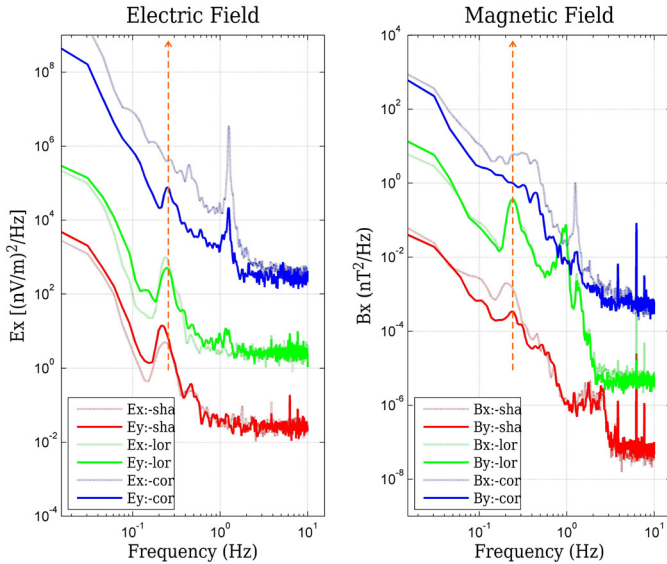
Figure 5.6: The PSD of the electric (left) and magnetic (right) field. Dotted and solid lines respectively represents the E_x and E_y component. A vertical dashed line is drawn corresponding to the 0.25 Hz peak.

in enhancing the strength. We will investigate this issue in later sections. Moreover, the peak at 0.25 Hz is apparent in all three deep stations (in both E and B PSD). Unlike the other two stations, Corella shows a weaker strength. Probably the strength of the spectral peak is topography influenced. Like 0.32 Hz (observed in every shallow station PSD), 0.25 Hz is also apparent in all the three stations. Let us examine the spectrograms to explore the spectral details in time.

5.3.2 Spectrogram

For the shallow station case, spectrograms are plotted using 5 hours of data but for the deeper station case we will use 24 hours of data, the purpose to show the time based spectral characteristics of 1.2 Hz peak, which will be not come up with 5 hour plotting. The spectrograms are shown in Fig. 5.7, Fig. 5.8 and Fig. 5.9 corresponding to Shark, Lorrie and Corella stations, respectively. For greater depth stations, the limiting frequency suggested by the depth of penetration (Eq. 3.22) formula is 0.1 Hz. We therefore expect influence from the ocean surface below 0.1 Hz. The spectral features greater than 0.1 Hz is likely by the sources with in the ocean. The observations from the spectrogram are as

follows:

Shark (Fig.5.7)

1. *E_x component :* A high power feature is evident approximately at 0.25 Hz. This is a time ambient feature.

2. *E_y component :* The 0.25 Hz is also evident here in form of a time ambient high power feature. Close to 1000 min., we observe a peak at 1.2 Hz. This spectral feature holds a greater power and haziness, which extends toward the lower frequencies.

3. *B_x and B_y components :* Like electric field components, a time ambient feature at 0.25 Hz is apparent in both magnetic components. At approximately 1000 min, a feature at 1.2 Hz is evident in both the magnetic components. This feature was also observed in E_y component. The haziness and some prominent features in both the magnetic components are similar to each other.

Lorrie (Fig.5.8)

1. *E_x component :* Time ambient high power feature is evident at 0.25 Hz. At some instances vertical stripes are prominent.

2. *E_y component :* Time ambient high power feature at 0.25 Hz is also evident here. Vertical stripes creating haziness is also evident. Most of the vertical stripes end by showing a high power at 1.2 Hz.

3. *B_x and B_y components :* Time ambient 0.25 Hz is evident in both the magnetic components. The haziness and overall spectral pattern evident in both the magnetic components are similar to each other.

Corella (Fig.5.9)

1. *E_x component :* Time ambient high power feature is evident at 0.25 Hz. At 1.2 Hz frequency, a temporary high power feature is apparent in spectrogram. Between the time interval 700 min to 1100 min, we observe a power switching. First, 1.2 Hz feature shows a low power approx. between time interval 700 min to 900 min. and thereafter it shows a high power with associated vertical haziness in time interval approx. between 900 min to 1100 min.

2. *E_y component :* Like E_x component, the time ambient high power feature of 0.25 Hz is also apparent in the E_y component. The temporary feature of 1.2 Hz, which is present in the E_x component, is also evident in the E_y component with approx. at similar times. Note the low and high power switching of the 1.2 Hz between the time interval 700 min to 1100 min. The power switching of the E_y component is different than the E_x component. Here, first 1.2 Hz show a high power and thereafter low power. High power holds vertical haziness in time range (700-900 min) .

3. *B_x and B_y components :* The 1.2 Hz feature corresponds the electric field timings. The vertical haziness is evident in both components of the magnetic spectrograms, showing similar spectral contents.
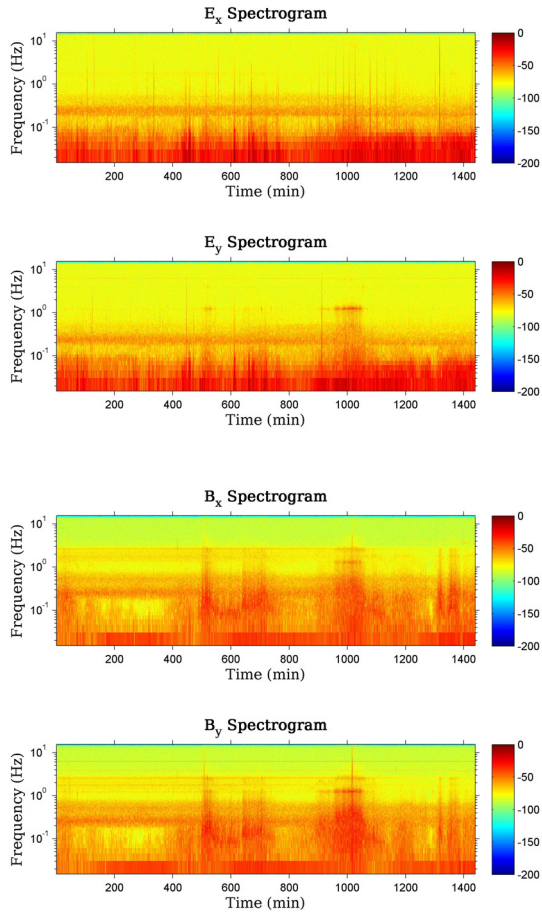

Figure 5.7: The electric and magnetic field spectrogram of the Shark (650 m) depth station.

A first common observation is the time ambient spectral feature at 0.25 Hz. In the case of shallow stations, we explained spectral shift of 0.32 Hz towards lower frequencies
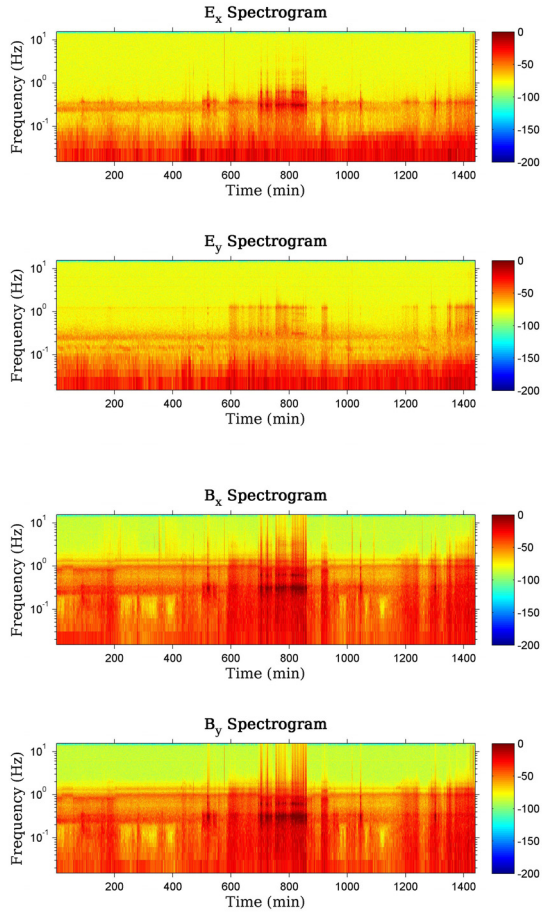
Figure 5.8: The electric and magnetic field spectrogram of the Lorrie (675 m) depth station.
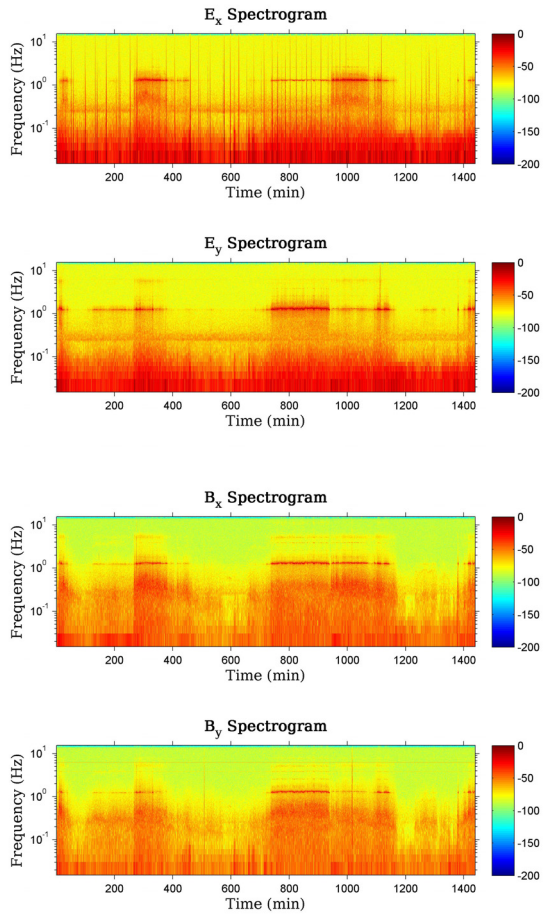
Figure 5.9: The electric and magnetic field spectrogram of the Corella (700 m) depth station.

by the tidal induced motion. Here, we do not observe spectral shift, which possibly is a significant property of the tidal induced motion, with 0.25 Hz and therefore we need a different explanation. In general at the sea surface, depending on the weather conditions, there occurs a variety of wave-wave interactions that could create standing waves, which will have phases varying slowly over the sea surface. At greater depth, they will create a horizontal pressure gradient and therefore horizontal water current, which will induce electromagnetic field (Cox, 1978) to be sensed by the electromagnetic sensors placed over the floor. The wave-wave interaction covers a big area and therefore they are capable to show their presence in many nearby recording stations (regional nature) simultaneously. The 0.25 Hz is a regional feature and is apparent in all the three stations data. The mechanism plausibly explains the observation. A second common observation is the similarity of the B_x and the B_y component. This observation was also noted in the shallow depth spectrograms. Moreover, a resemblance between the E_y component and horizontal magnetic components (i.e. B_x and B_y) was also apparent in the shallow depth stations (Currawong and Bunyip spectrograms). The similarity in E_y, B_x and B_y components are apparent in the deeper stations. An explanation for these observations is demanding as it may explain the electromagnetic signal characteristic close to the ocean floor.

5.4 Sea-floor topography

For a station, the haziness (i.e. spectral energy distribution over a limited frequency range at certain times) apparent in the B_x and B_y components are similar. They differ from station to station. The spectral patterns of the same component in the two stations data are also not alike. Therefore the observation suggests a local influence. The dissimilarity at identical time further supports the argument. Topography could be a possible influencing factor. The sea-floor topography map of the region is shown in the Fig. 5.10. Station locations are marked.

Among the electromagnetic field components, the vertical component will undergo major distortion by the topography due to their strong sensitivity for the conductivity and the velocity (topography perturbed) changes. The vertical electric (i.e. E_z) field is a TM mode creation. On the other hand vertical magnetic (i.e. B_z) field is a TE mode creation. This suggests that both the mode, TE and TM, are distorted by the topography. Schwalenberg and Edwards (2004) figured out that on the sea floor the magnetic components are distorted in the TE mode while electric components are distorted in the TM mode.

The mMT recordings are generally made by keeping the x- and y- components respectively towards the North and East directions. Let the coordinate system used for theoretical calculations are similar to the setting of the data recording. The TE mode components, created by the poloidal velocity field (V_y and V_z) are $E_x, \mathbf{H_y}, \mathbf{H_z}$, while the TM mode components created by the toroidal velocity field V_x are $B_x, \mathbf{E_y}, \mathbf{E_z}$. Note, the bold font denoted magnetic and electric components corresponds the topography distorted fields. Let us consider Currawong case, where the occurrence of 0.4 Hz (time interval:
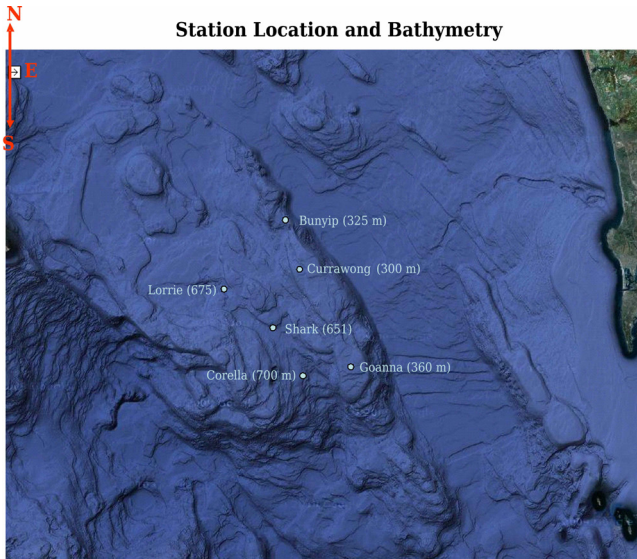
Figure 5.10: Detailed topography map of the ocean floor with station locations. Small circular marks represent the station locations. Name of the respective stations are written at a side of mark. Small bracket contains the depth of stations from the subsurface

125-300 min.) is only apparent in one of the electric field components i.e. E_y component. The E_y field can be distorted by the topography and therefore 0.4 Hz is most likely a consequence of the same. The absence of 0.4 Hz in the E_x component further supports the reason, as the E_x component can not be influenced by the topographic distortions.

The presence of 0.4 Hz in the E_y component spectrogram suggest its creation by the V_x field, as it is a TM mode field. The B_x component is also a TM mode creation and thus it will be also created by the same velocity field. If the argument is correct we should observe 0.4 Hz feature also in the B_x spectrogram. Evidently, the 0.4 Hz (time interval: 125-300 min.) feature is present (Fig. 5.3) here too. But if 0.4 Hz is by the topographic influence we should not observe this feature in the B_x component as this field (not a bold font fields) will not be distorted by the topography. This contradicts the observation. We will back on this issue in the next paragraph. Moreover, corresponding to the 0.4 Hz (time interval: 125-300 min.) of the B_x component, we observe a similar spectral behavior in the B_y component too. Contrary to B_x component, the B_y component can be influenced by the topographic distortions. Noteworthy point is B_y field is a V_y and V_z field creation and we explained 0.4 Hz as a V_x field creation. The observation also contradicts the result.

The resemblance of the B_x and B_y component suggests a common source for their excitation, which implies a role of the E_z field. The E_z field is a V_x creation (TM mode field)

and can be distorted by the ocean-floor topography. This explains both the contractions of **a)** the observation of topographic distortion in the B_x field and **b)** the influence of the V_x field in the B_y component. In other words, if E_z field plays a role in the B_x and B_y field creation, then we can observe the influences by the topographic distortions in the B_x and B_y components too, as E_z field experiences the topographic distortions. Moreover, as the E_z field is created by the V_x field and therefore we will see the effects of the V_x field in both the magnetic components.

Above explanation describes the reason for the spectral resemblance in E_y, B_x and B_y fields, observed in all the stations (both shallow and deep). In all the stations, the horizontal magnetic fields are found more distorted than the horizontal electric fields. The observations suggest that the horizontal magnetic fields are more sensitive to the velocity and topographic variations than the electric field. Every deep station spectrograms (Fig. 5.7, 5.8, 5.9) show a 1.2 Hz peak in their E_y component. Exception is Corella, where 1.2 Hz is also present in the E_x component. Among shallow stations, the peak is evident only in the Goanna spectrogram (Fig. 5.5). Please note, here also the peak is only in the E_y component. The observation suggests that the peak is a V_x field contribution. The peak is a function of time and is associated with some vertical haziness, therefore a role of topography is most likely.

5.5   Role of the topography gradient

The prevailing pressure gradient at the ocean floor (Cox, 1978) can generate a wave oscillation modulated by the ocean floor topography. These waves are expected to show the following characteristics:

1. Local influence in observation: The slope environment in the vicinity of a station may probably help in creating a spectral feature. This is because a wave motion is anticipated to be influenced by the slope.

2. Local spectral characteristics: The spectral characteristics would be influenced by the undulations in the topography. A almost flat (long wavelength undulation) topography would create a wave of very low spectral range while a short wavelength strong undulation in topography would support a wave of high spectral range. This suggests a dissimilar spectral appearance of the feature among the stations.

To check the hypothesis and understand the involved physics, topography gradients are calculated. A 2-minute Gridded Global Relief Data (ETOPO2, 2001) is utilized for the gradient calculation, which has a horizontal resolution of 2-minutes of latitude and longitude (1.853 km at the Equator). The vertical resolution is 1 meter. The vertical resolution is considerable, which is prime matter of interest for our study to understand the role of the slope of seafloor topography. The topography detail of the ocean floor (shown in the Fig 5.10) suggests an undulating topography in the vicinity of the stations and therefore a slope may play a significant role. The numerical gradients (differences)

are calculated for the slope study. The vertical variations (z) with respect to the changing latitude (x) and longitude (y) defines the gradient and is therefore calculated by

$$\nabla z = \frac{\partial z}{\partial x}\hat{x} + \frac{\partial z}{\partial y}\hat{y} \tag{5.1}$$
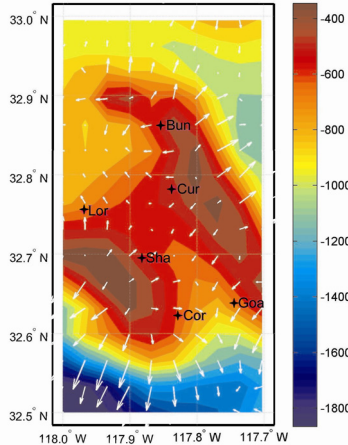

Figure 5.11: Gradient map superimposed on the bathymetry contour. The magenta stars show the station locations and their short names. The white arrows represent the velocity gradient and their length represents the strength. The color bar represents depth from the surface.

The obtained map is shown in Fig. 5.11. Arrow represents the strength and direction of the gradient. Evidently, the gradient scenarios near Bunyip and Currawong stations are similar. In Goanna the gradient is much stronger (compared with the Bunyip and Currawong) and therefore if a slope matters, an electromagnetic feature due to the gradient is anticipated. Note that the spectral feature at 1.2 Hz is only present in the Goanna data (absent in the Bunyip and Currawong), in the E_y component. Absence of the feature in other two shallow stations indicates a possible role of slope in the creation. Evidently, the feature is temporary in time. The constant spectral nature (constant frequency) of the feature is worth mentioning.

The deeper stations of Shark, Lorrie and Corella also show a significant gradient and therefore a spectral feature by slope is anticipated here too. The 1.2 Hz feature is evident. A vertically varying haziness is also evident with the feature. Haziness and 1.2 Hz is always found connected and this indicates a close connection in their genesis process. Most likely, the surrounding topography near station is controlling the haziness. The dissimilar-

ity of the haziness among stations supports the argument. The haziness is therefore a local creation. Since haziness and 1.2 Hz are connected with each other, 1.2 Hz is probably a local creation too. Moreover, the time presence of 1.2 Hz and haziness among stations is also different, which also supports the idea of a local source. The comparison of the shallow and deeper station data indicates that the 1.2 Hz is present only in those stations where the slope or topography gradient is significant. The observation also suggests that the topography has played a significant role in the formation of 1.2 Hz.

The slope of topography might explain a spectral peak and detail of topography (undulations) might explain the haziness association with the peak. A question still open is the observation of the fixed spectral peak i.e. 1.2 Hz. A mechanism is therefore required to explain the fixed frequency of 1.2 Hz? It is hard to explain at the moment, we leave it as a significant observation to explain.

5.6 Modeling

Till now we have discussed the PSD's and the spectrograms of the shallow and the deep stations. In this section, we will model background shape of these PSD's. The purpose of the modeling is to check the consistency with the theoretical formulation. Moreover, we can obtain some additional information from the match and mismatch of the spectral ranges. In the chapter 3, PSD simulations are done using only the electric field data. However, here as we have both electric and magnetic field data. It would be interesting therefore to observe the fit for both the electric and the magnetic field data by a single model. The response is calculated for a model consisting an ocean and the sediments of conductivity 3.33 S/m and 1 S/m, respectively. The depth of the ocean is chosen equal to the stations depth. Therefore, we choose 300 m, 325 m, 360 m, 650m, 675 m and 700 m ocean depth corresponding to stations Currawong, Bunyip, Goanna, Shark, Lorrie and Corella, respectively. The TM mode theory (see Section 2.5) will be used for the modeling. We have divided the ocean of depth (t) in to five layers that is $t = [t_1, t_2, t_3, t_4, t_5]$. The thickness of first, second, third and fifth layer is always kept constant (for both the shallow and deep stations) and is 100 m, 50 m, 50 m and 5 m, respectively. Only the fourth layer thickness is changed to attain the station depth. For example, layers thickness for the Shark is taken as $t = [100, 50, 50, 445, 5]$. The fourth layer thickness is chosen 445 m to attain the depth of Shark station (650 m). Different velocities are assigned to each layer. The used velocity model is $[0.01, 10^{-4}, 10^{-5}, 10^{-6}, 2 \times 10^{-6}]$. Each layer velocity represents the average velocity in the layer.

A magnetic power spectra measured on land by Vozoff (1991) is utilized (Fig. 3.11) to derive the field at the ocean floor. The downward continuation which utilizes damping theory gives the spectra at the floor. An identical velocity model is used to model the both, shallow and deep stations spectra. We considered a constant wavelength of 110 m and a vertical magnetic field of 3.96×10^{-5} Tesla (approx. similar to the acquisition area field). We are not trying to simulate the true velocity field, just wanted to test which
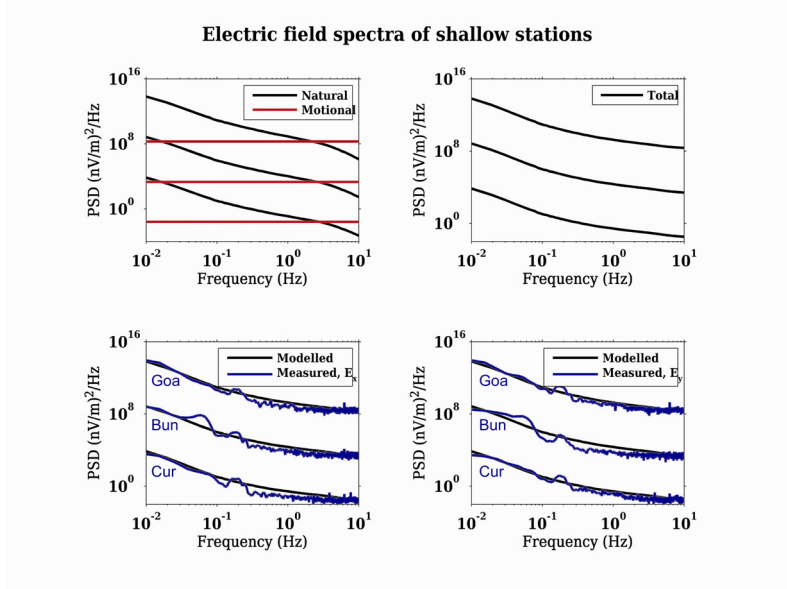
Figure 5.12: In each panel the top, middle and bottom spectra respectively correspond to Goanna (360 m), Bunyip (325 m) and Currawong (300 m) stations. **(a) Top-left panel:** Spectra for the naturally (black line) and motionally contributed (red line) field at the ocean floor. **(b) Top-right:** Total field (sum of naturally and motionally contributed field) at the ocean floor. **(c) Bottom-left:** Comparison of the modeled (black line) and the measured (blue line) electric (E_x component) field. **(d) Bottom-right:** Comparison of the modeled (black line) and the measured (blue line) electric (E_y component) field. Each Spectra in a panel is 10^5 units apart for clarity. The scales are appropriate for the lower most spectra.

velocity model and wavelength are required to explain the general shape. In strict sense, velocity and wavelength close to the ocean floor (i.e. here, fifth layer) are significant for the simulation of the PSD's. Above the ocean floor we assumed a layer of 5 m thickness and a velocity 2×10^{-6} m/s. Since the local topography will control the wavelength and velocity, therefore we can choose separate wavelengths to model different stations spectra. Even though we have used a fixed wavelength (110 m), just to maintain the simplicity and avoid the complications of the modeling. The modeling results for shallow and deep stations are respectively shown in the Fig. 5.12, Fig. 5.13 and Fig. 5.14, Fig. 5.15. In all the six stations, the spectral estimate of the electric and the magnetic field amplitudes in the low frequency range correspond to the decay of the natural field with depth. Over all, a reasonable match is evident. The magnetic components of Currawong and the electric components of Goanna show an excellent match with the modeled response. In general,
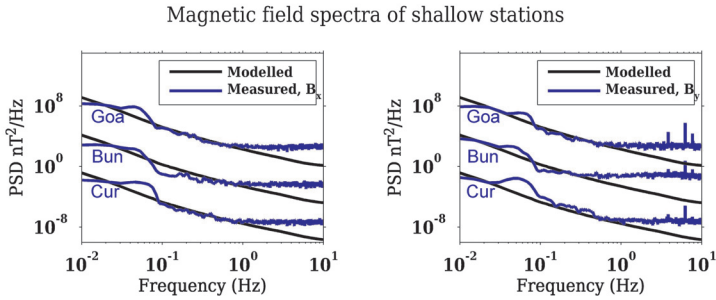
Magnetic field spectra of shallow stations

Figure 5.13: In each panel the top, middle and bottom spectra respectively correspond to Goanna (360 m), Bunyip (325 m) and Currawong (300 m) stations. **(a) Left:** Comparison of the modeled (black line) and the measured (blue line) magnetic (B_x component) field. **(b) Right:** Comparison of the modeled (black line) and the measured (blue line) magnetic (B_y component) field. Each Spectra in a panel is 10^5 units apart for clarity. The scales are appropriate for the lower most spectra.
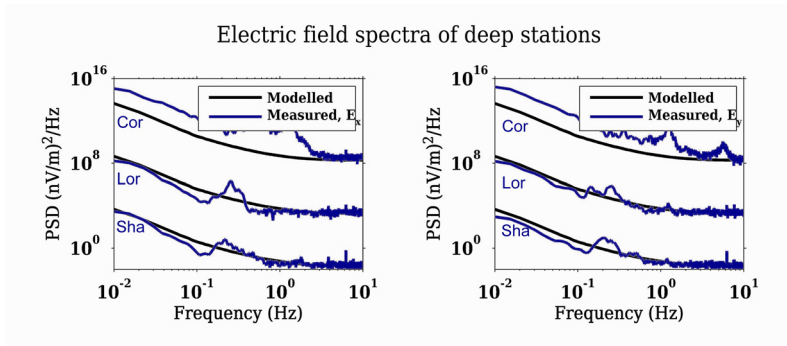
Electric field spectra of deep stations

Figure 5.14: In each panel the top, middle and bottom spectra respectively correspond to Corella (700 m), Lorrie (650 m) and Shark (675 m) stations. **(a) Left:** Comparison of the modeled (black line) and the measured (blue line) electric (E_x component) field. **(b) Right:** Comparison of the modeled (black line) and the measured (blue line) electric (E_y component) field. Each Spectra in a panel is 10^5 units apart for clarity. The scales are appropriate for the lower most spectra.
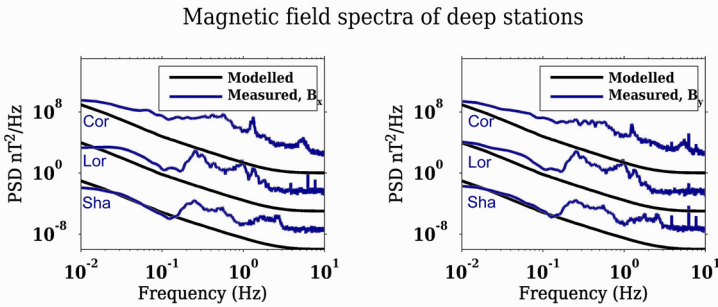
Figure 5.15: In each panel the top, middle and bottom spectra respectively correspond to Corella (700 m), Lorrie (650 m) and Shark (675 m) stations. **(a) Left:** Comparison of the modeled (black line) and the measured (blue line) magnetic (B_x component) field. **(b) Right:** Comparison of the modeled (black line) and the measured (blue line) magnetic (B_y component) field. Each Spectra's in a panel is 10^5 units apart for clarity. The scales are appropriate for the lower most spectrum.

the mismatch is pronounced in the higher frequency range, strongly in the magnetic components. There could be two possible reasons: i) distortion by the complex signals of seismic origin ii) the distortions by the topography. The modeling of the deeper station data are shown in Fig. 5.14 and Fig. 5.15. Evidently, the electric field spectra of the Shark and the Lorrie station data show a strong match with the modeled spectra while a difference can be noted in their magnetic field spectra. Most likely, the difference is caused by above mentioned two reasons (i.e. i and ii). The electric and magnetic components of Corella station do not fit the modeling results. The strong motionally induced signals, controlled by the topography might a probable reason behind the discrepancy in observations. The geological placement of the station [in a V-valley (see Fig. 5.10)] supports the reasoning. A V-valley kind of topography may support a long time water wave oscillations, because of consistent reflections of the waves. These persistent oscillations are capable to create a strong electromagnetic field.

5.7   Pressure

Bernoulli's principle for an inviscid flow (no viscosity) states that a decrease in pressure simultaneously causes an increase in the speed of the fluid. The principle suggests a relation between the pressure and speed. For an incompressible flow, a common form of Bernoulli's law (Feynman *et al.* 1963) is:

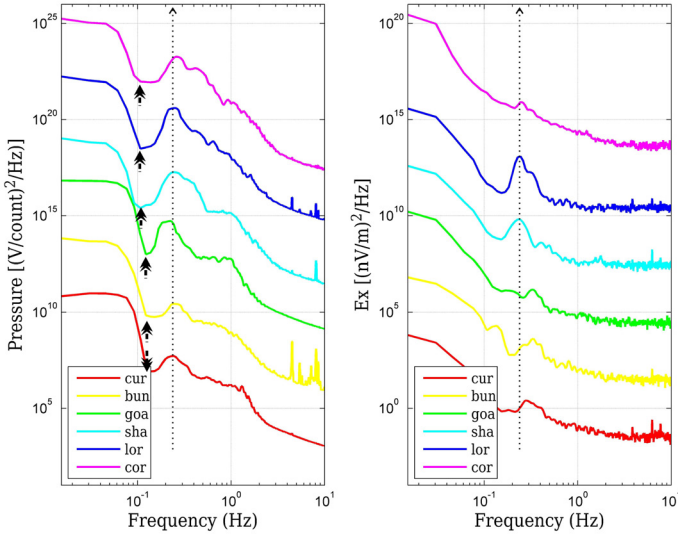$$\frac{V^2}{2} + gt + \frac{P}{\rho} = \text{constant along a streamline} \qquad (5.2)$$

Figure 5.16: The power spectral density of the pressure (left panel) and electric (E_x component) field (right panel). The legends cur, bun, goa, sha, lor, cor respectively represent the corresponding PSD's of stations Currawong, Bunyip, Goanna, Shark, Lorrie and Corella. A vertical dotted arrow is drawn corresponding to 0.25 Hz. The bold double arrows at 0.12 and 0.1 Hz represents the spectral shift observations. Each spectrum is 1000 unit shifted from the lowest one. The absolute scales are therefore only appropriate for the Currawong (cur) spectrum.

where, V represents a speed at a point on a streamline, g is the acceleration due to gravity, t is the elevation of the point from reference point, P is the pressure at the selected point and ρ is the density of the fluid. Multiplying the eq. 5.2 with mass presents the equation in terms of the energy i.e

$$\frac{1}{2}mV^2 + mgt + \frac{m}{\rho}P = \text{constant along a streamline} \tag{5.3}$$

The first and second term respectively represents the kinetic energy ($\frac{1}{2}mV^2$) and potential energy (mgt) of the flow. Evidently, if the potential energy or pressure will decrease then the fluid flow will increase (therefore kinetic energy too) to conserve the total energy. The obvious relationship between pressure and speed suggests an indirect connection between the motionally induced electric field and the pressure.

Initial six minute data is used for calculation of the power spectral density (PSD). To
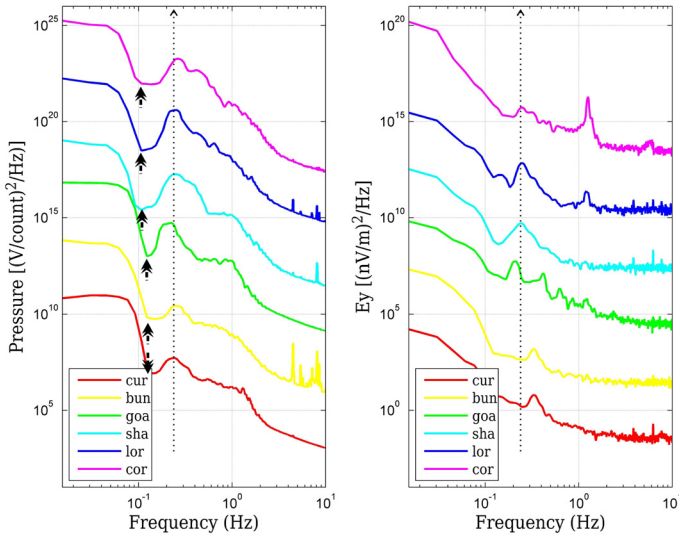
119

Figure 5.17: The power spectral density of the pressure (left panel) and electric (E_y component) field (right panel). The legends cur, bun, goa, sha, lor, cor respectively represent the corresponding PSD's of stations Currawong, Bunyip, Goanna, Shark, Lorrie and Corella. A vertical dotted arrow is drawn corresponding to 0.25 Hz. The bold double arrows at 0.12 and 0.1 Hz represents the spectral shift observations. Each spectrum is 1000 unit shifted from the lowest one. The absolute scales are therefore only appropriate for the Currawong (cur) spectrum.

compare the PSD of the pressure and the electric field, we plot them together in a figure. The Fig. 5.16 shows the PSD of the pressure with the E_x component and Fig. 5.17 shows the pressure PSD with the E_y component. Evidently, the pressure PSD holds a peak at 0.25 Hz and thereafter it looses power and shows a minimum. Note the spectral minimum frequency for shallow and deep stations. It is approximately at 0.12 Hz in shallow stations and 0.1 Hz in deeper stations (represented by arrows). A sharp rise in the pressure field is evident with decrease in frequency starting from 0.1 Hz and 0.12 Hz for deep and shallow stations, respectively. A pressure low and thereafter a rise indicates a possible role of surface wave. Greater than a limiting frequency influence by surface-waves will be absent and this may cause a pressure low. On the other hand, lower than the limiting frequency influence of surface-waves would be significant, which may lead to a sharp rise in the power. A careful observation suggest that the slope of the power rise in the shallow stations are slightly steeper than the deeper one. The observation indicates an influence by the surface waves as the deeper stations can only be influenced by the waves of greater

wavelengths than the wavelengths required for the shallow stations. The number of waves influencing the shallow station will be therefore more than the deeper stations, which may provide more energy to the shallow stations than the deeper one. The observation of slope is therefore consistent with the possible influence by the surface wave. Another striking observation is the width of the spectral low zone. The zone is wider for the deeper and a little narrower in shallow stations. In connection, this further supports the influence by the surface waves.

The pressure spectra of all (both shallow and deep) stations show a prominent peak at 0.25 Hz (marked by a single dotted arrow). The deeper stations spectra of horizontal electric field (both E_x and E_y) also contain a peak at 0.25 Hz. The careful notice suggest that the peak is also present in the E_x component of the shallow stations although the presence is weak.

Previously (Section 5.3) we explained the 0.25 Hz peak, noted in the deeper stations electric field data, by a mechanism of wave oscillation created by a pressure gradient at the ocean floor. The pressure gradient creates a velocity which induces an electric field. The presence of a 0.25 Hz peak (observed in the electric field data) in pressure spectrum therefore supports the mechanism and explains the reason for the peak. However, in the electric field data of the shallow stations, the presence of 0.25 Hz is not clear. The pressure spectra contains a peak at 0.25 Hz and therefore demands for an identical peak (i.e. 0.25 Hz) in electric field spectra too for the consistency of the above mechanism. A careful notice may lead us to see the peak in the E_x component, the strong peak at 0.32 Hz (apparent in shallow stations) is masking it.

In the shallow stations, the peak at 0.32 Hz is prominent in the electric field data but not in pressure data. On the other hand the peak at 0.25 Hz is prominent in pressure data but not in electric field data. The 0.32 Hz peak was explained (Section 5.2) by the tidally induced motion while 0.25 Hz (Section 5.3) peak was explained by the pressure gradient. Electric field is sensitive to the motions of both the horizontal and vertical components while the pressure field will be sensitive only to the vertical components. The likeliness of the lack of the strong vertical component with 0.32 Hz peak explains the observed spectra.

The presence of the similar peak in the electric and pressure fields of both shallow (weak presence) and deep stations (strong presence) suggests a correlation between two data sets. This will be our next step.

5.8   Cross-correlation

The cross-correlation analysis is a measure of the similarity between two waveforms. One waveform is displaced with respect to the other and corresponding values are multiplied and thereafter summed with each other. The obtained value is a cross-correlation value for a corresponding time shift. Normalization is done to obtain a value between +1 to -1. The product of approximately similar waveforms will usually be positive and therefore the cross-correlation will be large. Dissimilar waveforms will give small cross-correlation

as some of the products will be positive and some will be negative. A large negative value of the cross-correlation suggests that most part of one waveform is out of phase with the other.

Mathematically, the cross-correlation (Bendat & Piersol 1986) of the two waveforms X_i and Y_i are expressed as

$$C_{XY}(\tau) = \sum_i X_i Y_{i+\tau} \qquad (5.4)$$

where i represents the data points, τ is the lag or lead of Y_i with respect to X_i.

The expression for a normalized cross correlation at zero lag is

$$C_{XY}(0) = \frac{1}{\sqrt{C_{XX} * C_{YY}}} \sum_i X_i Y_i \qquad (5.5)$$

Here, $C_{XY}(0)$ represents cross-correlation of waveforms X_i and Y_i at zero lag. C_{XX} and C_{YY} are zero lag auto-correlation of X and Y waveforms.

The reason to calculate the cross-correlation is the previous section observations, which indicated a possible similarity of the pressure field with the electric field. Cross-correlation is therefore an obvious choice. We found the small magnitude of cross-correlation for a large time length of the electric and pressure waveforms, despite that they show a similar spectral content. Therefore we calculate windowed cross-correlation to see whether there is temporarily good correlation. The technique of 'moving window cross-correlation at zero lag' is used for the calculation. In this technique, the cross-correlating waveforms are first divided into segments of equal window length. The corresponding windows are thereafter cross-correlated at a zero lag. Normalisation is done to rate the similarity from 0 to ±1.

The present experiments are made using initial two hour of time series data. The data is divided in to 120 segments, each of one minute (window) length. We choose time length of one minute duration as it sufficiently describes the frequency range of interest. As we mentioned above, the consideration of a larger waveform will cause decrease in correlation magnitude. For example, we have observed a correlation magnitude 0.1 at zero lag by cross-correlating pressure and electric filed waveform of 10 minute duration. In the present case, we cross-correlate with the pressure waveforms with the corresponding time electric and magnetic fields. The experiments are done for all the 6 stations. The obtained plots representing cross-correlation values with time are shown in the Fig 5.18. The correlation is sometimes positive, sometimes negative. This probably excludes a direct mechanism how pressure controls electric field. Sometimes they are in phase and sometimes out of phase. Mostly, the correlation magnitudes are greater than ±0.5. Comparatively, the deeper stations (right column) show a consistently stronger cross-correlation magnitude than the shallower stations (left column). The pressure and magnetic field cross-correlation magnitudes are stronger in the shallow stations than the deeper ones. Shark and Lorrie shows very weak values. The observations suggest a poor cross-correlation between pressure and magnetic field in deeper stations. From Fig. 5.18, it is clear that there is no simple relationship between pressure and electric/magnetic field.

The strong correlation magnitude, specially in deeper stations where sometimes it is 0.9, indicates for a relationship, must be of a complicated nature. We have found 0.25 Hz spectral peak in both pressure and electric field PSD, let us utilize it to understand the relationship between the two fields. In the pressure data, the characteristic peak is possibly created by a pressure gradient at ocean-floor. This gradient will cause a similar oscillatory flow which will change phases with respect to the pressure. The flow will create an electric field of the characteristic oscillation. Together with this oscillation the electric field sensor is also sensitive to other prevailing oscillations at the ocean-floor, which may further cause change in the phase data of the electric field. For example, in shallow stations tidal induced flow (0.32 Hz) might cause a change in phase data of the electric field. The flow reflection by the topographic can also effect the phase data of electric field.

5.9   Discussion and Result

We studied the mMT data to understand the ambient electromagnetic noise characteristics in the ocean. We have selected six stations from different depths to obtain an understanding of the depth relative noise environment.

The PSD and spectrograms of every shallow stations show a presence of the 0.32 Hz. The absence of the frequency in the deeper stations data indicated that the source is effective only in shallow depths and thus we presumed tidal induced motion as a probable source. The argument is supported by the characteristics like the regional presence, time based spectral power shift and directionality of the feature. The observation of 0.32 Hz is significant as it not only conveys the distortion of mCSEM and mMT data set by the tidal induced motion but it also conveys that the distortion is both time and frequency dependent. In the every deeper stations, we observed a time ambient peak at 0.25 Hz. Unlike 0.32 Hz which was showing a spectral shift in power towards lower frequencies, the 0.25 Hz is observed consistent in time. We implicated non-opposite, non-linear, wave-wave interaction mechanism of Cox *et al.* (1978) to explain the 0.25 Hz. The mechanism suggest that the prevailing pressure gradient at the floor will generate a velocity field, which creates electromagnetic field. Since the 0.25 Hz is as created by a pressure gradient, we expect a similar peak in the pressure spectra. The observation of an identical peak in the pressure spectra strengthens the implication of the mechanism. The peak at 1.2 Hz, which is evident in one of the shallow station and every deeper station, is another significant feature in the spectrograms. We do not observe any time similarity between the stations corresponding to this frequency. It is a temporary peak in every station. These observations indicated for a local influence in the creation of the peak. The spectral pattern of the 1.2 Hz is station dependent. We observed 1.2 Hz presence only in the station with significant topography changes. This observation motivated us to do an experiment to understand a role of slope of the topography. For the purpose, the numerical gradients of the topography is calculated. We found significant slope in every station, where 1.2 Hz is present. Probably, there is a connection of 1.2 Hz with the slope of topography.
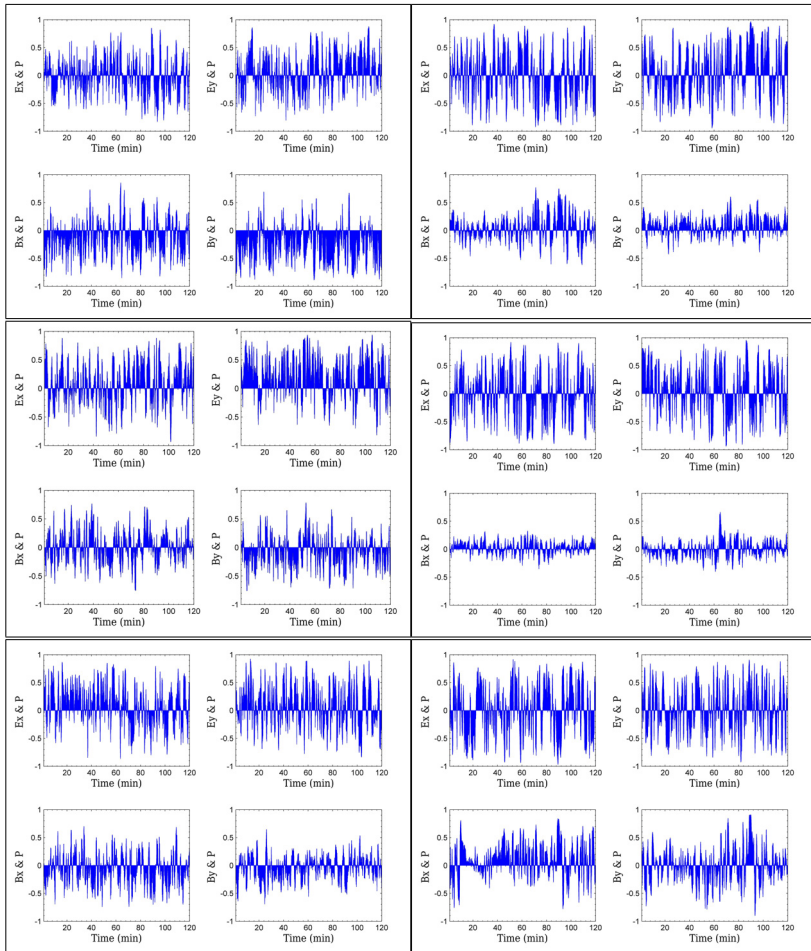
Figure 5.18: The windowed cross-correlation vs. time of six stations. Left three and right three boxes respectively represent the shallow and the deep stations. **Left:** top-Currawong; middle-Bunyip; bottom-Goanna. **Right:** top-Shark; middle-Lorrie; bottom-Corella. Each box contains four cross-correlation plots. Top two plots corresponds electric field and pressure cross-correlation. Bottom two correspond magnetic field and pressure cross-correlation. The index x and y represents x and y component of the respective fields.

A further support to the observation is provided by the haziness which is always evident associated with the 1.2 Hz feature. The haziness is station dependent feature and most likely a role of the topography is thus significant in their creation. The other significant observation which we noted in each shallow station spectrogram is the spectral pattern resemblance of E_y, B_x and B_y component. The observation is also evident in the deeper station data. A good start to the explanation is provided by the spectral patterns, created by haziness in the spectrograms. The studies (Schwalenberg & Edwards 2004) indicated that both the TE and the TM mode will be distortion by the topography. The magnetic fields (say H_y and H_z) are reported to be distorted in the TE mode while electric fields (say E_y and E_z) in the TM mode. The spectral resemblance of B_x and B_y component indicated for a common source, which could be E_z field only. The electric field E_y and E_z, both are TM mode creation by a horizontal movements in the x-direction. The resemblance of E_y, B_x and B_y components are therefore obvious. The distortions are evident more in the horizontal magnetic components than the electric components. Therefore they indicate that the magnetic fields are more sensitive to velocity and topography variations than the electric fields, which is consistent with the theoretical observation. We have modeled each station spectra using an identical velocity and wavelength to simulate both electric and magnetic responses. In general, we have found a good correspondence in the lower frequencies indicating a possible influence by the natural fields. Moreover, the decay of the field also supports the observation by showing a good spectral match in the low frequencies of various depth stations.

We observe a significant distortion in the horizontal magnetic components. The likely reason is the significant sensitivity of the B_x and B_y fields to velocity changes. The cause is supported by the theoretical observations too (Chapter 2), as among all the electromagnetic field components, the B_x, E_z and B_y fields show a sharp change in response pattern at the ocean floor (where the velocity is zero) whereas other fields components show a smooth transition there. The result implicates that the undulating topography in the vicinity of the stations, causing changes (distortions) in the velocity field and consequently might distort these electromagnetic field components, can therefore play a significant role in controlling the quality of the electromagnetic (i.e. mCSEM/mMT signals) recordings.

We observed the correlation between the electric/magnetic and pressure field. For the correlation, we first used a long time-series and then observed a small correlation magnitude. Despite the similarity in spectral content between fields, small magnitude was surprising. We soon realized that to satisfy the spectral content, one minutes time window would be sufficient. We used windowed cross-correlation technique to study the extent of similarity between the two wave-forms using one minutes of time window. This time we observed a good correlation magnitude between electric field and pressure. In general, from deeper and shallower station, we observed a correlation magnitude greater than 1/2. Noteworthy point is the correlation magnitude, which is higher in deeper stations than the shallower one. Possibly, the stronger vertical velocity component is an influencing factor. We do not expect complete spectral range similarity in the waveforms of the electric and pressure field, the observations indicate that there is a role of frequency dependent com-

mon force mechanism in the creation of the electric and the pressure field. The horizontal magnetic field components in the deeper show a poor correlation magnitude, probably due to weak vertical velocity component in their creation.

6   Conclusions

The developed theory profoundly explains the physics of the electromagnetic field creation in the ocean by the oceanic movements. We have shown that the horizontal oceanic flow in a vertical geomagnetic field will create only the TM mode, which is a galvanic mode. In this mode, the accumulation of the surface charges and the induction process might respectively energize the vertical and horizontal components of the current density. The TE mode is a purely inductive mode and its creation demands both vertical and horizontal component of the velocity field.

The theory of TM mode show that the B_x and E_z fields show a significant change in the response pattern (below the floor) for a spatial change in the velocity field in the vertical direction. The observation is suggestive of extra-responsiveness of both the field components for a velocity changes. A similar response for the corresponding velocity change is shown by the B_y field component in the TE mode. Theoretical results therefore suggest that the horizontal magnetic fields are extra sensitive to velocity changes. Practically, the mMT data shows a significant distortion in the horizontal magnetic fields (i.e. B_x and B_y fields). The integral interpretation of the theoretical results and the observed distortions suggest that the distortions might be caused by a change (distortion) in the velocity field generated by the local undulating topography in the vicinity in the receivers. This is a good example where the developed theory complements the practical observation. A further significant observation obtained from the mMT data is the spectral correspondence of the lower band with the modeled spectra from different depth. The natural field is controlling the lower spectral range (in the modeling). The considerable agreement between the modeled and observed results from different depths therefore support the decay of the natural field (like MT field). The natural field is therefore one of the probable prime source to govern the field strength in the lower spectral range.

We have observed some correlation between the electric/magnetic and pressure field which are systematically positive or negative and therefore indicating a complicated type similarity in the wave-form. Data with small time-length provides a significant correlation magnitude while this is not true for larger time-length. Moreover, the magnitude of correlation is significant in greater depth stations. The electric field (at 0.25 Hz) created by the pressure-gradients (generating significant vertical component of the velocity field) is observed significant in the greater depth stations compared to the shallow stations. The combined interpretation of above two results indicates an influence of the vertical velocity component in deciding the correlation magnitude. The weak correlation magnitude

between the pressure and horizontal magnetic field of the deeper stations further supports the argument as vertical velocity field will generate only the significant horizontal electric field, whose spatial derivative will create the B_x and B_y fields. We have found pressure measurements significant to characterise an electromagnetic spectral peak (of 0.25 Hz) created by the pressure field. Other than this, we do not see any other significant information by the pressure measurements. The overall observations indicate that pressure measurements might not be useful to correct the noise.

We have demonstrated in chapter 3 and 5 that the oceanic features (created by different movements) contributing significant electromagnetic fields to the mCSEM data are, mainly, 1. the velocity field formed by the pressure gradient near the ocean floor created by the non-opposite, non-linear interactions of the waves at the surface; 2. the perturbed velocity field generated by the floor topography; 3. the tidally induced motion and 4. microseisms. Among these features, a microseism is powerful to considerably distort the mCSEM signal (Section 3.10). The time when transmitter was active, the strong recording of a microseism indicates the distortion of the mCSEM signal and suggests a necessity to account them for any realistic mCSEM modeling. Regardless of the fact that the strength of the fields by a microseism depends on the parameters of its creation, the observed results suggest that they might be significant even at small transmitter-receiver (T-R) separations. A possible simulation of microseisms (Webb & Cox 1986), provided the velocity data at the receiver station is available, may help to improve the target detection possibility. The only time ambient feature we observed is the 1st one (i.e non-opposite, non-linear interaction at surface). The strength of the feature suggest its significance only in stations with large T-R separations. The feature is as generated by a time ambient source and therefore may distort every station at significantly large T-R separations. In the shallow ocean, the strength of the feature is weaker than the strength created by the tidally induced motion. The strength of various features are controlled primarily by the velocity field and therefore a vector velocity measurement near the stations may help to rectify the distortion by any motional induced field. Moreover, the modeling of the surface waves (as discussed in the Section 3.8) suggests that these waves can hardly penetrate to some tens of meter. This observation in addition supports the measurement of the velocity field near the floor, as local velocity field play a prime role in the creation of the field, to quantify the distortion of the mCSEM signals.

Finally, the observed influences by the oceanic sources in mCSEM/mMT data require a treatment before modeling for the reservoirs. The velocity components measurement at the receiver station is recommended for effective noise reduction. This is significant because we have shown that different velocity components excite different electromagnetic modes.

References

Bahr, Karsten. 1988. On the feasibility of seafloor magnetotelluric soundings in the North Sea. *Ocean Dynamics*, **41**, 277–281. 10.1007/BF02225936.

Beal, HT, & Weaver, JT. 1970. Calculations of magnetic variations induced by internal ocean waves. *Journal of Geophysical Research*, **75**(33), 6846–6852.

Bendat, J S, & Piersol, A G. 1986. *Random Data: Analysis & Measurement Procedures*. John Wiley and Sons, Inc.

Bromirski, Peter D. 2005. Mid-ocean microseisms. *Geochemistry Geophysics Geosystems*, **6**(4), 1–19.

Camara, Alfaro J, Corcoran, C, Davies, K, Gonzalez, Pineda F, Hampson, G, Hill, D, Howard, M, Kapoor, J, Moldoveanu, N, & Kragh, E. 2007. Reducing Exploration Risk. *Oilfield Review 19*, **Spring**(1), 26–43.

Carter, R W G. 1988. *Coastal Environments.* Academic Press.

Chave, A D, Constable, S C, & Edwards, R N. 1991. *Electrical exploration methods for the seafloor*. Vol. 2. Society Of Exploration Geophysicists. Pages 931–966.

Chave, Alan D. 1983. On the Theory of Electromagnetic Induction in the Earth by Ocean Currents. *Journal of Geophysical Research*, **88**(B4), 3531–3542.

Chave, Alan D., & Cox, Charles S. 1982. Controlled Electromagnetic Sources for Measuring Electrical Conductivity Beneath the Oceans 1. Forward Problem and Model Study. *Journal of Geophysical Research*, **87**(B7), 5327–5338.

Chave, Alan D., & Filloux, J. H. 1984. Electromagnetic induction fields in the deep ocean off California: oceanic and ionospheric sources. *Geophysical Journal International*, **77**(1), 143–171.

Chave, Alan D, & Luther, Douglas S. 1990. Low-Frequency, Motionally Induced Electromagnetic Fields in the Ocean 1. Theory. *Journal of Geophysical Research*, **95**(C5), 7185–7200.

Christensen, Niels B., & Dodds, Kevin. 2007. 1D inversion and resolution analysis of marine CSEM data. *Geophysics*, **72**(2), WA27.

Constable, S. C. 1990. Marine electromagnetic induction studies. *Surv.Geophys.*, **11**, 303–327.

Constable, S. C., Orange, A. S., Hoversten, G. M., & Morrison, H. F. 1998. Marine magnetotellurics for petroleum exploration Part I: A sea-floor equipment system. *Geophysics*, **63**(3 may-june), 816–825.

Constable, Steven, & Srnka, Leonard J. 2007. An introduction to marine controlled-source electromagnetic methods for hydrocarbon exploration. *Geophysics*, **72**(2), WA3–WA12.

Constable, Steven, Key, Kerry, & Lewis, Lisl. 2009. Mapping offshore sedimentary structure using electromagnetic methods and terrain effects in marine magnetotelluric data. *Geophysical Journal International*, **176**(2), 431–442.

Constable, Steven C, & Key, Kerry. 2006. Marine Electromagnetic Methods for Hydrocarbon Exploration. *SEG*, 136–224.

Cox, C. 1980. Electromagnetic induction in the oceans and inferences on the constitution of the earth. *Surveys in Geophysics*, **4**(1), 137–156.

Cox, C S. 1981. On the electrical conductivity of the oceanic lithosphere. *Physics of the Earth and Planetary Interiors*, **25**(3), 196–201.

Cox, Charles, Kroll, Norman, Pistek, Pavel, & Watsons, K. 1978. Electromagnetic fluctuations induced by wind waves on the deep-sea floor. *Journal of Geophysical Research*, **83**(C1), 431–442.

Crews, A., & Futterman, J. 1962. Geomagnetic Micropulsations Due to the Motion of Ocean Waves. *J. Geophys. Res.*, **67**(1), 299–306.

De Lauro, E, De Martino, S, Falanga, M, & Palo, M. 2006. Statistical analysis of Stromboli VLP tremor in the band [0.1-0.5] Hz: some consequences for vibrating structures. *Nonlinear Processes in Geophysics*, **13**, 393–400.

Edwards, Nigel. 2005. Marine Controlled Source Electromagnetics: Principles, Methodologies, Future Commercial Applications. *Surveys in Geophysics*, **26**(6), 675–700.

Eidesmo, T, Ellingsrud, S, MacGregor, L M, Constable, S, Sinha, M C, Johansen, S, Kong, F N, & Westerdahl, H. 2010. Sea Bed Logging (SBL), a new method for remote and direct identification of hydrocarbon filled layers in deepwater areas. *First Break*, **20**(March), 144–152.

Ellingsrud, S, Eidesmo, T, Johansen, S, Sinha, M C, MacGregor, L M, & Constable, S. 2002. Remote sensing of hydrocarbon layers by seabed logging (SBL): results from a cruise offshore Angola. *The Leading Edge*, **21**(10), 972.

Ezer, Tal, Heyman, William, Houser, Chris, & Kjerfve, B. 2010. Modeling and observations of high-frequency flow variability and internal waves at a Caribbean reef spawning aggregation site. *Ocean Dynamics*, 1–18.

Faraday, Michael. 1832. The Bakerian Lecture. Experimental Researches in Electricity. Second Series. *Philosophical Transactions of the Royal Society of London*, **122**, 163–194.

Feynman, R P, Leighton, R B, & Sands, M. 1963. *The Feynman Lectures on Physics, Volume II*. Addison-Wesley.

Fraser, D. C. 1966. The Magnetic Fields of Ocean Waves. *Geophysical Journal International*, **11**(5), 507–517.

Griffin, D. 1984. Signal estimation from modified short-time Fourier transform. *IEEE Transactions on Acoustics Speech and Signal Processing*, **32**(2), 236–243.

Haubrich, R. A., Munk, W. H., & Snodgrass, F. E. 1963. Comparative spectra of microseisms and swell. *Bulletin of the Seismological Society of America*, **53**(1), 27–37.

Hesthammer, Jonny, & Boulaenko, Mikhail. 2005. The offshore EM challenge. *First Break*, **23**(November), 59–66.

Jackson, J D. 1975. *Classical Electrodynamics*. Vol. 67. Wiley.

Kedar, Sharon, Longuet-Higgins, Michael, Webb, Frank, Graham, Nicholas, Clayton, Robert, & Jones, Cathleen. 2008. The origin of deep ocean microseisms in the North Atlantic Ocean. *Proceedings of the Royal Society A Mathematical Physical and Engineering Sciences*, **464**(2091), 777–793.

Kinsman, Blair. 2002. *Wind Waves: Their Generation and Propagation on the Ocean Surface*. Dover Pubns.

Koefoed, O., Patra, H.P., & Mallick, K. 1980. *Geosounding principles*. Methods in geochemistry and geophysics. Elsevier Scientific Pub. Co.

Lamb, H. 1932. *Hydrodynamics*. (6th ed.). Cambridge U. Press.

Larsen, J. 1973. An introduction to electromagnetic induction in the ocean. *Physics of The Earth and Planetary Interiors*, **7**(3), 389–398.

Larsen, J C. 1997. Noise Reduction in Electromagnetic Time Series to Improve Detection of Seismic-Induced signals. *Journal of Geomagnetism and Geoelectricity*, **49**, 1257–1265.

LeBlond, Paul H, & Mysak, Lawrence A. 1978. *Waves in the ocean*. Elsevier Scientific Pub. Co., New York :.

131

Leont'yev, I. 2009. Generation mechanism of an alongshore bar on a sandy beach slope. *Oceanology*, **49**(2), 281–289.

Longuet-Higgins, M S, Stern, Melvin E, & Stommel, Henry M. 1954. *The electrical field induced by ocean currents and waves, with applications to the method of towed electrodes*. Vol. 13. Massachusetts Institute of Technology and Woods Hole Oceanographic Institution.

Longuet-Higgins, MS. 1950. A theory of the origin of microseisms. *Philosophical Transactions of the Royal Society of London Series A Mathematical and Physical Sciences*, **243**(857), 1–35.

Longuet-Higgins, M.S., & Ursell, F. 1948. Sea waves and microseisms. *Nature*, **162**(4122), 700–700.

MacGregor, L, & Sinha, M. 2000. Use of marine controlled-source electromagnetic sounding for sub-basalt exploration. *Geophysical Prospecting*, **48**(6), 1091–1106.

MacGregor, L M, & Tompkins, Michael J. 2005. Imaging Hydrocarbon Reservoirs Using Marine Controlled-Source Electromagnetic Sounding. *Offshore Technology Conference*, 1–3.

Manoj, C, Kuvshinov, A, Neetu, S, & Harinarayana, T. 2010. Can undersea voltage measurements detect tsunamis? *Earth, Planets and Space*, **62**(3), 353–358.

Mei, Chiang C. 1989. *The Applied Dynamics of Ocean Surface Waves*. Singapore: World Scientific.

Nabighian, Misac N. 1987. *Electromagnetic Methods in Applied Geophysics, Volume 1, Theory*. SEG.

Nichols, C R, & Williams, R G. 2008. *Encyclopedia of Marine Science*. Science Encyclopedia. Facts on File.

Palshin, N.A. 1996. Oceanic electromagnetic studies: a review. *Surveys in geophysics*, **17**(4), 455–491.

Peterson, J. 1993. *Observations and Modeling of Seismic Background Noise*.

Phillips, O M. 1977. *The Dynamics of the Upper Ocean (Ed. by Batchelor, G K and Miles, J W)*. Cambridge University Press.

Pinet, Paul R. 2006. *Invitation to Oceanography*. Jones & Bartlett Publishers.

Podney, Walter. 1975. Electromagnetic Fields Generated by Ocean Waves. *Journal of Geophysical Research*, **80**(21), 2977.

Ponomaryov, E. 1998. Microseisms and infrasound: a kind of remote sensing. *Physics of The Earth and Planetary Interiors*, **108**(4), 339–346.

Reddy, M P M. 2001. *Descriptive physical oceanography*. A.A. Balkema.

Sanford, Thomas B. 1971. Motionally Induced Electric and Magnetic Fields in the Sea. *Journal of Geophysical Research*, **76**(15), 3476–3492.

Schwalenberg, K, & Edwards, R N. 2004. The effect of seafloor topography on magnetotelluric fields: an analytical formulation confirmed with numerical results. *Geophysical Journal International*, **159**(2), 607–621.

Shin, K, & Hammond, Joseph. 2008. *Fundamentals of Signal Processing for Sound and Vibration Engineers*. Wiley Interscience.

Sinha, Martin C, Patel, P D, Unsworth, Martyn J, Owen, T R E, & MacCormack, M G R. 1990. An active source electromagnetic sounding system for marine use. *Marine Geophysical Research*, **12**, 29–68.

Stewart, Robert H. 2007. *Introduction to Oceanography*. Department of Oceanography, Texas A & M University.

Sundermann, J. 1994. *Coastal, estuarial, and harbour engineers' reference book Edited by Abbott, M. B. and Price, W. A.* E & FN Spon.

Tanimoto, T. 2005. The oceanic excitation hypothesis for the continuous oscillations of the Earth. *Geophysical Journal International*, **160**(1), 276–288.

Tanimoto, T., Ishimaru, S., & Alvizuri, C. 2006. Seasonality in particle motion of microseisms. *Geophysical Journal International*, **166**(1), 253–266.

Toh, H., Satake, K., Hamano, Y., Fujii, Y., & Goto, T. 2011. Tsunami signals from the 2006 and 2007 Kuril earthquakes detected at a seafloor geomagnetic observatory. *Journal of Geophysical Research*, **116**(B2), 1–10.

Vozoff, K. 1991. *Electromagnetic Methods in Applied Geophysics, Volume 2, Ed. by Nabighian, Misac N*. SEG.

Ward, S.H., & Hohmann, G.W. 1987. *Electromagnetic Methods in Applied Geophysics (Ed. by Nabighian, Misac N), Volume 1, Theory*. SEG.

Webb, SC, & Cox, CS. 1972. The magnetotelluric method in the exploration of sedimentary basins. *Geophysics*, **91**, 98Ű–141.

Webb, SC, & Cox, CS. 1984. Pressure and electric fluctuations on the deep sea floor: Background noise for seismic detection. *Geophysical Research Letters*, **11**(10), 967–970.

Webb, SC, & Cox, CS. 1986. Observations and Modeling of Seafloor Microseisms. *Journal of Geophysical Research*, **91**(B7), 7343–7358.

Webb, Spahr C, Zhang, Xin, & Crawford, Wayne. 1991. Infragravity Waves in the Deep Ocean. *Journal of Geophysical Research*, **96**(C2), 2723–2736.

Weidelt, Peter. 2007. Guided waves in marine CSEM. *Geophysical Journal International*, **171**(1), 153–176.

Weitemeyer, K A, Constable, S C, Key, K W, & Behrens, J P. 2006. First results from a marine controlled-source electromagnetic survey to detect gas hydrates offshore Oregon. *Geophysical Research Letters*, **33**(3), 1–4.

Welch, P D. 1967. The Use of Fast Fourier Transform for the Estimation of Power Spectra: A Method Based on Time Averaging Over Short, Modified Periodograms. *IEEE Transactions on Audio and Electroacoustics*, **15**(2), 70–73.

Young, F. B., Gerrard, H., & Jevons, W. 1920. XIII. On electrical disturbances due to tides and waves. *Philosophical Magazine Series 6*, **40**(235), 149–159.

Appendix A:

The calculation of the transfer function $b_e(z)$ and $b_m(z)$ for a downward diffusing electromagnetic field

$$\sigma_0 = 0, \mu_0$$

$$z = h_1 = 0$$

$$d_1 \qquad \sigma_1, \ \mu_1$$

$$z = h_2$$

$$z = h_n$$

$$d_n \qquad \sigma_n, \ \mu_n$$

$$z = h_{n+1}$$

$$z = h_N$$

$$\sigma_N, \ \mu_N$$
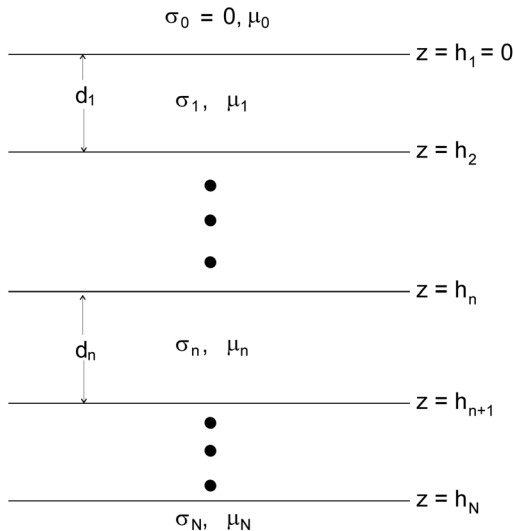
Figure 1: Diagram showing the sketch plan of the N-layered earth
.

For a layered earth construction, the transfer function $b_e(z)$ in the TE mode can easily be obtained by the recursion (e.g. Ward & Hohmann (1987)). Let us consider N layered earth with conductivities σ_n and thickness d_n (Fig. 1). We assume that the source is present at interface s.

Let $\alpha_n = \sqrt{S^2 + i\omega\mu_n\sigma_n}$, $\qquad \eta_n = \alpha_n/\mu_n$ $\quad$ and $\quad$ $b_n = b_e(h_n)$

Then b_n is recursively obtained from

$$b_N = \eta_n, \qquad b_n = \eta_n \frac{b_{n+1} + \eta_n \tanh(\alpha_n d_n)}{\eta_n + b_{n+1} \tanh(\alpha_n d_n)} \quad \text{for } n = N-1, ..., s \tag{1}$$

Similarly, the TM mode transfer function $b_m(z)$ can also be obtained using the the recursion. For N layered earth with conductivities σ_n and thickness d_n (Fig. 1) and with a source presence at interface s

Let $\xi_n = \alpha_n/\sigma_n$ $\quad$ and $\quad$ $b_n = b_m(h_n)$

Then b_n is recursively obtained from

$$b_N = \xi_n, \qquad b_n = \xi_n \frac{b_{n+1} + \xi_n \tanh(\alpha_n d_n)}{\xi_n + b_{n+1} \tanh(\alpha_n d_n)} \quad \text{for } n = N-1, ..., s \tag{2}$$

Appendix B:

A GUI Program: MENA

In order to address the problems of the quantitative study of the electromagnetic noise by the oceanic and the natural sources, we have developed a software code MENA (i.e. **M**arine **E**lectromagnetic **N**oise **A**nalyser). It is a graphical user interface program, written in the Matlab environment. The main features of the program are as follows:

1. MENA helps in study of:

   (a) Ionospheric and magnetospheric current system induced electromagnetic fields.

   (b) Motionally contributed electromagnetic field.

   (c) Combination of above two fields.

2. Layered model: MENA utilises the layered Green's function to replicate the layered earth.

3. Surface wave simulation: The TE mode selection is applicable for the simulation of the surface gravity waves.

4. Layered velocity model: The TM mode selection allows you to use a layered velocity model.

5. Outputs: MENA generates the outputs in figure governing:

   (a) Fields variation with respect to the depth.

   (b) The power spectral density (PSD) at any desired depth.

   (c) Random phase time series at a user defined depth.

6. For the calculation of naturally induced fields, rather than constant magnetic field variation, a magnetic field spectrum is utilised.

7. Noise addition: An option allows the addition of noise in the time-series. Three types of noise can be added to the time-series:

    (a) Signal to noise (S/N) ratio based white noise.

    (b) Fixed amplitude white noise.

    (c) Frequency based addition of the noise.

8. Noisy Power Spectrum: MENA allows an easy comparison of noisy time series and corresponding change in power spectral density.

Start Manual for the users of the MENA

How to start "MENA"?

Please follow the steps to get the welcome screen of MENA

1. Go to the folder MENA\welcome

2. Open the Matlab file "welcome.m".

3. Press the key **F5** from the keyboard (or in Matlab window, go to **debug** and choose **run**).

4. Now, a welcome screen of 'MENA' as shown in the Fig. 2 will pop up.
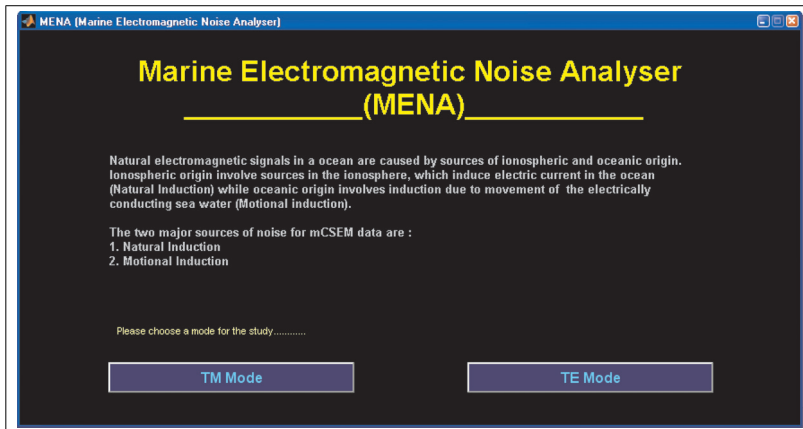
Figure 2: Welcome screen of the MENA. It demands an input based on your choice of the modal study. For a TM mode study press TM or vice-versa.

5. For a study, choose a selection among 'TE mode' or 'TM Mode'.

    (a) if choice is TM mode, press 'TM Mode'. This will show to an input window shown in Fig. 3.
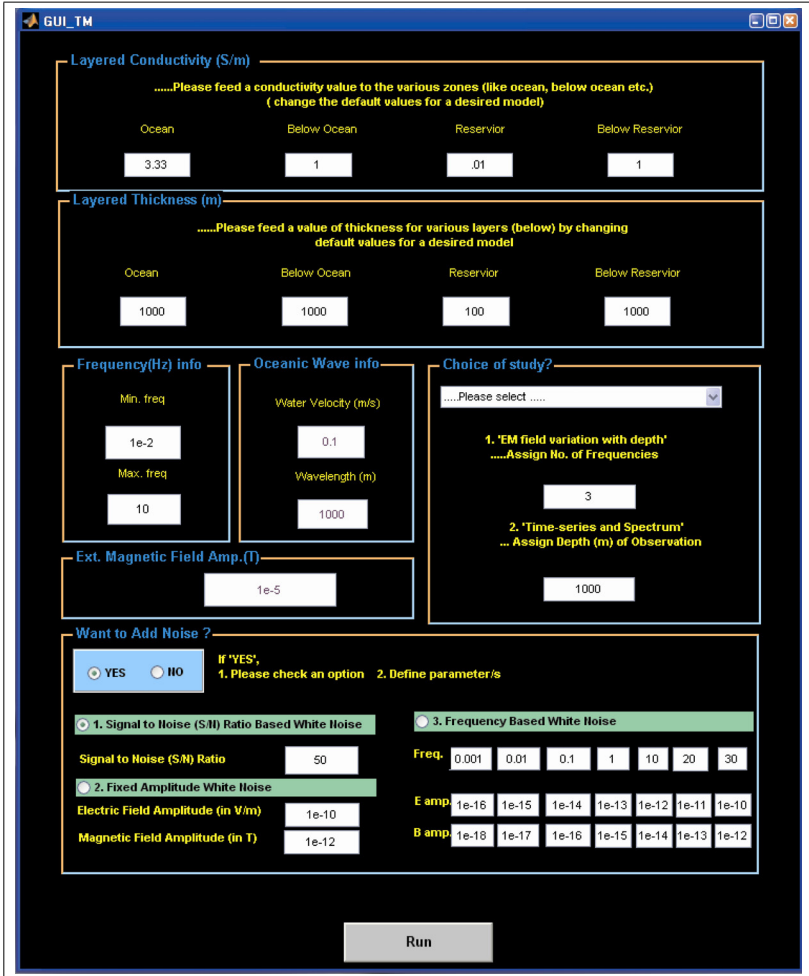
Figure 3: The TM mode screen window of the MENA. Window demands selection of *Choice of study?*, after defining a model and their parameter values.

(b) Prepare a desired four layer model by assigning conductivity (in S/m) & thickness (in meter) values. Please choose a frequency-band of interest by typing on a value in the edit-box of the Min. freq. & Max. freq. (in Hz). Enter a value of the water wave velocity (in m/s) & wavelength (in meter) edit-box. The Ext. Magnetic Field Amp. (in Tesla) reads the value of an ambient Geomagnetic field prevailing in the experimental region. Please select a choice from the pop-up menu (the section-*Choice of study?*) among:

- EM field variation with depth,
- The power spectral density (PSD) at any desired depth,
- Random phase time series at a user defined depth.

For example: If the choice is **EM field variation with depth**, please assign a number to edit-box representing the number of frequencies. Now, press **Run**. Following outputs (Fig. 4 and Fig. 5) will appear for the default values:
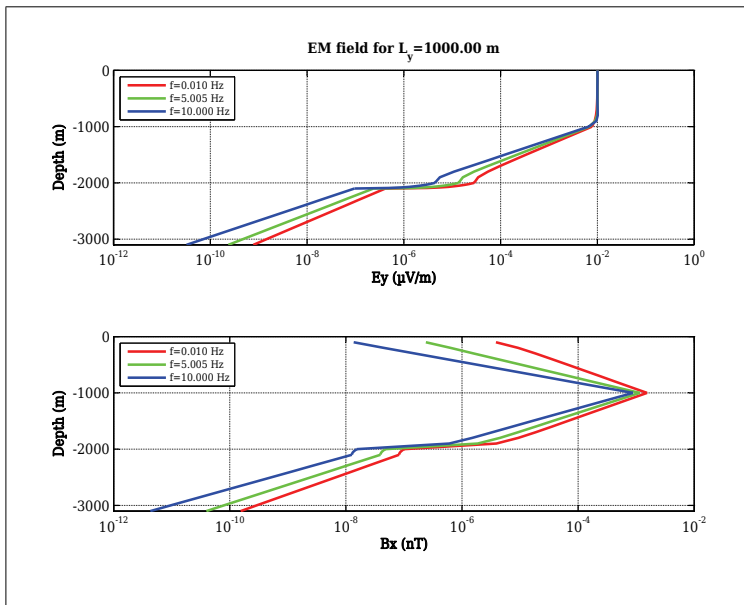
Figure 4: For a 1 km wave, the variation of *motionally induced* horizontal electromagnetic fields (E_y and B_x) with respect to the depths is shown. Red, blue and green line corresponds to the frequency 0.01, 5.005 & 10 Hz, respectively.

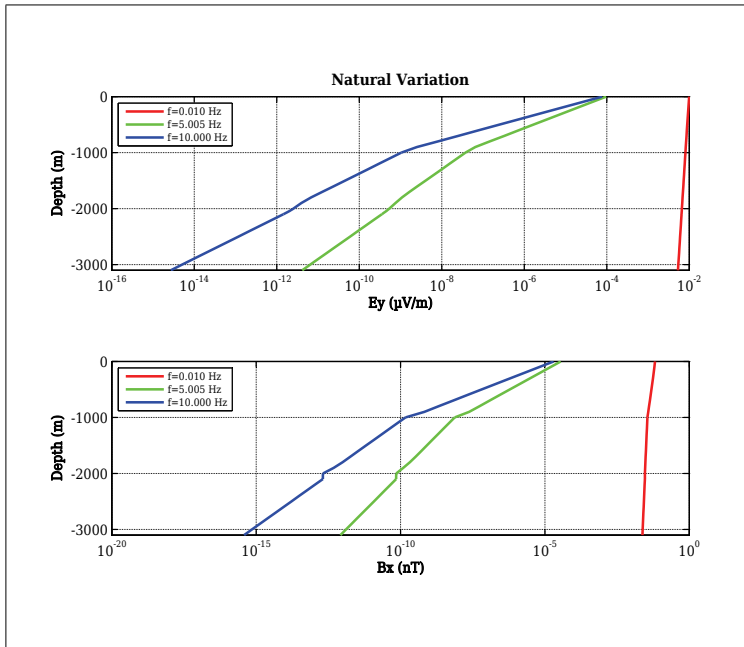Similarly, we can obtain output for two other choices by selecting one from the pop-up menu.

Figure 5: The ionospheric current system generated *naturally induced* horizontal electromagnetic fields (E_y and B_x) variation with respect to the depths is shown. The red, blue and green line corresponds to the frequency 0.01, 5.005 & 10 Hz, respectively.

(c) After the TM mode analysis, if you wish to do TE mode analysis, please close every window and repeat the steps 1 to 4. Now for the TE mode, press **TE Mode**. A new window will appear (Fig. 6)

(d) Prepare a desired four layer model by assigning conductivity (in S/m) & thickness (in meter) values. The Ext. Magnetic Field Amp. (in Tesla) reads the value of a ambient geo-magnetic field prevailing in the experimental region. For the simulation of surface waves, enter a value of the wave height (in meter) in edit-box. Please define a wavelength range of interest by typing on a value in the edit-box of the Min. wavelength & Max. wavelength (in meter). Please select a choice from the pop-up menu, as did for TM mode case.
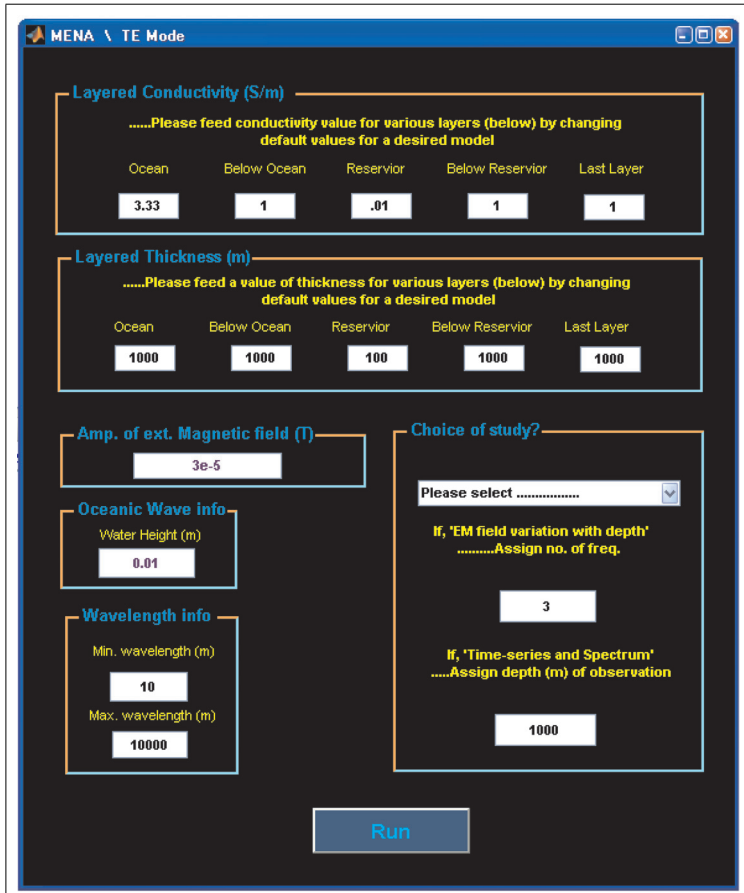
Figure 6: The TE mode screen window of the MENA. Window demands selection of *Choice of study?*, after defining a model and their parameter values.

Acknowledgments

I owe my deepest gratitude to Prof. Andreas Hördt, who has not only given careful guidance as my supervisor, but has provided considerable support during the study. The valuable comments and suggestions have added enormous value to the quality of the study. There is no doubt that without his constant prodding and helpful chidings, this study would not have been got this shape.

The comprehensive care by Late Prof. Peter Weidelt, his guidance, encouragement and teaching is among one of my wonderful lifetime memories. I feel lucky to work with and to know him but same-time unlucky to miss him to an extent as I never ever missed any one.

Thanks to KMS Technologies-KJT Enterprises Inc. for the sponsorship and fruitful discussions. I am grateful to Prof. Dr. Kurt Strack and Mr. Tilman Hanstein for his support and help.

Prof. Steven Constable provided the mMT data set. I am thankful for his kindness, support and helpful discussions.

A foreigner can easily mix with the cross-language and culture with the friends like Mr. Erik Peneewitz, Mr. Marcus Fundling, Miss. Stefanie Milde and Miss Sabine Mathesius. I am thankful for their consistent support. They not only shared good memories but also added their help to make my Braunschweig stay comfortable.

I wish to show my gratitude to the persons like Mrs. Heidi Weidelt, who made me to first feel Germany as my second home, has touched my heart by the warm celebration on a happy occasion of my daughters birth, in days when I was missing my family. Mrs. Monica Cremer Hördt has given a consistent support by visiting my family every week since more than two years. It is result of her pure and warm love which has made her favorite of my daughter and wife. The social work of Mrs. Steffi Bouomann connected us, which resulted in a family friendship. The respectful work and her simplicity always inspire. A wonderful lady with great social values Mrs. Inge Els-Velivassis keeps a special space in our memories. Her time to time visits, celebrations, 24 hrs stay at her home with delicious foods and many delights, consistent invitation to visit Wolfenbüttel are among rare memories.

I am indebted to Mr. Vamshi Togiti, Mr. Jayata Mishra, Dr. Puspendra Kumar and Mrs. Shireesha Sajjanapu for their valuable friendship and consistent family support.

I am grateful to Dr. S K Verma and Dr. Ajay Manglik of NGRI, Hyderabad for their encouragement and supports. I also thank Dr. Vikas Baranwal of NGU, Norway for

Curriculum Vitae

Surname:	Bhatt
First Name:	Kaushalendra
Middle Name:	Mangal
Date of Birth:	25 April 1981
Nationality:	Indian
Marital status:	Married
Email:	kmbhatt@rediffmail.com

Positions: **May 2008–Continuing**

Doctoral Student, Technical University, Braunschweig, Lower Saxony, Germany

Aug. 2006–April 2008

Geophysicist, Institute of Seismological Research, Gandhinagar, Gujarat, India

Dec. 2005–Aug. 2006

JRF, National Geophysical Research Institute, Secundarabad, Andhra-Pradesh, India

Nov. 2003–Nov 2005

CSIR Diamond Jubilee Awardee, National Geophysical Research Institute, Secundarabad, Andhra-Pradesh, India

PREVIOUS RESEARCH EXPOSURES

1. Numerical Electromagnetic Modeling of frequency domain electromagnetic sounding data.

2. Development of a Joint Inversion code.

3. Resistivity Imaging (HERT Imaging).

4. Seismological studies related to Kachchh, Gujarat, India.

5. Real Time Earthquake Epicenter location (through V-SAT connected broadband data).

6. The b-value and Seismicity analysis.

Education: **1997-2000**

M.Sc. (Tech), Geophysics from Banaras Hindu University, Department of Geophysics, Varanasi, U.P., India; First Division

2000-2003

B.Sc. (Phy. Che. and Math), Purvanchal University, Jaunpur, Varanasi, U.P., India; First Division

SCHOLARSHIPS AND AWARDS

1. Education Award for Seven Years (1990-1997) from "Ministry of Human Resource Development", Department Of Education; Government of India in Year 1990.

2. UGC Scholarship (2002).

3. CSIR Diamond Jubilee Award (2003).

Publications

PUBLICATIONS

1. Bhatt, K. M., Hördt, A., Weidelt, P. and Hanstein, T. (2009) Motionally Induced Electromagnetic Field within the Ocean, 23rd Schmucker-Weidelt Kolloquium für Elektromagnetische Tiefenforschung, Page 46-59, ISSN 0946-7467.

2. Bhatt, K. M., Hördt, A. and Hanstein, T. (2009) Analysis of seafloor marine EM data with respect to motion induced noise, 23rd Schmucker-Weidelt Kolloquium für Elektromagnetische Tiefenforschung, Page 33-45, ISSN 0946-7467.

CONFERENCE PAPERS

1. Bhatt, K. M., Hördt, A., Weidelt, P. and Hanstein, T. (2009) Motion induced noise in marine controlled source electromagnetic data, 69th DGG in Keil, page 178-179 (Oral).

2. Bhatt, K. M., Hördt, A., Weidelt, P. and Hanstein, T. (2009) Motionally Induced Electromagnetic Field within the Ocean, 23rd Schmucker-Weidelt Kolloquium für Elektromagnetische Tiefenforschung, Heimvolkshochschule am Seddiner See, 28 Sept - 2 Oct 2009 (Oral).

3. Bhatt, K. M., Hördt, A. and Hanstein, T. (2009) Analysis of seafloor marine EM data with respect to motion induced noise, 23rd Schmucker-Weidelt Kolloquium für Elektromagnetische Tiefenforschung, Heimvolkshochschule am Seddiner See, 28 Sept - 2 Oct 2009 (Poster).

4. Bhatt, K. M., Hördt, A., Weidelt, P. and Hanstein, T. (2010) Motion Induced Noise in Marine Electromagnetism, 20th international electromagnetic induction workshop, Giza, Egypt (Poster).

5. Bhatt, K. M., Hördt, A., Hanstein, T. and Baranwal, V. C. (2010) Spectral-Directionalogram: Representing the directions of the registered frequencies in time, 20th international electromagnetic induction workshop, Giza, Egypt (Oral).

6. Bhatt, K. M., Hördt, A. and Hanstein, T. (2009) Electromagnetic Noise in marine Controlled Source Electromagnetic Data, 71st DGG in Cologne, page 39 (Poster).

OTHER PUBLICATIONS

1. Bhatt, K. M., Hördt, A. and Kumar, S. (2009) Seismicity analysis of the Kachchh aftershock zone and tectonic implication for 26 Jan 2001 Bhuj earthquake, Tectonophysics, 465, 75-83.

2. Bhatt, K. M. and Kumar, S. (2009) Anomalous b-value in seismogenic layer of Bhuj Region, Journal of Ind. Geo. Union, July 2009, Vol.13, No.3, pp.99-106.

3. Bhatt, K. M. (2006) Kachchh: Physics and Fault Pattern, Proceedings of 13th Symposium on Earthquake Engineering, Dec 18-20, 2006, I.I.T. Roorkee, Page 27-33.

ABSTRACTS

1. Verma, S. K. and Bhatt, K. M. (2004) 3-D electromagnetic modeling of a kimberlite pipe to assess conductivity variations with depth, 17th International Electromagnetic Workshop, Hyderabad, India.

2. Verma, S. K., Dutta, S. and Bhatt, K. M. (2004) Remodeling of old profiling data to study the resistivity-depth images of kimberlite pipe, 17th International Electromagnetic Workshop.

3. Verma, S. K. and Bhatt, K. M. (2004) Influence of xenolith in 3D electromagnetic modeling of a kimberlite pipe, 41st annual convention and meeting of Indian Geophysical Union, Dec. 29-31, 2004, NGRI, Hyderabad, India.

4. Verma, S. K., Murty, N. S. K., Rao, V. A., Chandra, S., Dutta, S., Bhatt, K. M. and Ahmad S. (2004) Delineation of overburden, floats, pulses, and crustal xenolith with in a kimberlite pipe by HERT imaging, 41st annual convention and meeting of Indian Geophysical Union, Dec. 29-31, 2004, NGRI, Hyderabad, India.

5. Verma, S. K. and Bhatt, K. M. (2004) Electromagnetic modeling of a kimberlite pipe with epiclastic sediments, 42st annual convention and meeting of Indian Geophysical Union, Barkatullah University, Bhopal, India.

6. Verma, S. K., Murty, N. S. K., Manglik, A., Dutta, S., Bhatt, K. M. and Ahmad S. (2004) Three dimensional structure of a kimberlite pipe by HERT technique, 41st annual convention and meeting of Indian Geophysical Union, Barkatullah University, Bhopal, India.

7. Bhatt, K. M., Rao, V. A., Sharma, V. S. and Verma, S. K. (2006) Resistivity Tomography and SP Surveys to study faulted deep seated Coal seams; National Seminar on New Frontiers in Environmental and Engineering Geophysics, May 30-31, Andhra University, Visakhapatnam, India.

8. Bhatt, K. M. (2007) Fault pattern and Bhuj earthquake, 44th Annual Convention of Indian Geophysical Union, Nov.21-23, Kurukshetra, India.

9. Bhatt, K. M. and Kumar, S. (2007) Anomalous b-value in seismogenic layer of Bhuj region, 44th Annual Convention of Indian Geophysical Union, Nov.21-23, Kurukshetra, India.

10. Bhatt, K. M. (2007) Rotation of faulted block in 26 Jan 2001, Bhuj earthquake, 44th Annual Convention of Indian Geophysical Union, Nov.21-23, Kurukshetra, India.